論文 / 著書情報
Article / Book Information

題目(和文)	HR-AESとToF-SIMSの先進的利用による実用表面･界面分析の展望
Title(English)	Perspective on practical surface and interface analysis by advanced use of HR-AES and ToF-SIMS
著者(和文)	阿部芳巳
Author(English)	
出典(和文)	学位:博士(理学), 学位授与機関:東京工業大学, 報告番号:甲第5877号, 授与年月日:2004年9月30日, 学位の種別:課程博士, 審査員:
Citation(English)	Degree:Doctor (Science), Conferring organization: Tokyo Institute of Technology, Report number:甲第5877号, Conferred date:2004/9/30, Degree Type:Course doctor, Examiner:
学位種別(和文)	博士論文
Type(English)	Doctoral Thesis

A Doctoral Thesis

Perspective on
Practical Surface and Interface Analysis
by Advanced Use of
HR-AES and ToF-SIMS

Yoshimi ABE

Tokyo Institute of Technology

2-12-1 Ookayama, Meguro-ku, Tokyo 152-0033, Japan

Contents

Chapter 1

Introduction

1.1. Present limitations of Practical Surface and Interface Analysis

Present situation in industry

In industry, materials and products, which are required to deal with in the scene of both research & development and manufacturing, have been being downsized every year and every month. Key words of "micro-devices" or "nano-technology" represent the current situation. A schematic diagram of hard disk drive is shown in Fig.1.1 as an example of the current product in which the downsizing in depth scale plays a crucial role. A magnetic layer, where the magnetic signals are recorded, has a thickness below 20 nm. A carbon overcoat with thickness below 5 nm protects the magnetic layer against wear and corrosion induced by the friction with the drive head. A lubricant film of ~1 nm is coated on the overcoat for surface lubrication.

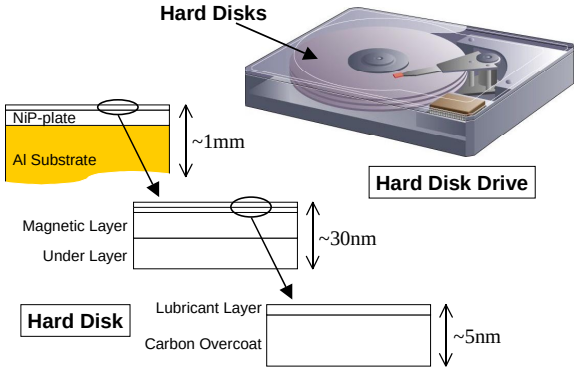

Fig. 1.1. Schematic diagram of hard disk drive (HDD).

Along with the downsizing, high functionality and additional values of the products, which discriminate the product against similar ones of competitors, have been invented mostly as the peculiar functionality on the surface. Therefore, the development of surface sensitive analytical techniques providing comprehensive and spatially resolved information on the surface has been called for in order to characterize the currently-developed high-functional materials.

Survey of popular techniques

In the analytical division in industry, various analytical tools have been used in order to characterize the morphology, elemental composition, vibrational state, chemical bonding state and molecular structure of the practical surfaces.

To make a brief survey of the techniques, the already established popular techniques are tabulated in Table 1.1. In Table 1.1, ten techniques used in my laboratory are listed, and their spatial resolution, information depth and sensitivity for elemental are summarized.

Surface analytical tool map

Fig.1.2 shows the analytical tool map for surface characterization. The horizontal and vertical axes represent the analyzing spot size and detection range, respectively. An analytical tool, which can provide sufficient information with high position sensitivity, is strongly requested for characterization of the progressing practical surfaces. In Fig.1.2 techniques providing morphological, elemental and chemical information are colored in *green*, *blue* and *red*, respectively. Here the chemical information means the information on chemical bonding state and molecular structure on surfaces.

Table 1.1. Survey of the more popular techniques for surface and interface analysis.

Technique	Abbreviation	Probe	Signal	Information*	Spatial Resolution	Information Depth	Sensitivity for elemental
Scanning Electron Microscope	**SEM**	electron	electron	**M**	1 nm	10 nm	NA
Transmission Electron Microscope	**TEM**	electron	electron	**M**	0.1 nm	(tissues)	NA
Atomic Force Microscope	**AFM**	pyramid	atomic force	**M**	0.1 nm	outermost surface	NA
Fourier Transform Infrared Spectroscopy	**FTIR**	photon	photon	**V**	100 µm	1 µm	NA
Raman Spectroscopy	**Raman**	photon	photon	**V**	1 µm	10 nm	NA
Electron Probe Micro Analyzer	**EPMA**	electron	X-ay	M, **E**	1 µm	1 µm	0.01%
X-ray Photoelectron Spectroscopy	**XPS**	X-ray	electron	E, **C**	10 µm	5 nm	0.1%
Auger Electron Spectroscopy	**AES**	electron	electron	M, **E**, (C)	10 nm	5 nm	0.1%
Dynamic Secondary Ion Mass Spectrometry	**D-SIMS**	ion	ion	**E**	10 µm	1 nm	ppm-ppb
Time-of-Flight Secondary Ion Mass Spectrometry	**ToF-SIMS**	ion	ion	E, C, **MS**	1 µm	1 nm	ppm-ppb

*__M__ = morphology, __E__ = elemental, __V__ = vibration, __C__ = chemical state and __MS__ = molecular structure.

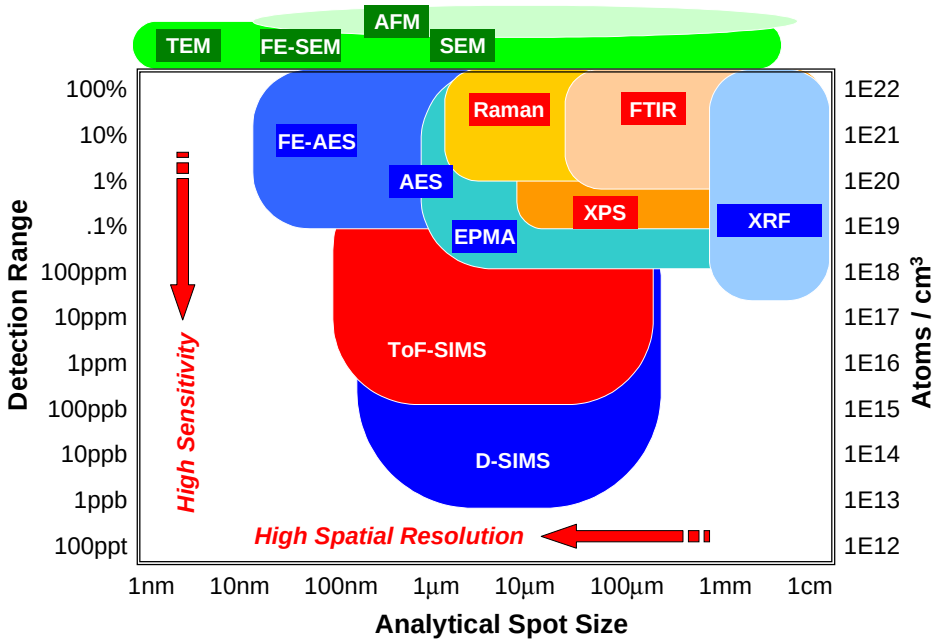

Fig. 1.2. Analytical tool map for surface characterization.

Electron probe techniques

SEM, TEM, EPMA and AES in Table 1.1 are surface analytical techniques using electron beam as a probe. The electron probe techniques are generally characterized by the high spatial resolution. For the imaging purpose, **SEM** is the most popular technique to investigate the surface morphology. More highly spatially resolved images can be obtained by **TEM**, however, this technique requires the pre-treatments including sample thinning in principle.

EPMA (or **EDS**) and **AES** can be used both for the observation of the SEM images and for qualitative analysis of the elements localizing in the target area on the surface. For EPMA measurements, a characteristic X-ray originating from near surface region in the depth range of 1 μm is analyzed. In contrast with EPMA, AES detecting Auger electrons has the smaller information depth of a few nm, depending on the escape depth of detecting signals. These techniques using the electron beam as a probe have a great advantage in reducing the analytical spot size. But the sensitivity is not high enough and is usually above 1000 ppm.

X-ray probe techniques

On the contrary to electron probing techniques, **XPS** has a poorer spatial resolution of 10 μm order. Its typical analyzing area size is as large as FTIR, ranging over 100 μm, because the exciting X-ray source is difficult to be focused into a small analytical spot. In spite of the poor spatial resolution, XPS is still one of the most frequently used techniques among the various surface sensitive one. It is considered to be due to the following reasons: First of all, it can give us not only elemental but also chemical information. Siegbahn, who established the usefulness of XPS for chemical analysis, thus named XPS as ESCA (electron spectroscopy for chemical analysis). Secondly, the X-ray radiation causes little damage on the surface as compared with the radiation of electrons and ions, which allows us to perform less-destructive surface analysis. Thirdly, many supporting data have been accumulated for many substances.

Ion probe techniques

SIMS, one of the ion probing techniques, is less popular than AES and XPS, however, it has a great advantage in sensitivity. In principle, **D-SIMS** dosing high density of primary ions is destructive technique and routinely used to measure the depth profiles of the trace elements such as dopants. In contrast with D-SIMS, the primary ion dose density of **ToF-SIMS** is quite low and the surface is not highly damaged by sputtering. Because of this reason, ToF-SIMS has a unique advantage in detecting the information on the molecular structure of the chemical species on the surface.

Present limitations

Major limitations of practical surface and interface analysis at the present are summarized below.

1) AES equipped with field emission gun (FEG) has the highest spatial resolution and can give the elemental information with the small analytical spot size of 10 nm. But typical use of FE-AES is limited to the elemental analysis.

2) XPS is the most popular technique, and can give the information on elemental composition and chemical bonding state. But its spatial resolution is not sufficiently high to analyze the target area localized to nano-structures on the surface.

3) ToF-SIMS is a newcomer technique and can give the information on molecular structure with moderate spatial resolution and high sensitivity. It has become available since the late 1980’s. ToF-SIMS is expected to be applicable to a variety of materials, however, usefulness of ToF-SIMS has not been fully

explored yet.

Aim of the present study

In spite of many limitations of the already established surface analytical tools, the demand for surface characterization has been extensively increasing. Some of the most important subjects in the field of practical surface analysis are the application to the analysis of modified surface and to the new materials invented on the surface.

This thesis is devoted to presenting the perspective on practical surface and interface analysis by advanced use of AES and ToF-SIMS.

1.2. Advanced Use of AES as a tool for Micro Chemical Analysis

Refinement of AES

AES detects the Auger electrons, which are originating from the specific electron transitions; in the first stage, a core electron is ionized by primary electron irradiation, and in the next stage, core hole state is relaxed through the transition of an electron from an outer shell and the surplus energy is carried by an electron which leaves from the material. Primary electron beam is easily focused and thus the analyzing spot size can be minimized by the use of AES. In the late 1980's, the use of FEG instead of thermionic emission gun was developed, which enables us the micro area analysis with spatial resolution of nm order. By the use of FEG, AES has become a micro elemental analysis with spatial resolution of nm order.

Along with the progress in reducing the spot size, detection system has been refined recently. Some types of modern instruments equipped with concentric hemispherical analyzer (CHA), which can give the spectra with high-energy resolution comparable to that of XPS spectra, have been developed. AES spectra with high-energy resolution are expected to reveal the fine structures, which reflect the chemical states of component atoms. And the improvement of computerized detection system allows us to obtain the direct spectra without any derivation. These refinements will promote the application of AES to chemical state analysis.

Chemical effects on the AES spectra

If a certain element is in some chemical bonding states in a material, chemical effects such as the energy shift and line shape change may appear on the AES spectra as in the case of XPS. Chemical effects are usually viewed as obstacles to perform the quantitative analysis, however, these can be used for chemical state analysis if the peaks of atoms in several chemical states are resolved in spectra by the use of high-resolution AES. At present, there are very few AES studies applied to chemical analysis.

Demands for characterization of surface oxidation

Surface oxidation is one of the most important surface modifications. The oxidation of metal surface is caused by the interaction with oxidizing agents unexpectedly or in a designed manner. The chemisorption of oxygen and the initial oxidation on a clean metal surface have been investigated extremely for the purpose of understanding oxide growth mechanism.

From a practical point of view, it is well known that stainless steels have a dense oxide layer with high Cr content in the surface region, which is responsible for high corrosion resistivity. Magneto-optical media have a thin layer of alloys as a memory layer, which is adjacent to oxide layer on both sides. Such structure should be protected against the interfacial oxidation. Magnetic recording disks

also have a thin layer, which should be protected against wear and corrosion. The magnetic layer of Co-based alloy is separated into small magnetic domains with Cr-rich boundary as a result of designed oxidation during the sputter deposition. Thus, it is important to prove the oxidation behavior of metal surfaces from both fundamental and practical aspects.

It is necessary to understand changes in elemental composition, chemical bonding state and electronic structure in order to elucidate the oxidation process of a material. AES is believed to possess the sufficient potential to characterize these changes and has been widely used to study the oxidation behavior on metal surfaces. The elemental composition in the surface region of around 5 nm depth can be estimated from the peak intensities in the AES spectra. In some cases, along with elemental composition, chemical bonding state and electronic structure of the surface can be deduced from AES line shapes. But the usefulness of AES to the chemical and electronic characterization has not been extended yet.

Advanced use for micro chemical analysis

There are some obstacles in extension of AES to the chemical and electronic characterization of metal surfaces. First, the line shapes of Auger peaks are determined by much more complicated factors as compared with photoelectron lines. Three electrons in an atom participate in an Auger transition and two holes are generated in the final state. Correlation between the two holes substantially complicates the spectral line shapes. Secondly, Auger peaks appear on the giant background of the secondary electrons. Data analysis requires the background subtraction, but the adequate method has not been established in the case of AES. Thirdly, few reference data on the chemical shift are available. Lastly, AES cannot detect hydrogen in principle, which leads to some difficulty in detecting the surface hydroxyl species. The hydroxyl species formed on the surface during or after oxidation process have much influence on properties of oxide surfaces. Regarding the detection of hydrogen and its compound, ToF-SIMS has great advantages.

In spite of many obstacles in application of AES to chemical state analysis, attempts to extract chemical information from the AES spectra are strongly motivated because of its high potential in micro analysis.

1.3. Advanced Use of ToF-SIMS as a tool for Surface Chemical Structure Analysis

A brief survey of ToF-SIMS

ToF-SIMS has come into use since the last 1980's. The secondary ions emitted from the surface are usually generated by impinging of pulsed primary ion beam. Molecular structural information can be obtained because the species of secondary ions are strongly dependent on the initial chemical species on the surface. The primary ion dose is usually lowered below the order of 10^{12} ions/cm^2, which corresponds to 0.1% of the atoms on the surface. Liquid metal ion gun (LMIG) is adequate to reducing the analytical spot size. Thus, ToF-SIMS is also used for imaging.

There are many advantages of ToF-SIMS, as summarized below. For these advantages, ToF-SIMS has been extensively used in the field of practical surface analysis such as, organic contaminant analysis, trace element analysis, failure analysis, trouble shooting.

- molecular structural information
- high surface sensitivity; information depth below 1 nm

- high spatial resolution of sub-μm order by use of LMIG → chemical imaging
- low detection limits; high sensitivity for trace elements, order of ppm-ppb
- high mass resolution with time-of-flight mass spectrometer
- wide mass range → applications to macro molecules
- quick data collection; parallel detection → in-situ monitoring of surface reaction
- less destructive analysis
- insulator analysis by use of charge compensation with flood gun of low energy electrons

Demands for characterization of organic molecules

Some of new material inventions developed on the surface are realized through the harmony with organic molecules. For example, Fomblin molecules whose molecular weight has mono-dispersive distribution around several thousand are coated on the magnetic recording disks as a lubricant film with thickness below 1 nm. Some molecules are chemically bonded to the surface through the functional end groups. The properties of these molecules such as molecular weight, monomer ratio, functional end group, film thickness, uniformity of layer structure and bondability to the surface are important factors to certify the proper functionality of the disks. The macromolecules are too large to evaluate their properties by the conventional surface analytical techniques such as FTIR or XPS. For instance, Fomblin Z-DOL molecule with molecular weight of 4000 and monomer ratio of 1 has 21 methylene units (CF_2O), 21 ethylene units (C_2F_4O) and 2 end group units (CF_2CH_2OH). The proportion of the number of end group units that are deeply related with the chemical bonding to the surface is only 4-5%. There are only two hydroxyl groups in the molecule of 4000 amu, which is composed of 248 atoms. A new surface analytical tool that can elucidate the structure of a part of a molecule, which is responsible for the functionality, as well as the whole molecular structure is strongly requested.

Coating of nanocrystals with phosphine oxide molecules with alkyl long chains is effective to improve the optical properties by passivating surface nonradiative recombination sites. Trioctylphosphine oxide has molecular weight of 386, which is one order smaller than Fomblin. But the molecules are still large to characterize their whole chemical structure on the surface by the conventional techniques. Molecular-structure sensitive techniques are required at present situation.

1.4. Outline of This Thesis

This Thesis is divided into 7 chapters. General introduction is described in this **chapter 1**. The following two chapters are devoted to the general description on experimental setups including their principle and instrumentation: **chapter 2** for AES and **chapter 3** for ToF-SIMS. Results and discussion is presented in the following three chapters. The **chapter 4** describes results of the study on the initial oxidation of the metal surfaces by three techniques of conventional AES, HR-AES and ToF-SIMS. The **chapter 5** presents the typical applications of ToF-SIMS to magnetic recording disks. In **chapter 6**, a comparable study of nanocrystals thin films by XPS and ToF-SIMS is presented. The last **chapter 7** summarizes the results obtained here as a perspective on the practical surface and interface analysis by advanced use of AES and ToF-SIMS.

Chapter 2

AES Experimental

2.1. Principle of AES

Secondary electron emission [2]

When a solid surface is irradiated by an electron beam of the energy in the KeV range, various processes take place in the surface region [1-7]. Figs.2.1.1, 2.1.2 and 2.2 show examples of energy distributions of emitted electrons induced by electron irradiation. At the energy of the incident electrons, there is a large peak corresponding to the elastically scattered electrons. An example of energy distribution of electrons emitted from GaAs smooth surface by the irradiation of 2 keV beam is shown in Fig.2.1.1 (with CAE mode; described in the following section 2.3). The width of an elastic peak is determined by the energy spread in the incident electron beam. The elastic peak intensity depends on the atomic number, as shown in Fig.2.1.2. They can be used for the technique as elastic peak electron spectroscopy (EPES).

In addition to the elastic peak, there exists smooth background in the lower kinetic energy region. The background is formed by inelastically scattered electrons, which are called “secondary electrons”. On top of the background, a series of smaller and broader peaks whose intensity decreases successively away from the elastic peak are observed in spectra. These are the electron energy loss structures due to the excitation of plasmons or inter-band transitions. Observation of these loss features is called reflective electron energy loss spectroscopy (REELS). An example of REELS spectra is shown in Fig.2.1.2. While the plasmon loss peaks periodically appear in the Al spectrum, characteristic loss peaks due to inter-band transition are dominantly observed in the spectra of 3d transition metals.

At the lowest energy offset region it can be seen another large peak, which are produced by a cascade process and called true secondary peak. They are utilized for the observation of surface morphology by scanning electron microscope (SEM).

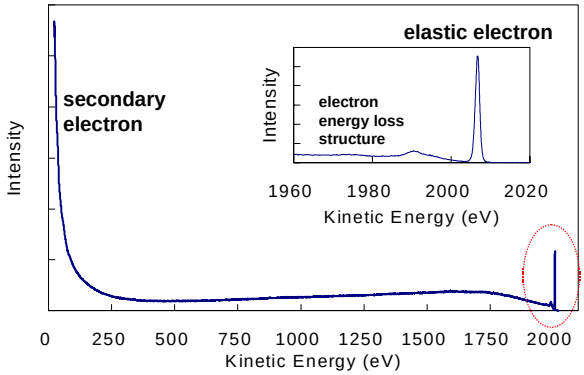

Fig. 2.1.1. An example of secondary electron spectrum emitted from GaAs obtained by 2 keV beam.

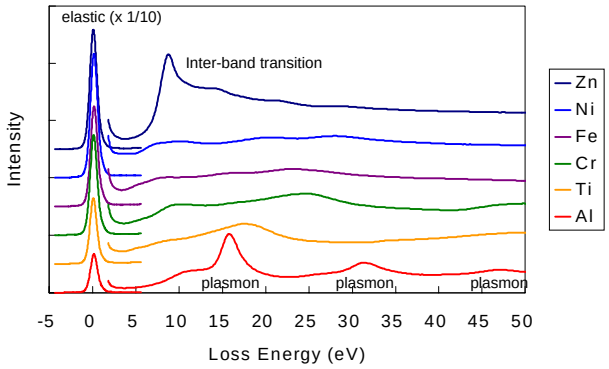

Fig. 2.1.2. Variation in the REELS spectra of 3d transition metals and Al obtained by 2 keV beam.

Between the elastic and the true secondary peak, other features due to Auger emission are often observed. An example of Auger peaks emitted from GaAs smooth surface by the irradiation of 10 keV beam is shown in Fig.2.2 (with CRR mode; described in the following section 2.3). Auger emissions are observed in the kinetic energy region of 1000-1300 eV, which are originated from the

surface Ga and As atoms. The details on the Auger process will be described below.

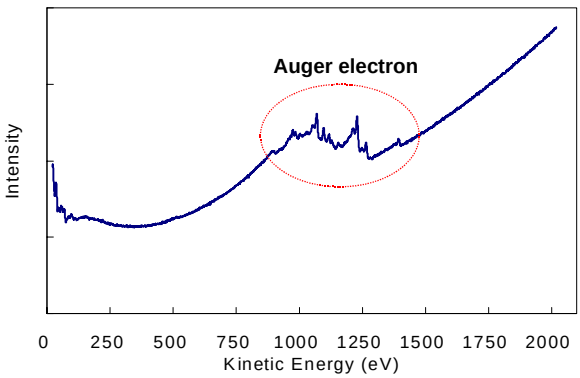

Fig. 2.2. An example of secondary electron spectrum emitted from GaAs obtained by 10 keV beam.

Auger process [2]

Pierre Auger discovered Auger electrons in a cloud chamber in 1920's [1]. Fig.2.3 shows a schematic diagram of the Auger emission process in solids. The ground state of an atom is shown in Fig.2.3(a). When a primary electron of energy E_p which is high enough to ionize a K electron impinges the atom, a hole is created in the core level K. Subsequently a core hole state is relaxed by filling the hole via a transition from an outer level, for example, a L_1 level (Fig.2.3(b)). As a result of that transition, the excess energy of $(E_K - E_{L1})$ emerges. The excess energy is carried by either of two different ways. One is a characteristic X-ray emission of the energy of $(E_K - E_{L1})$, and the other is an Auger electron emission with energy of $(E_K - E_{L1} - E_{L2,3})$.

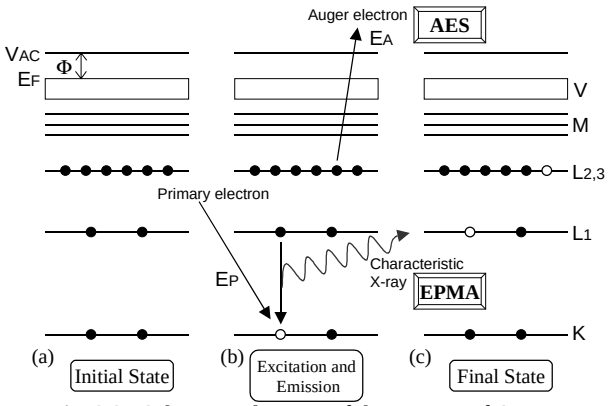

Fig. 2.3. Schematic diagram of the process of Auger emission in solids.

The Auger transition represented in Fig.2.3 is named $KL_1L_{2,3}$ in the conventional *j-j* coupling scheme. The nomenclature used in AES and corresponding to those used in XPS are tabulated in Table 2.1.

Table 2.1. X-ray and spectroscopic notation.

X-ray level	Spectroscopic level
K	$1s_{1/2}$
L_1	$2s_{1/2}$
L_2	$2p_{1/2}$
L_3	$2p_{3/2}$
M_1	$3s_{1/2}$
M_2	$3p_{1/2}$
M_3	$3p_{3/2}$
M_4	$3d_{3/2}$
M_5	$3d_{5/2}$

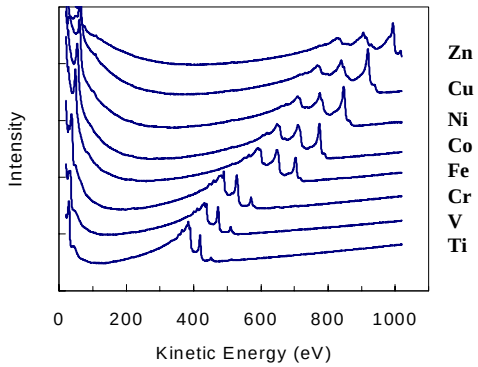

Fig. 2.4. Variation in the AES spectra of 3d transition metals.

Characteristic Auger lines [2]

The energy of the ejected Auger electron in the example of Fig.2.3 is

$$E_{KL1L2,3} = E_K - E_{L1} - E_{L2,3}^* \qquad (1)$$

where $E_{L2,3}^*$ is the binding energy of the $L_{2,3}$ level in the presence of a hole in L_1 level, which is different from the ground state energy of $E_{L2,3}$. Eq.(1) shows that the Auger energy is characteristic of each element, because there being no two elements with the same set of atomic binding energies. Thus analysis of Auger electrons leads immediately to elemental identification. Examples of AES for 3d transition metals are shown in Fig.2.4. It can be seen the characteristic fingerprint of the LMM triplet, consisting of the transitions of L_3VV,

$L_3M_{2,3}V$ and $L_3M_{2,3}M_{2,3}$ in the series of 3d transition metals.

Information depth and inelastic mean free path

The inelastic mean free path (IMFP) of typical Auger electrons in solids is the order of 1-3nm. This means that only Auger electrons generated in the surface region can emit from the surface without suffering inelastic scattering. Thus AES can be used as a surface sensitive technique. The inelastically scattered Auger electrons will make a giant background on the spectrum. Typical IMFP values for C, Al, Cu and Au evaluated by Tanuma *et al.* [8-11] are shown in Fig.2.5. The surface sensitivity of AES varies with the kinetic energy of the ejected electron, and is usually highest in the energy range of 50-200 eV [3].

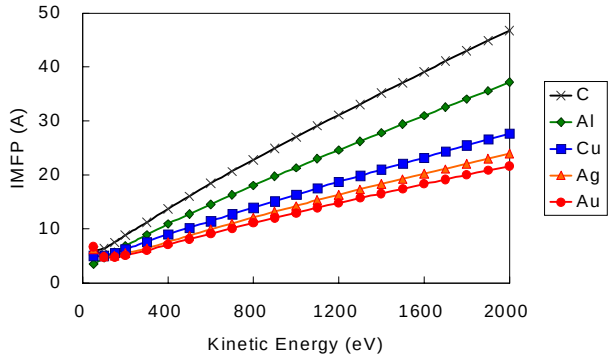

Fig. 2.5. Calculated IMFP values in some materials as a function of kinetic energy.

Chemical effects [2]

In Auger spectra, fine structures of peaks are often resolved both for metals and non-metals. The fine structures are induced either by chemical effects or by final state effects [2,12-15].

Chemical effects arise from the change in electrostatic potential on an atom when valence electron charge density is accepted or withdrawn from the atom, as in the case of chemical shifts in XPS. The binding energy of electrons in a core level being ionized can alter with the change in chemical environment, leading to a similar shift in the consequent Auger transition. The number of studies of Auger lines in the XPS spectrum have increased significantly in recent years, particularly in the context of "Auger parameter" measurements for chemical state determination.

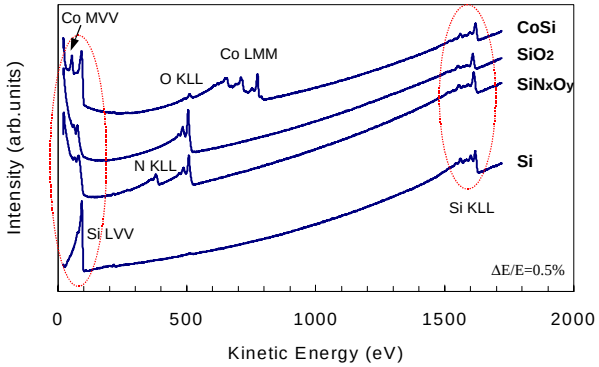

Fig. 2.6. Variation in the AES wide-scan spectra from some Si compounds.

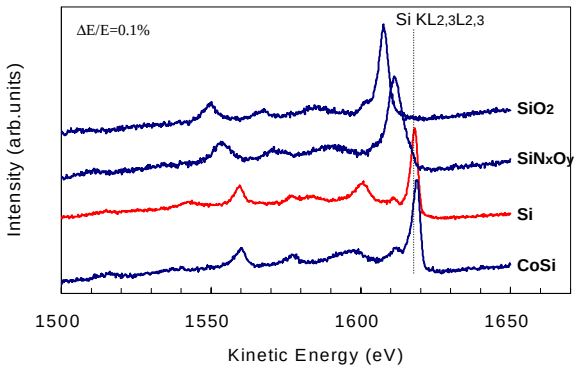

Fig. 2.7. Variation in the AES narrow-scan spectra of Si KLL from some Si compounds.

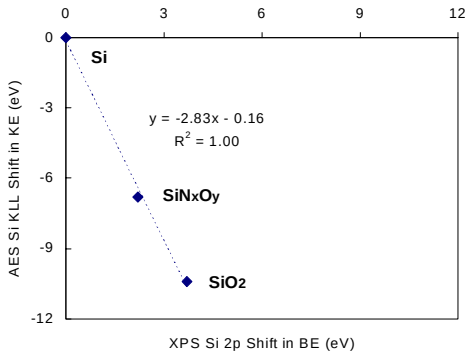

Fig. 2.8. Correlation of the energy shift between XPS and AES for some Si compounds.

Examples of the chemical shifts in the AES spectra of some Si compounds are shown in Fig.2.6. It can be seen that the Si KLL Auger line shape is unique to each compound, as

shown in Fig.2.6. But the usual energy resolution of 0.5% for the conventional AES is not sufficient to characterize the energy shift, because ΔE is reached at ~8 eV at this condition. In the highly energy-resolved spectra we can identify the chemical shifts more precisely, as shown in Fig.2.7, with the energy resolution of 0.1%. The energy shift of Si KLL Auger lines observed for some Si compounds are plotted as a function of Si 2p photoelectron line shift in Fig.2.8. In accordance with the previous report [15], the observed chemical shift of AES is greater than that of XPS (Fig.2.8).

When an Auger process results in at least one vacancy in the valence levels then the intensity distribution of the lines in the Auger series can vary strongly from one compound to another. In effect the valence band or molecular orbital structure is convoluted into the Auger peak structure.

2.2. Field Emission Gun for Primary Electron Source

There are two main components in an AES facility: a primary electron gun and an electron energy analyzer.

There are two types of electron source, one is the thermionic type and the other is the field emission type. The latter has been getting much more common since the late 1980's.

Thermionic emission [2]

Thermionic emission is generated by heating a material to a temperature high enough to give some electrons sufficient energy to overcome the work function barrier at the surface. The higher the temperature rises, the greater the thermionic current becomes. The thermionic emission has a lower brightness, but is much easier to make and to replace, and can be used over a wider range of emission currents. Tungsten is by far the most commonly used material for thermionic filaments. Even nowadays the W filament is still widely used, though the lanthanum hexaboride (LaB_6) has taken over the W-cathode as a cathode of higher brightness and high stability since the early 1970's [16]. The LaB_6-cathode is now widely used in the electron beam instruments like AES and EPMA.

Field emission [2]

Field emission is obtained by reduction of the height of the work function barrier through application of a high electrostatic field. In this case, electrons escape from the surface by tunneling through the barrier, which enables us to obtain an electron beam from a tip even at room temperature. The field is enhanced to the necessary strength by shaping the emitter into the form of a sharp point whose apex radius is of the order of 20 nm.

Because the emitting area of a field emission source is so small, and the emission is concentrated in a small solid angle, the current density per unit solid angle is much higher than that obtainable from a thermionic source. Thus, the field emission sources are known as 'high brightness' sources. They are used in electron sources designed to produce a finely focused electron beam on the sample surface.

Zirconiated W-cathode, Zr-O / W(100) cathode, has been extensively used since 1980's as the most popular high brightness cathode of high stability in modern electron beam instruments [16]. By use of this cathode the electron beam size is reduced less than 15 nm.

Beam energy and its energy spread

For AES the role of the incident electron beam is limited to the ionization of core levels, which initiates the Auger process. For this purpose the beam is not needed to be

precisely monochromatized, provided it is high enough to ionize all core levels of interest with efficiency both high and uniform. The electron ionization cross-section rises steeply from threshold to a maximum at about 4-5 times the ionization energy of a core level, which implies that the exciting energy should be at least 4-5 times higher than that of the ionization energy. Since the energy dependence of the cross-section becomes fairly flat beyond the maximum, the incident energy is usually set to a value high enough to ionize all relatively shallow core levels with approximately the same efficiency. The commonly used energy range is 5-10 keV.

Because the energy of the incident electrons does not enter the expression for the Auger energy, the energy spread in the incident electron beam does not affect the quality of AES. The energy spread is greater than the Boltzman thermal spread of 0.3-0.5 eV and its typical value is around ~1 eV, as shown in Fig.2.1.2. The energy spread of the field emission is smaller than that of the thermionic emission because of the lower operating temperature. Thus, the field emission plays an important role especially for REELS measurements, which require the shallow energy spread of the incident electrons in order to resolve the fine energy loss structure.

2.3. Electron Energy Analyzer

The analysis of electron energy is the 'heart' of electron spectroscopic techniques like AES. At present, two types of electron energy analyzer, the cylindrical mirror analyzer (CMA) and the concentric hemispherical analyzer (CHA), are dominantly used. Within only a year of the origination of AES, CMA had appeared and it has been used ever since as the principal energy analyzer for AES. On the other hand, CHA has been used from the very beginning in XPS. Recently, the modern AES system equipped with CHA has been developed.

CMA [2,3]

As mentioned above, it was realized soon after the origination of AES that CMA was suitable for AES. A diagram of CMA is shown in Fig.2.9. It consists of two coaxial cylinders of radii R_1 (inner) and R_2 (outer). Usually the inner cylinder is kept at ground potential and a potential of $-V$ is applied on the outer. Electrons emitted from the specimen aligned on the axis move in field-free space towards a mesh-covered annular aperture in the inner cylinder, those within the angular spread passing into the space between the cylinders. Those electrons of a particular kinetic energy E_0 are deflected by the potential on the outer cylinder to go through a second mesh-covered aperture and are focused at the detector, also aligned on the axis. Scanning the potential $-V$ on the outer cylinder of CMA gives directly the energy distribution of electrons passing through it. But, because the transmission of CMA varies as E, the recorded distribution is not N(E) but E*N(E). Thus CMA is operating only with the constant retard ratio mode, mentioned below.

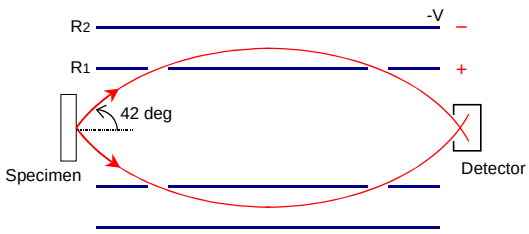

Fig. 2.9. Schematic diagram of a CMA.

The great advantage of CMA as far as AES is concerned is its very high solid angle of acceptance, leading to high transmission.

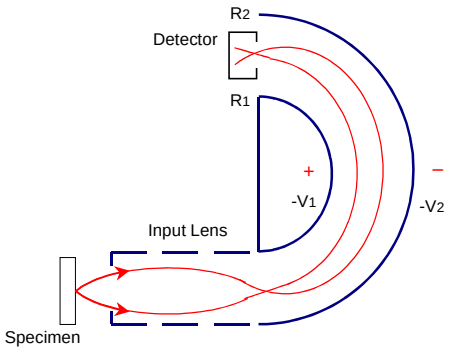

Fig. 2.10. Schematic diagram of a CHA.

CHA [2,3]

A diagram of CHA is shown in Fig.2.10. CHA consists of two hemispheres of radii R_1 (inner) and R_2 (outer) positioned concentrically. Potentials $-V_1$ and $-V_2$ are applied to the inner and outer hemispheres, respectively. The median equipotential surface between the hemispheres has radius R_0 and the source and focus are colinear with the center of curvature.

For optimum design the transmission of a simple CHA when used for AES will always be less than that of a CMA for the same energy resolution. Operating with input lens systems can improve the less transmission. In the modern AES instruments, CHA can be used for AES in harmony with the improved input lens. CHA combined with the input lens also enables us the variety of operating mode: the constant retard ratio mode and the constant analyzer energy mode, mentioned below.

Two operating modes

There are two operating modes of CHA for AES measurements: the “constant retard ratio (CRR)” mode and the “constant analyzer energy (CAE)” mode. For CMA, the CRR mode is only available. The retard ratio (RR) means the reducing ratio of the original kinetic energy (KE) and the energy passing in the analyzer (pass energy, PE).

$$RR = KE / PE$$

In the CRR mode, $\Delta E/E$ is constant, that is to say, ΔE is proportional to E. On the contrary, ΔE is independent of E and constant through the whole analyzing energy range in the CAE mode.

For XPS, the peak width defined as the full width at half-maximum (FWHM), ΔE, is a convolution of several contributions as follows:

$$\Delta E^2 = \Delta E_n^{\,2} + \Delta E_p^{\,2} + \Delta E_a^{\,2}$$

where ΔE_n is the natural or inherent width of the observed peak, ΔE_p is the width of the photon source and ΔE_a is the analyzer resolution, all expressed as FWHM. Here it is assumed that all components have a Gaussian line shape. Because the energy of the incident electrons does not enter the expression for the Auger energy, the energy spread in the incident electron beam is unimportant for AES. Thus the Auger peak width of ΔE is described as follows:

$$\Delta E^2 = \Delta E_n^{\,2} + \Delta E_a^{\,2}.$$

The analyzer contribution is the same for all peaks in the spectrum when the analyzer is operated in the CAE mode, but varies across the spectrum when the analyzer is operated in the CRR mode.

The CRR mode is frequently used for AES measurements because the decreasing energy resolution with the increasing KE is adequate to detect the small signal due to the Auger emission. In general, energy resolution and sensitivity are usually trade-off. On the other hand, the CAE mode is frequently used for XPS measurements. The constant energy resolution through the spectrum is suitable for the line shape analysis and the available energy resolution is higher in the CAE mode.

Energy resolution

The observed FWHM for 1 keV

elastic peak is shown in Fig.2.12 as an example of the energy resolution obtained with various modes. With the CRR mode, an increase in RR leads to the higher energy resolution. There is the following relationship between RR and the energy resolution in this AES system used.

$$\Delta E/E\ (\%) = 2 / RR$$

With the CAE mode, the decrease in the pass energy improves the energy resolution. The correlation between the pass energy and the FWHM is shown in Fig.2.13. For both modes, the obtained energy resolution is a simple function of the pass energy. The pass energy of the CAE mode is mostly smaller than that of the CRR mode.

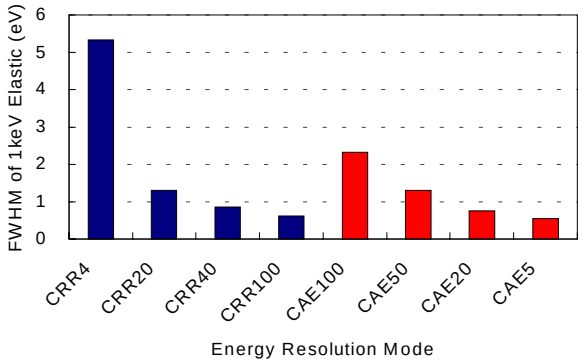

Fig. 2.12. Comparison of the energy resolution for 1 keV elastic peak among the various modes.

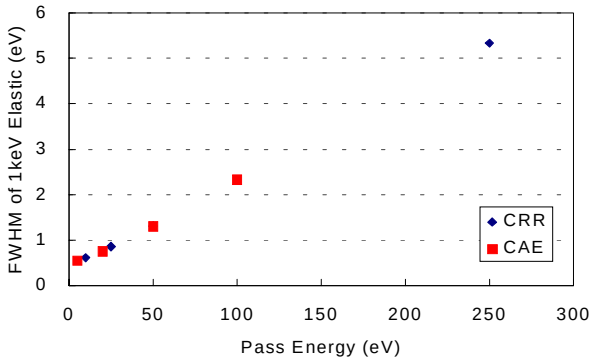

Fig. 2.13. The energy resolution for 1 keV elastic peak as a function of the pass energy.

The typical properties for two electron energy analyzers are present in Table 2.2. In order to demonstrate the much variety of energy resolution modes for CHA, the variation in the AES spectra of Si KLL from elemental Si with CRR = 4 (0.5%), 10 (0.2%), 20 (0.1%) and 40 (0.05%) is shown in Fig.2.14. It can be seen the fine structure at the tail of Si $KL_{2,3}L_{2,3}$ at 1611 eV in the highly energy-resolved spectra, which are obtained with the retard ratio above 20. The peak situated at 1611 eV is originating from ^1S state, well separated from the main peak originating from ^1D state [2]. It should be noticed that two peaks from ^1S and ^1D can not be energy-resolved with the usual energy resolution of 0.5% in spite of their large energy separation of ~7 eV. Highly energy-resolved AES spectrum will give a new insight into the spectral interpretation.

Table 2.2. Typical properties for electron energy analyzers.

Analyzer	CMA	CHA
Operating modes	CRR	CRR and CAE
Energy resolution	0.5-0.6%	0.05-1.0%
Variety of energy resolution modes	Few	Much
Transmission	High	Low (without input lens)

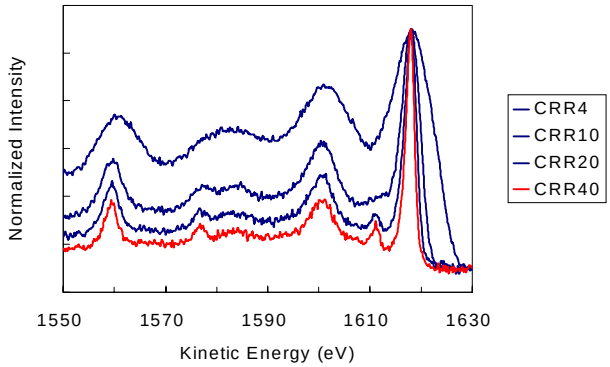

Fig. 2.14. Variation in the AES narrow-scan spectra of Si KLL from elemental Si with various energy resolution.

Energy calibration

In order to discuss the small chemical shift observed in the Auger lines, the energy calibration becomes substantially important. The standardization procedure for the calibration method of kinetic energy scale for AES has been progressing by ISO [17]. According to the planning procedure, the observed kinetic energy scale should be calibrated through the measurements of

reference materials, pure Cu, Al or Au, and referring the peak position of the Auger transitions of Al KLL, Cu MVV, Cu LMM or Au MNN. The recommended calibration kinetic energy for Auger electron peaks referred to the Fermi level in the direct mode at high energy resolution using 5 keV or 10 keV electron beam energies has been proposed by Seah [18,19]. The reference values are tabulated in Table 2.3.

To qualify the observed kinetic energy in the highly energy-resolved AES spectra reported in this work, the calibration of kinetic energy scale is performed. The variations in the AES spectra of Al KLL, Cu LMM and Au MNN with various energy resolution of CRR = 2 (1%), 4 (0.5%), 8 (0.25%), 10 (0.2%), 20 (0.1%) and 40 (0.05%) are shown in Fig.2.15. While in the Al KLL and Cu LMM spectra the peak positions seem to be almost independent of the energy resolution, the peak positions of Au MNN tend to move toward the lower kinetic energy with increasing energy resolution. Thus, for Au MNN only the data obtained with high-energy resolution below 0.1% should be used for the energy calibration [20]. From the energy differences between the observed values and the reference ones, the spectrometer offset function [21] is estimated and shown in Fig.2.16. The obtained equation of y = 0.0012x - 0.5302 can be used for the calibration of kinetic energy scale of the AES instrument used.

Table 2.3. The reference values for the peak positions on the kinetic energy scale [17].

Auger transition	Kinetic energy (eV)
Cu $M_{2,3}VV$	62.37
Cu L_3VV	918.69
Al $KL_{2,3}L_{2,3}$	1393.09
Au $M_5N_{6,7}N_{6,7}$	2015.80

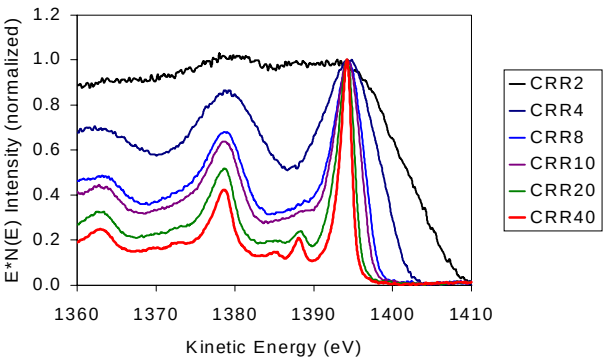

Fig. 2.15.1. Variation in the AES narrow-scan spectra of Al KLL from Al foil with various energy resolution.

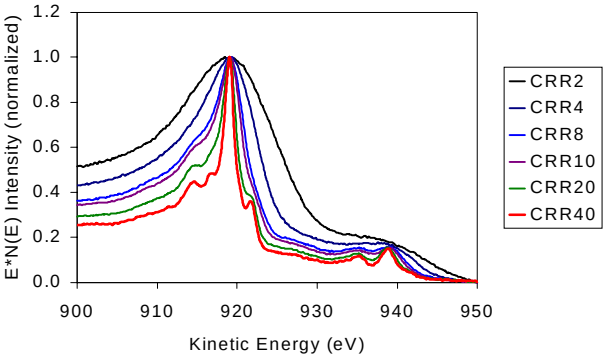

Fig. 2.15.2. Variation in the AES narrow-scan spectra of Cu LMM from Cu sheet with various energy resolution.

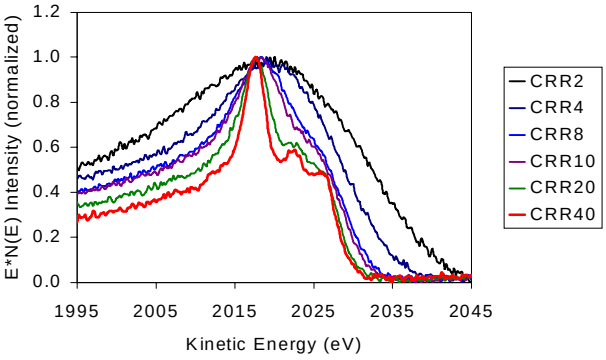

Fig. 2.15.3. Variation in the AES narrow-scan spectra of Au MNN from Au sheet with various energy resolution.

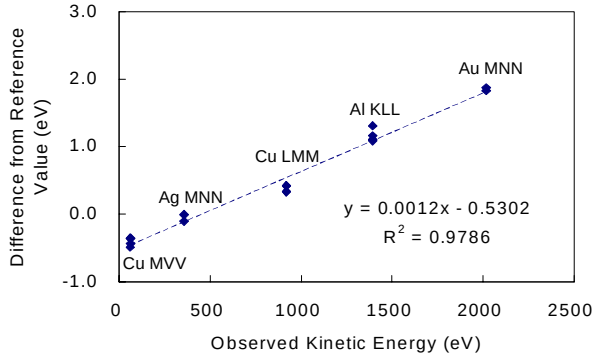

Fig. 2.16. Obtained offset function for the energy calibration of AES spectrum.

2.4. Instrumental Systems Used

In this work, two commercially available instruments are used for AES experiments. Typical measuring conditions are tabulated in Table 2.4 and 2.5.

Table 2.4. Typical measuring conditions for electron sources used.

System	JAMP-30	Microlab 310-F
Emission source	LaB_6	FEG
energy	5 keV	10 keV
current	200 nA	9 nA
sampling area	10 μmϕ	10 μm x 10 μm
incident angle	75 degree	30 degree

Table 2.5. Typical measuring conditions for electron energy analyzer used.

System	JAMP-30	Microlab 310-F
mode	CRR	CRR
energy resolution	0.6%	0.1-0.5%
detection angle	15 degree	30 degree

JEOL, JAMP-30

This system is the conventional AES system equipped with the LaB_6 thermionic emission gun and CMA.

- The primary electron current of μA order is available and necessary to obtain the spectra.
- Its CMA is composed of only the upper half parts of the whole co-cylindrical mirrors. The angle between the electron gun and the CMA axis is 90 degree. In order to detect the sufficient signal the specimen is needed to tilt over 60 degree.
- Auger detection is provided in a derivative mode, differentiated with lock-in amplifier. The modulation is set to $5V_{p\text{-}p}$.

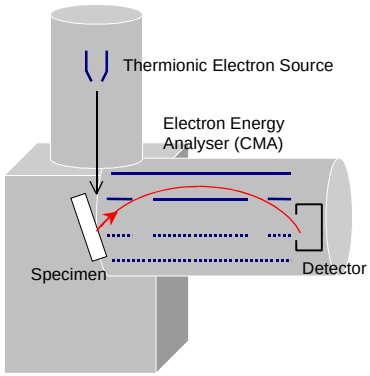

Fig. 2.17. Schematic diagram of JEOL, JAMP-30.

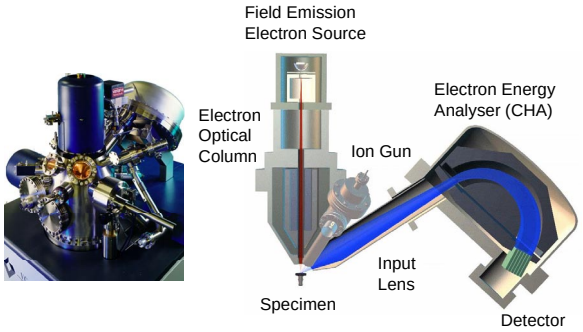

Fig. 2.18. Schematic diagram of VG, Microlab 310-F.

VG, Microlab 310-F

This system is the modern system equipped with FEG and CHA.

- The primary electron current of nA order is available up to 100 nA. The current range is lower than the thermionic emission, which is necessary to reduce the beam size effectively.
- The CHA is combined with the input lens system. The angle between the electron gun and the CHA is 60 degree.
- Auger detection is provided in a direct mode without any derivation. In order to count the smaller signal excited by the smaller current of nA order, five channeltrons are used in the detection system.

References

[1] P. Auger, J. Phys. Radium, 6, 205 (1925).
[2] Eds. D. Briggs and M. P. Seah, Practical Surface Analysis, 2nd ed., Vol. 1, Wiley, Chichester (1990); 合志陽一, 志水隆一 監訳, 表面分析(上・下) -基礎と応用-, アグネ承風社 (1990).
[3] M. Prutton, Introduction to Surface Physics, Oxford University Press, Oxford (1994).
[4] 志水隆一, 吉原一紘 編, ユーザーのための実用オージェ電子分光法, 共立出版 (1989).
[5] 大西孝治, 堀池靖浩, 吉原一紘 編, 固体表面分析 I, 講談社 (1995).
[6] 日本表面科学会 編, 表面分析技術選書 オージェ電子分光法, 丸善 (2001).
[7] 日本表面科学会 編, 表面分析技術選書 X 線光電子分光法, 丸善 (1998).
[8] S. Tanuma, C. J. Powell and D. R. Penn, Surf. Interface Anal., 11, 577 (1988).
[9] S. Tanuma, C. J. Powell and D. R. Penn, Surf. Interface Anal., 17, 911 (1991).
[10] S. Tanuma, C. J. Powell and D. R. Penn, Surf. Interface Anal., 17, 927 (1991).
[11] S. Tanuma, C. J. Powell and D. R. Penn, Surf. Interface Anal., 21, 165 (1993).
[12] 二瓶好正, 日本化学会 編, 化学総説 電子分光, 16, 217 (1977).
[13] H. H. Madden, Surf. Sci., 126, 80 (1983).
[14] D. E. Ramaker, Critical Reviews in Solid State and Materials Sceneces., 17, 211 (1991).
[15] T. Sekine, N. Ikeo and Y. Nagasawa, Appl. Surf. Sci., 100/101, 30 (1996).
[16] R. Shimizu, e-J. Surf. Sci. Nanotech., 1, 106 (2003).
[17] 橋本哲, 田沼繁夫, J. Surf. Anal., 9, 69 (2002).
[18] M. P. Seah, G. C. Smith and M. T. Anthony, Surf. Interface Anal., 15, 293 (1990).
[19] M. P. Seah and I. S. Gilmore, J. Electron Spec., 83, 197 (1997).
[20] 阿部芳巳, J. Surf. Anal., 9, 185 (2002).
[21] 藤田大介, 吉原一紘, 表面科学, 14, 429 (1993).

Chapter 3

ToF-SIMS Experimental

3.1. Principle of ToF-SIMS

Secondary ion emission [1]

When a solid surface is bombarded with ions in keV range, various processes take place in the surface region [1-9]. The incident ion may penetrate to a certain depth into the solid and transfer its energy to the lattice atoms. Further impacts distribute this energy to an extended lattice zone. A fraction of this energy reaches the surface and it can induce the emission of a surface particle, which may be an atom or a cluster of atoms in a charged or neutral state. The charged particles are called "secondary ions". Above process is schematically shown in Fig.3.1 [1].

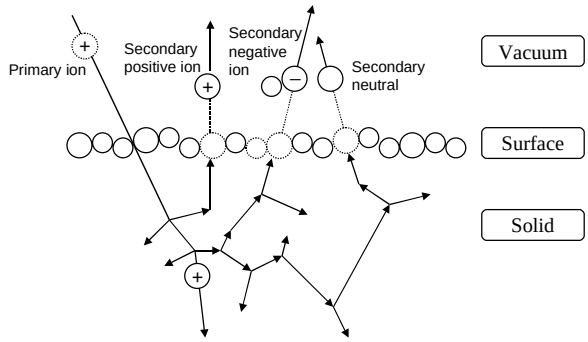

Fig. 3.1. Schematic diagram of the process of secondary ion emission in solids.

Secondary ion mass spectrometry is primarily based on the fact that bombardment of surfaces by ions of some keV energy induces not only the emission of atoms but also the emission of intact molecules on the surface.

The major portion of emitted secondary particles is neutrals and only a fraction of 10^{-6} - 10^{-1} of the total is positively or negatively charged secondary ions [9]. At present the desorption mechanism of secondary particles from elemental targets is fairly well understood [10]. However, the mechanisms of the emission of charged particles and of the emission of molecular species is still in dispute. According to the linear transport theory introduced by Sigmund [10], the impact energy of the primary ion is transformed into movement of target atoms, which results in "collision cascade". A part of the energy is transported back to the surface, and its amount may be sufficient to overcome the surface binding energy of the respective atomic and molecular particles. Therefore SIMS is a very surface sensitive analytical technique. The charge state of the sputtered particles depends largely on the chemical environment (matrix effect), which in general complicates a direct quantification of SIMS results.

Chemical structure information [9]

Ions originating from elemental targets can be positively or negatively charged depending on their electron configuration in the outermost electron shell. Molecular species can be emitted intact if their mass is below 10000 amu. In this case ionization occurs via attachment of protons, salts and metals or loss of hydrogen and small functional groups. Fragmentation leads to charged smaller ions, some of them are called "fingerprint ions", which are characteristic of the investigated molecule. Existence of such ions enables us to investigate larger molecules whose ionization channel forming intact molecule is absent.

An example for a ToF-SIMS spectrum is presented in Fig.3.2, in which the positive spectra of some polymers are shown. Fig.3.2 shows three spectra obtained from the typical polymer films of polyethylene terephthalate (PET), Nylon-6 and polytetrafluoroethylene (Teflon). In accordance with the surface composition of each polymer, the fragments of

oxygen-including hydrocarbons, nitrogen-including hydrocarbons and fluorocarbons are dominantly observed in each spectrum of PET, Nylon-6 and Teflon, respectively. The fragments originating from the repeating units are also observed: $C_{10}H_9O_4^+$ for PET ([-OOC-C_6H_4-COO-C_2H_4- + H]$^+$) and $C_6H_{12}NO^+$ for Nylon-6 ([-NH(C_5H_{10})CO- + H]$^+$).

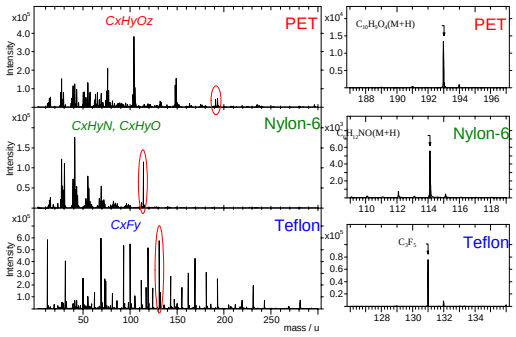

Fig. 3.2. Positive ToF-SIMS spectra from various polymer films of PET, Nylon-6 and Teflon.

Surface damage [9]

The ion bombardment of the surface and the formation of the collision cascade lead to the destruction of the molecular integrity of the sample, not only at the surface, but also in deeper layers. In order to obtain molecular information of the intact surface the primary ion bombardment has to be lowered to such an extent that the bombardment induced changes in surface chemistry become negligible. For surface analysis, "static SIMS" conditions must be employed, i.e. the spectra must be acquired during the accumulation of a total ion dose which is significantly less than the dose required to cause damage to the surface [11].

On the other hand, high primary ion doses are used to subsequently erode the surface for the "dynamic SIMS" mode. Monitoring of the desorbed secondary ions as a function of time then leads to a depth profile of the elements present in the sample. Almost no information on organic species can be expected under dynamic SIMS conditions. The highest tolerable primary ion dose for obtaining molecular information can be defined as follows [9]: If σ is the area at the surface which on average is affected by a primary ion, so-called "disappearance cross section" or "damage cross section", and *A* is the totally bombarded area then one can write for low primary ion dose densities:

$$PID \times \sigma << A$$

or

$$PIDD << 1/\sigma$$

where PID means the primary ion dose and PIDD means the primary ion dose density.

The analysis of organic material is limited to the uppermost monolayer due to the destruction introduced by the collision cascade. The maximum intensity can be expected if the complete monolayer is removed. The PID necessary for a complete removal of the uppermost monolayer is depending on the disappearance cross section σ of the secondary ion species of interest. With *A* of the totally bombarded area one gets

$$PID \times \sigma = A$$

or

$$PIDD = 1/\sigma$$

The σ can be determined by plotting the detected signal intensity N_D against the applied PIDD:

$$N_D(PIDD) = N_D(0) \times \exp(-\sigma \times PIDD)$$

Then the σ can be calculated from the slope of the respective curve, so-called "dose profile".

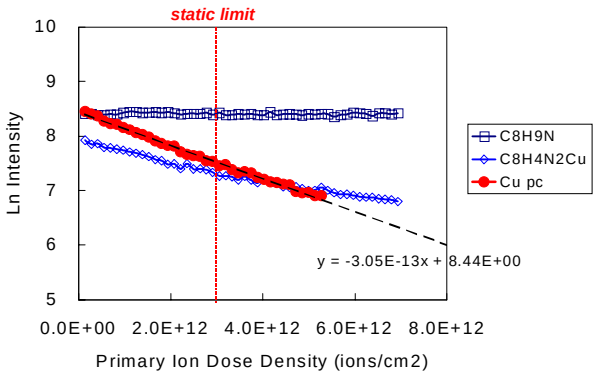

Fig. 3.3. Dose profile obtained from Cu phthalocyanine (pc). Primary ion conditions: Au^+, 25 kV, 0.5 pA, 150 x 150 um^2.

Typical dose profile obtained from Cu phthalocyanine (Cu pc) is shown in Fig.3.3. The intensity of its molecular ion ($M+H^+$) is decreasing with increasing PIDD. The conditions of primary ion gun are energy of 25

keV, current of 0.5 pA, and raster size of 150 x 150 μm^2. The σ of Cu pc for the conditions used is estimated at 3 x 10^{-13} cm^{-2} and the static limit is considered as around 3 x 10^{12} ions/cm^2. Typical values for σ are in the order of 10^{-13} ~ 10^{-16} cm^{-2} [12-14] depending on the sample material and bombardment conditions. Therefore the static SIMS limit at worst is in the order of 10^{12} ions/cm^2.

3.2. Liquid Metal Ion Gun for Primary Ion Source

There are two main components in the SIMS facility: a primary ion gun and a mass spectrometer.

Ion sources [5]

In static SIMS we are concerned to have high surface sensitivity with minimal surface damage. The bombardment of the surface may generate additional surface chemical modification, which can also be regarded as the damage. In order to minimize surface chemical modification, inert gas ion gun, argon or xenon, had been normally used. But it is not possible to generate gas-phase based ion guns with adequate intensity having beam diameters less than 1 μm.

In the 1980s, liquid metal ion gun (LMIG) has been developed to obtain imaging SIMS. LMIG are widely used in Focused Ion Beam Systems (FIB) for micromatching applications in microelectronics industry and TEM / SEM sample preparation [16]. It is capable of delivering adequate beam current into 50 nm beam diameter because of its high brightness. These sources are typically metals that are liquid near room temperature, for example, gallium and indium. A highly focused ion beam is also suitable for ToF-SIMS.

LMIG [15]

A liquid metal ion source consists of a tungsten tip covered with a metal film with a tip radius of about 10 μm. The tip is heated to a temperature above the melting point of the metal. When a positive high voltage is applied to the tip, liquid metal is flowing to the tip and forms a so-called “Taylor cone” by the balance between electrostatic forces and surface tension. On the cone a protrusion of a few nm in diameter is formed and the resulting high field strength leads to field evaporation of positive metal ions. Space charge effects stabilize the emission current and increase the virtual source size to about 50 nm. Due to these effects the energy spread is about 5 eV at low current. At present Ga is used because of its high performance, reliability and long lifetime.

Ion optical columns mostly consist of a condenser and objective lens either operating with a collimated beam or with an intermediate crossover. Due to the small virtual source size the overall magnification can be close to 1. The current density for spot sizes of 200 nm and below is determined by the chromatic aberration of the lenses. Typically the source is operated with an emission current of 1-2 μA to keep the energy spread as low as possible.

When a ToF analyzer is used, the primary beam has to be pulsed. The schematic diagram of pulsed primary ion beam is shown in Fig.3.4. The duty time is 10^{-4} sec at the pulsing frequency of 10 kHz. After the pulsing typical beam current is of the order of 0.1 ~ 3 pA. The beam current of 1 pA corresponds to 6.24 x 10^6 ions, or PIDD of 6.24 x 10^{10} ions/cm^2 when it is dosed on the 100 x 100 μm area on the surface. Considering the static limit mentioned above, the acquisition should be finished within 100 sec under these conditions.

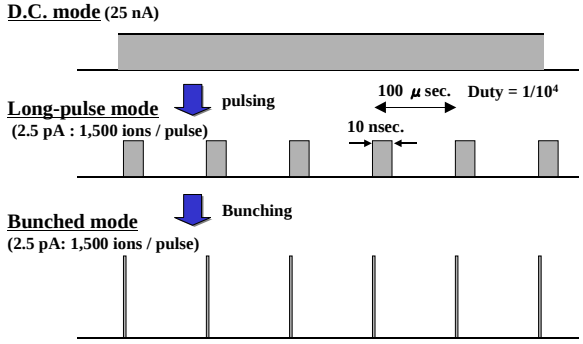

Fig. 3.4. Schematic diagram of pulsed primary ion beam used for ToF-SIMS.

Two operating modes

There are two operating mode of the LMIG for ToF-SIMS measurements: "bunched mode" and "long-pulse mode". The former is adequate to mass spectrum acquisition with high mass resolution and the latter is more suitable for imaging with high lateral resolution. Comparable examples of positive ion image and mass spectrum for two operating modes are shown in Fig.3.5. For the bunched mode, the primary ion pulses are bunched in order to reduce the pulse width at just the arrival on the analyzing surface, which leads to the improvement of mass resolution (shown in the bottom of Fig.3.5). Thus, this mode is utilized for mass spectrum acquisition. But the reduced pulse width will cause the increase of ion density and degrade the spatial resolution (shown in the top of Fig.3.5).

On the contrary, the spatial resolution is getting better with long-pulse mode. This mode is utilized for imaging of chemical species on the surface. Instead of the improvement of spatial resolution, the mass resolution is degraded.

Typical conditions for two modes are tabulated in Table 3.1.

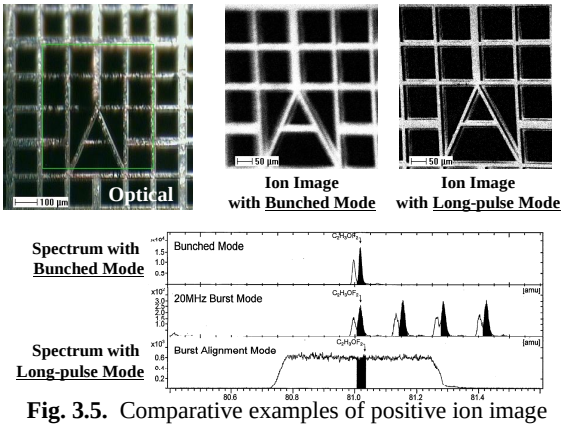

Fig. 3.5. Comparative examples of positive ion image and mass spectrum for two operating modes.

Table 3.1. Typical conditions for two operating modes.

Mode	Bunching	Long-pulse
Current	~ 1 pA	~ 0.2 pA
Pulse width	~ 0.7 nsec	~ 50-100 nsec
Mass resolution	~ 10000	~ 100-500
Lateral resolution	~ 2-3 μm	~ 100 nm

3.3. Time-of-Flight Mass Analyzer

Mass spectrometer [1,5]

For SIMS systems, there are three types of mass spectrometer: the quadrupole, magnetic sector and time-of-flight (ToF) analyzers. In the beginning of Static SIMS (S-SIMS), the quadrupole analyzer was utilized in the majority of S-SIMS systems because of its ability for fast mass scan, a relatively high mass resolution and transmission, a small size and no magnetic stray fields.

In the early 1980's the possibility of utilizing the ToF analyzers began to be explored. The parallel ion detection in these systems overcomes a most serious limitation of the quadrupoles: the 'one mass at a time' principle.

ToF spectrometer [1,9]

ToF analyzer is the best choice for S-SIMS because of its high geometrical transmission as well as of its ability for simultaneous detection of all secondary ions of

one spectral polarity.

Mass determination in a ToF analyzer is based on the measurement of a flight time from a defined start time. It is essential that the ions to be analyzed enter the flight path simultaneously or at least within the shortest possible time interval. To achieve this, the area of the surface to be analyzed is bombarded with pulses of primary ions whose duration Δt_p is kept as short as possible. All the secondary ions that are generated almost simultaneously are then accelerated by passage through a fixed accelerating voltage U before entering the flight path of length L. If we neglect the relatively small initial energy of the secondary ions, it follows that all the ions enter the flight path with the same kinetic energy. The measured time of flight T has the relationship as follows:

$U = ½*m*v^2$, where $v = L/T$

$m = 2UT^2 / L^2$

The schematic diagram of ToF analyzer is shown in Fig.3.6.

The mass resolution $\Delta m/m$ of a linear ToF spectrometer as described here is limited by the primary pulse duration Δt_p, the time resolution Δt_D of the detection system, the initial energy ΔE of the emitted secondary ions, and the total flight time t, is given by

$$\Delta m/m = \Delta E/E + 2(\Delta t_p + \Delta t_D)/t$$

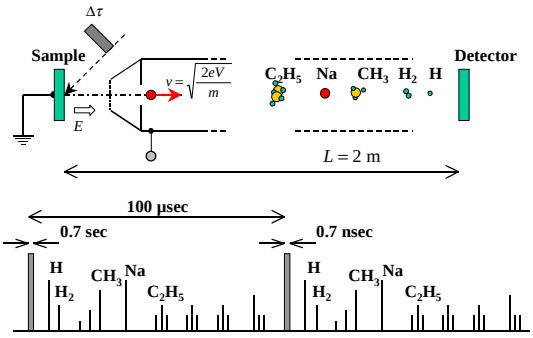

Fig. 3.6. Schematic diagram of ToF mass spectrometer.

3.4. Instrumental Systems Used

In this work, two instruments are used for ToF-SIMS experiments.

PHI, TRIFT II

This system is equipped with Ga LMIG and electrostatic energy analyzer-type ToF mass spectrometer.

The sample holder is biased with a 3 kV positive voltage at the acquisition of positive ions. Thus, the impact energy of primary ions is described as the beam energy minus 3 keV. The beam energy of 12 keV is adequate for mass spectrum acquisition with high mass resolution and the 22 keV beam is suitable for imaging with high lateral resolution. Along with 12 and 22 keV, 2 and 7 keV beams can be used. Nevertheless the lower energy beams will degrade the ToF-SIMS performance such as mass resolution or lateral resolution, wide variety of beam energy enables us the "beam-energy dependent" experiments.

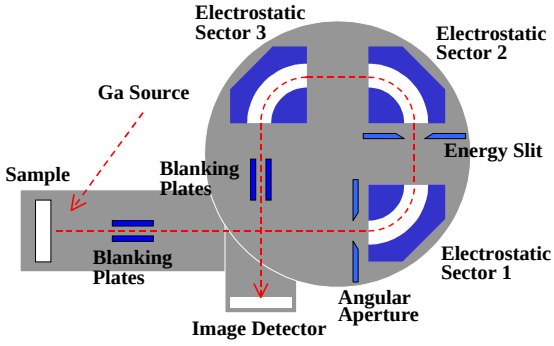

Fig. 3.7. Schematic diagram of PHI, TRIFT II.

ION-TOF, TOF-SIMS IV

This system is equipped with Ga LMIG and reflectron-type ToF mass spectrometer. Typical beam energy is 25 keV for both mass spectrum acquisition and imaging.

Insulating samples can be more easily analyzed than TRIFT II because the sample holder is grounded in this system. For charge compensation of charging effects on the insulators, the flood gun providing the low energy electron beam is used. The extraction field for detection of secondary ions goes down to zero volts between the primary ion pulses. At this point a pulse of electrons is directed at the sample surface and neutralizes the positive surface charge.

Along with Ga LMIG, Ar ion gun for sputtering is also equipped in this system, which enables us the “dual ion beam depth profiling”. The data collection cycles are composed of ToF-SIMS analysis by Ga^+ and sputtering by Ar^+.

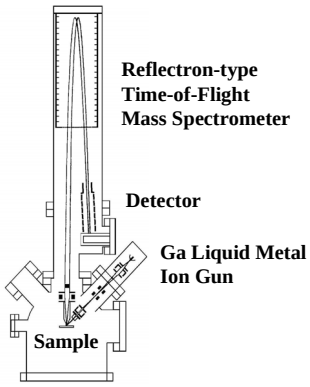

Fig. 3.8. Schematic diagram of ION-TOF, TOF-SIMS IV.

References

[1] A. Benninghoven, Surf. Sci., 35, 427 (1973).
[2] A. Benninghoven, Surf. Sci., 299/300, 246 (1994).
[3] A. Benninghoven, Angew. Chem. Int. Ed. Engl., 33, 1023 (1994).
[4] Eds. D. Briggs and M. P. Seah, Practical Surface Analysis, 2nd ed., Vol. 2, Wiley, Chichester (1992); 志水隆一, 二瓶好正 監訳, 表面分析 : SIMS -二次イオン質量分析法の基礎と応用-, アグネ承風社 (2003).
[5] D. Briggs, A. Brown and J. C. Vickerman, Handbook of Statistic Secondary Ion Mass Spectrometry, Wiley, Chichester (1989).
[6] M. Prutton, Introduction to Surface Physics, Oxford University Press, Oxford (1994).
[7] 大西孝治, 堀池靖浩, 吉原一紘 編, 固体表面分析 I, 講談社 (1995).
[8] 日本表面科学会 編, 表面分析技術選書 二次イオン質量分析法, 丸善 (1999).
[9] B. Hagenhoff, Mikrochimica Acta, 132, 259 (2000).
[10] P. Sigmund, Phys. Rev., 184, 383 (1969).
[11] D. Briggs and M. J. Hearn, Vacuum, 36, 1005 (1986).
[12] F. Kotter and A. Benninghoven, Appl. Surf. Sci., 133, 47 (1998).
[13] D. Stapel, O. Brox and A. Benninghoven, Appl. Surf. Sci., 140, 156 (1999).
[14] D. Rading, R. Kersting and A. Benninghoven, J. Vac. Sci. Technol. A 18, 312 (2000).
[15] E. Niehuis, Proc. SIMS X, 47 (1997).
[16] J. Orloff, Rev. Sci. Instrum., 64, 1105 (1993).
[17] B. Hagenhoff, J. Lub, N. T. van Velzen, D. van Leyen and A. Benninghoven, Surf. Interface Anal., 12, 53 (1988).

Chapter 4

Initial Oxidation Study of Metal Surfaces by AES and ToF-SIMS

In this chapter 4, I will demonstrate the results of studies which aim at extraction of chemical information by the complementary use of conventional AES, high-energy resolution AES (HR-AES) and ToF-SIMS. As a typical example of chemical state changes, the initial oxidation on the metal surface caused by the oxygen exposure is focused on. First, a conventional AES system, which provides the AES spectra in derivative mode with usual energy resolution, is used. Secondly, a modern HR-AES system, which provides the AES spectra in direct mode (without any derivation) with high-energy resolution, is used. Lastly, a newcomer of ToF-SIMS is applied to the field of the initial oxidation study of metals instead of the already established electron spectroscopic techniques.

4.1. Initial Oxidation Study of 3d Transition Metals (Cr, Fe, Co and Ni) and Rare Earth (Tb) by Conventional AES: Application to Auger Depth Profiling of Magneto-Optical Disk

Abstract

Initial oxidation processes of 3d transition metals (Cr, Fe, Co and Ni) and rare earth (Tb) were studied by Auger peak-to-peak height (APPH) method. Based on the results obtained, a simple technique using APPH's ratio was applied to the Auger depth profile analysis of magneto-optical disk (MOD). It was clearly revealed that the preferential oxidation of Tb occurred only at the lower interface between the TbFeCo and metal-oxide layers. It was found that this technique is applicable for obtaining the chemical information about the interface oxidation.

4.1.1. Introduction

Auger electron spectroscopy (AES) combined with inert gas-ion sputtering is of considerable importance in applied surface analysis of thin films. But it has been difficult to obtain information about chemical states especially at the interface of multilayers with AES. Recently many studies [1-6] have been performed to obtain the chemical information from AES through analyzing the factors which determine an Auger spectral line shape, namely factor analysis [7]. In order to perform this method, however, an additional computerized data processing system is necessary. In this chapter, the conventional and simple technique of Auger peak-to-peak height (APPH) method for Auger depth profile analysis is proposed.

The chemisorption of oxygen and the initial stages of oxidation on a clean metal surface have been of great interest, because of their technological importance. Many authors have discussed the oxide growth mechanism both theoretically and experimentally. In some of them AES and factor analysis were applied to study quantitatively the initial oxidation stages of Cr [6], Fe [4], Ni [1,2], steel [5] and their alloys [2,3].

In this section 4.1, the main purpose is to show how chemical information about the interface oxidation can be obtained from the Auger depth profile by application of the simple APPH method. The oxygen exposure experiments were performed on 3d transition metals (TM) and rare earth (RE), which have been the most important species for memory media. The changes of Auger line shapes of LMM and NOO transition groups for TM and RE, respectively, were investigated. In terms of the APPH method, the changes of the APPH's ratio upon increasing oxygen exposure were focused on.

Based on the results obtained, a simple technique was applied to the Auger depth profile analysis of magneto-optical disk (MOD), and tried to make clear the oxidation behavior at its interfaces. The interfacial oxidation significantly degrades the recording function of MOD. Thus, it is important to evaluate the oxidation behavior in order to invent the adequate layer structure against the oxidation.

4.1.2. Experimental

Materials

High purity polycrystalline Cr, Fe, Co and Ni sheets were mechanically polished and washed with acetone. For Tb, a thin film deposited on a glass substrate was prepared. Along with a Tb film, a model sample of MOD deposited on a glass substrate was prepared for AES depth profiling. The detail of MOD sample will be described in the following section 4.1.3 (see Fig.4.7).

Measurements

The experiments were performed in a AES system of JEOL model JAMP-30. The base pressure was less than 1 x 10^{-7} Pa in the analyzing chamber. For AES, electron beam of 5 keV, at a current of 0.2 μA with a diameter of 10 μm was used. Auger spectra were obtained in a derivative mode [d(N*E)/dE], using lock-in amplifier operating with a 5 Vp-p modulation. A single-pass CMA, of which the axis was perpendicular to the primary electron gun, was used as an analyzer. The energy resolution of CMA was ΔE/E = 0.6%. The sample was oriented with 75 degree between the surface normal and the primary electron gun.

Oxygen Exposing

In the first experiments, after initial cleaning by ion sputtering, the pure metals were exposed to oxygen at room temperature up to 100 L (1L=10^{-6} Torr*sec). Oxygen was admitted at 0.1-1 x 10^{-7} Torr into the chamber through a variable leak valve.

AES Depthprofiling of MOD

In the second experiments, depth profiling of MOD was performed with a rastered Ar ion beam of 3 keV. The ion current was 0.5 μA and the rastered area was 1 x 2 mm^2.

4.1.3. Results and Discussion

Initial oxidation study of 3d TM (Cr, Fe, Co, Ni)

Figs.4.1(a)-(d) show the changes in the derivative AES spectra of Cr LMM, Fe LMM, Co LMM and Ni LMM with increasing oxygen exposure. In the Auger spectra of 3d TM, three specific peaks arising from the transitions $L_3M_{23}M_{23}$ (=LMM), $L_3M_{23}M_{45}$ (=LMV) and $L_3M_{45}M_{45}$ (=LVV), namely LMM group, appear. After oxygen exposure, an additional peak of O KLL appears around 500 eV (Fig.4.1(a)). The relative APPH of the three peaks changed upon oxygen exposures (Fig.4.2), as previously reported [8]. It was clearly observed that the proportion of LVV, which was concerned with the valence band, was in particular reduced among them. Figs.4.3(a) and (b) show the changes of APPH of O KLL and APPH's ratio of LMV/LVV as a function of oxygen exposure. The APPH's ratio increased corresponding to the increase of O KLL APPH. Since the Auger transition of LVV is the most sensitive to the change of the valence band structure among the LMM group, the increase of the ratio is accounted for the broadening of LVV peak due to the oxygen chemisorption followed by the oxide growth.

According to the previous studies applying factor analysis [1,2,4,6], at least three factors are distinguished on the surface exposed to oxygen up to ~100 L. The change in the ratio of LMV/LVV is supposed to correspond with the different initial oxidation stages. In conclusion, the APPH ratio between LMV and LVV depends on the oxidation stages of the surface and this ratio can be used as an index of oxidation.

Initial oxidation study of RE (Tb)

In the case of Tb, in addition to the change of the relative APPH between two main peaks in NOO group, a new feature appeared around 134 eV in an oxygen-adsorbed Tb spectrum (Fig.4.4). This new feature has been previously reported [9,10], but has not been well characterized. The feature will be called "Tb oxide" in this section. Fig.4.5 shows the changes of APPH of O KLL and APPH's ratio of Tb oxide/Tb NVV, where Tb NVV denoted the lower peak of two main peaks around 116 eV in a metallic Tb spectrum (see the top of Fig.4.4). The change in the ratio was quite similar to the increasing curve of O KLL APPH. After the oxygen exposure of ~20 L the changes of both the ratio and O KLL almost reached to the saturation.

The APPH's ratio will be used as a quantitative index of oxidation states on Tb surface. Fig.4.5 shows that the 100L-exposed

surface is the oxygen-saturated surface, where the oxygen coverage is estimated to be ~1. In this way a relationship between the coverage θ and the APPH's ratio of Tb oxide/Tb NVV , R, is expressed as follows:

$$\theta = 1.017 * R + 0.036,$$

as is plotted in Fig.4.6.

Application to Auger depth profiling of MOD

The MOD sample used here has four layers deposited on the glass substrate. They are called protective, reflective, memory and interferential layers, as shown in Fig.4.7. The thickness and the chemical composition of each layer are also shown in Fig.4.7. The memory layer is composed of $Tb_{20}Fe_{72}Co_8$, which is one of the RE-TM alloys. The reflective layer is an Al-alloy and both the protective and the interferential layers are metal oxides, whose composition is nearly Ta_2O_5.

The results of the depth profiling measurements of magneto-optical disk (MOD) are shown in Figs.4.8 and 4.9. In these measurements, the ratio of Tb oxide/Tb NVV was used for Tb as the index of the oxidation. For Fe and Co, due to the severe overlapping of peaks between them, Fe LMV and Co LMM or Fe LVV and Co LMV, I could not succeed in strict applying the index mentioned above. Fig.4.9 shows the ratios in the cases of (a) Tb and (b) Fe in the depth profile of Fig.4.8. The APPH's ratio between Fe LMM and Co LVV, which are less affected by the peak overlapping, is also shown in Fig.4.9(b).

It was clearly observed that Tb was oxidized only at the interface between the memory and interferential layers. This is reasonable, since at this interface the TbFeCo layer adjoined to the oxygen-containing layer and Tb has a high affinity for oxygen. From the relationship between the coverage and the ratio, the degree of oxide formation at the lower interface was estimated ~0.7 for Tb.

On the other hand, there seemed to be less indication of oxidation about Fe, since the LMV/LVV ratio was increasing very slightly through the layer except the interfaces. Considering the peak overlapping with Co, the changes of the ratios at the both interfaces were accounted for the enrichment of Co, which makes difficult the application of the index. However, these results clearly indicated that the preferential oxidation of Tb occurred at the lower interface and the index applied here can be used in order to obtain the chemical information in Auger depth profiling.

4.1.4. Conclusions

The changes of the APPH's ratio were oserved as a function of oxygen exposure on 3d TM and RE using the simple APPH method. The analysis of the ratio was applied to the depth profiling of MOD as an index of interface oxidation. The results obtained here suggested that this technique could be useful for the analysis of interface oxidation using the conventional Auger depth profile analysis.

References

[1] J. Steffen and S. Hofmann, Surf. Sci. 202, L607 (1988).
[2] S. Hofmann and J. Steffen, Surf. Interface Anal. 14, 59 (1989).
[3] H. J. Steffen and S. Hofmann, Surf. Interface Anal. 19, 157 (1992).
[4] C. Jansson and P. Morgen, Surf. Sci. 233, 84 (1990).
[5] C. Jansson, G. T. Nielsen, J. Jakobsen and P. Morgen, J. Vac. Sci. Technol. A 11, 183 (1993).
[6] C. Palacio and H. J. Mathieu, Surf. Interface Anal. 16, 178 (1990).
[7] E. R. Malinowski, p. 4, in Factor Analysis in Chemistry, 2nd ed., Wiley, New York, 1991.
[8] K. Ishiguro and T. Homma, J. Japan Inst. Metals 45, 360 (1981).
[9] K. F. Stork, N. R. Armstrong and P. A. Lee, J. Vac. Sci. Technol. A 6, 1863 (1988).
[10] G. L. P. Bernig, H. C. Swart and B. de Witt, Appl. Surf. Sci. 64, 1 (1993).

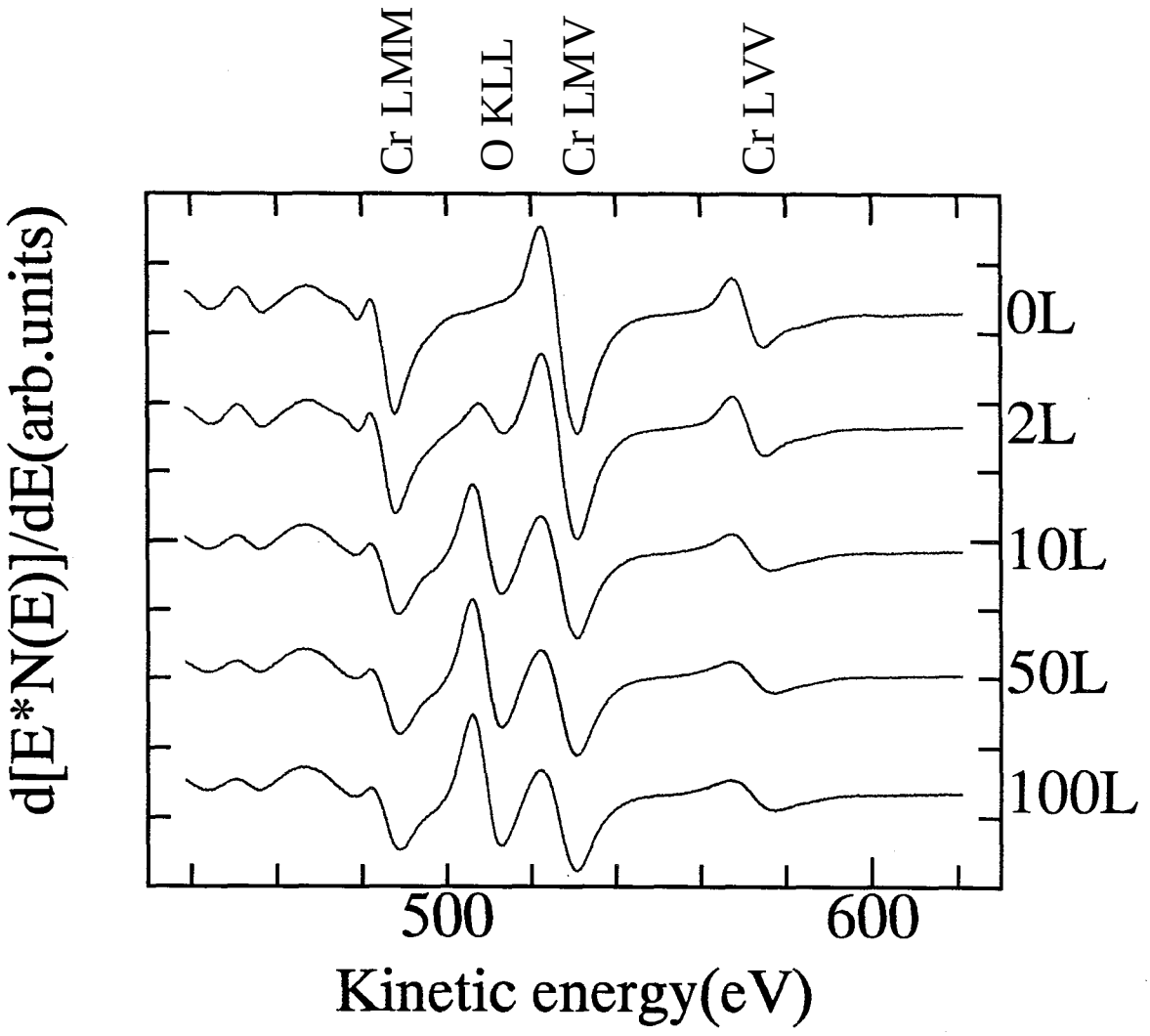

Fig. 4.1.(a) Derivative Cr LMM Auger spectra as a function of kinetic energy for different oxygen exposures.

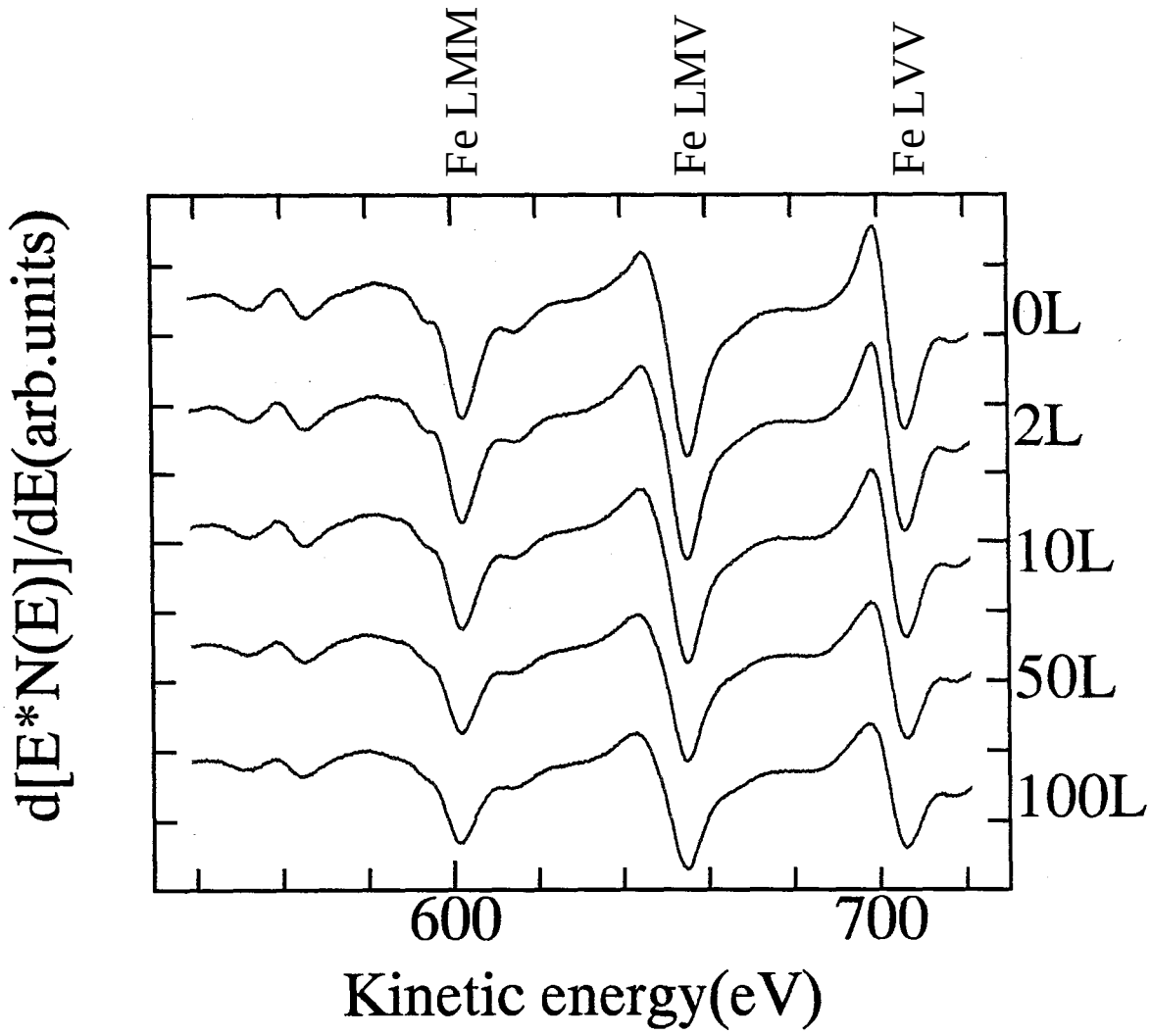

Fig. 4.1.(b) Derivative Fe LMM Auger spectra as a function of kinetic energy for different oxygen exposures.

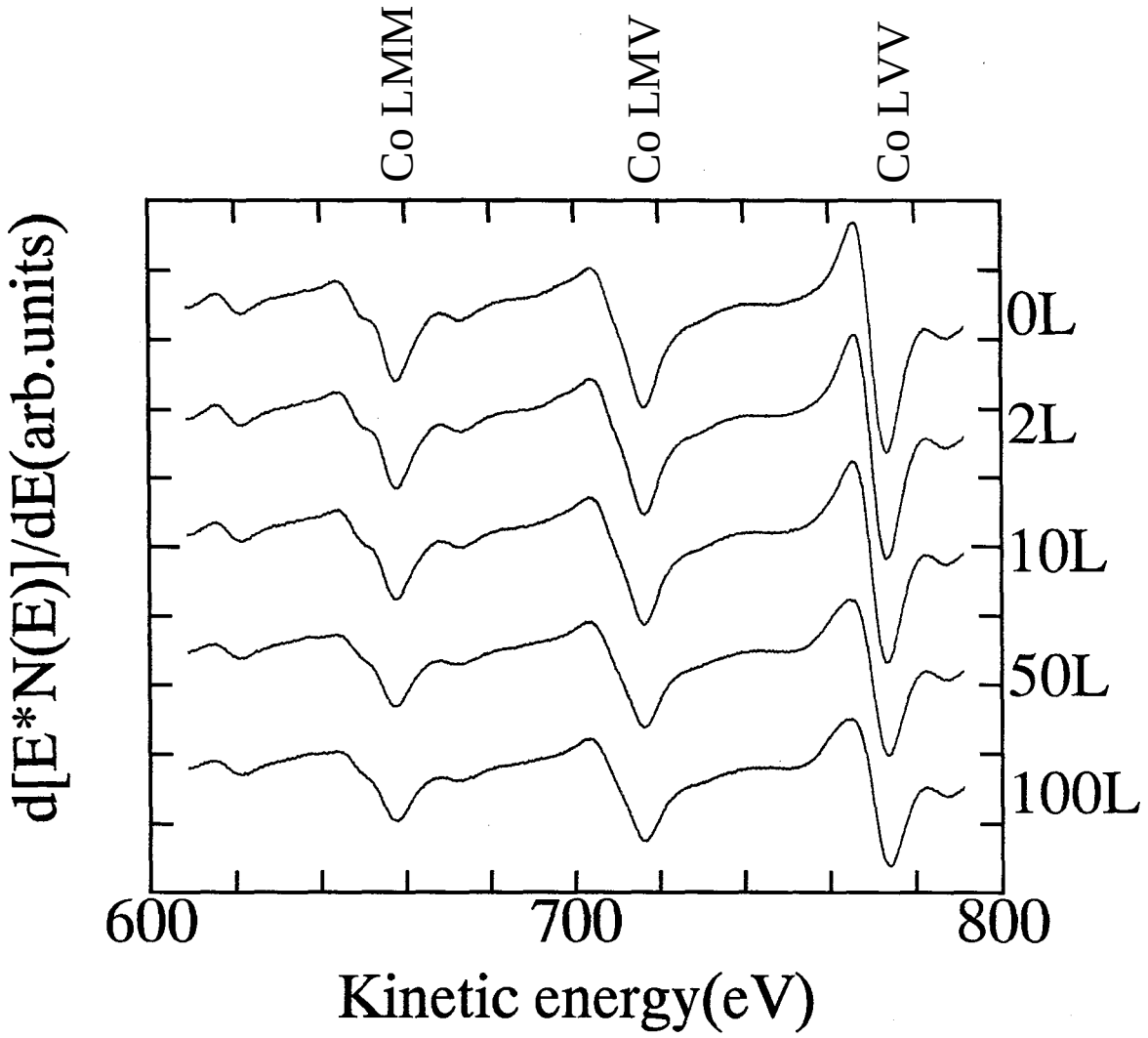

Fig. 4.1.(c) Derivative Co LMM Auger spectra as a function of kinetic energy for different oxygen exposures.

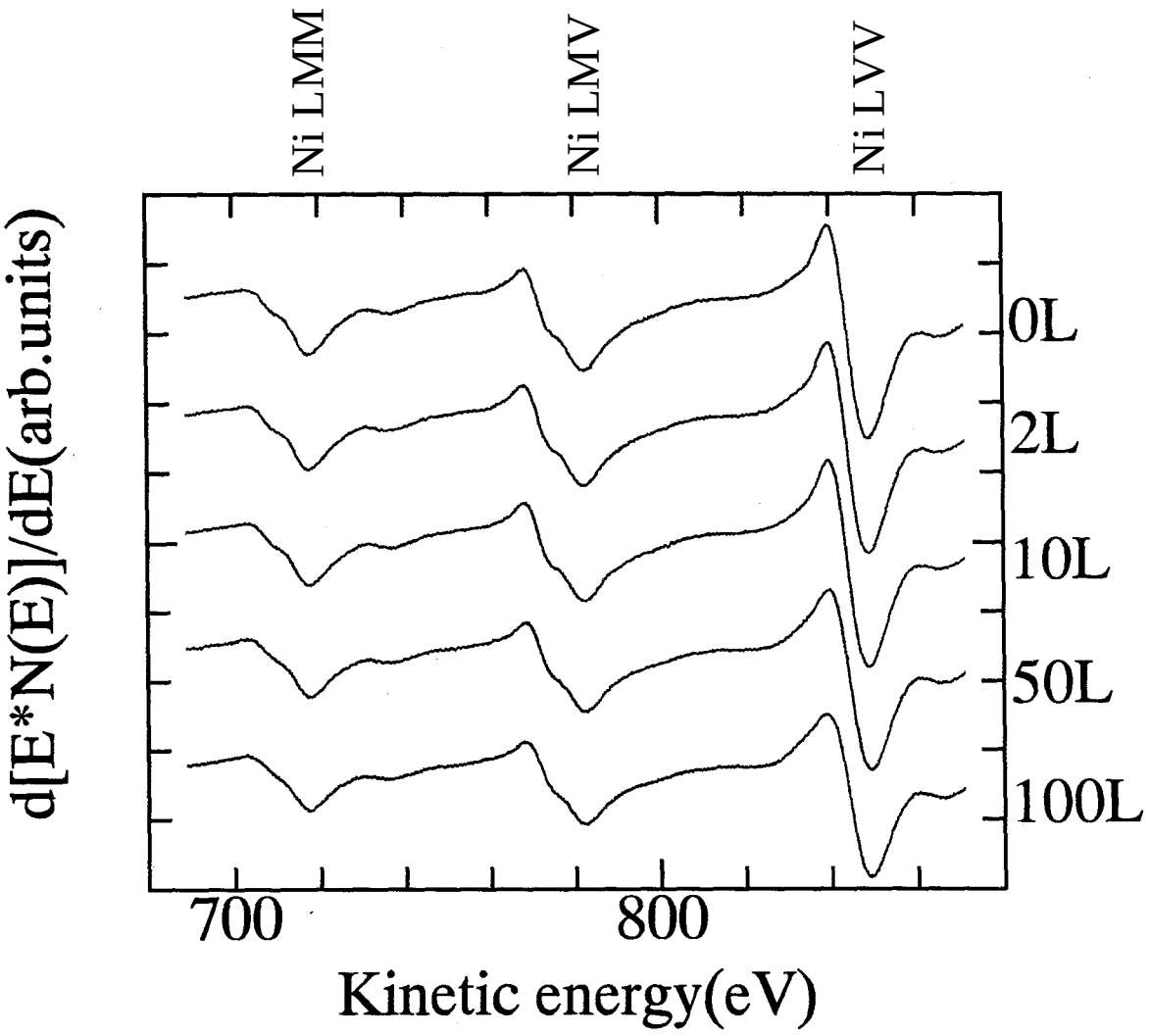

Fig. 4.1.(d) Derivative Ni LMM Auger spectra as a function of kinetic energy for different oxygen exposures.

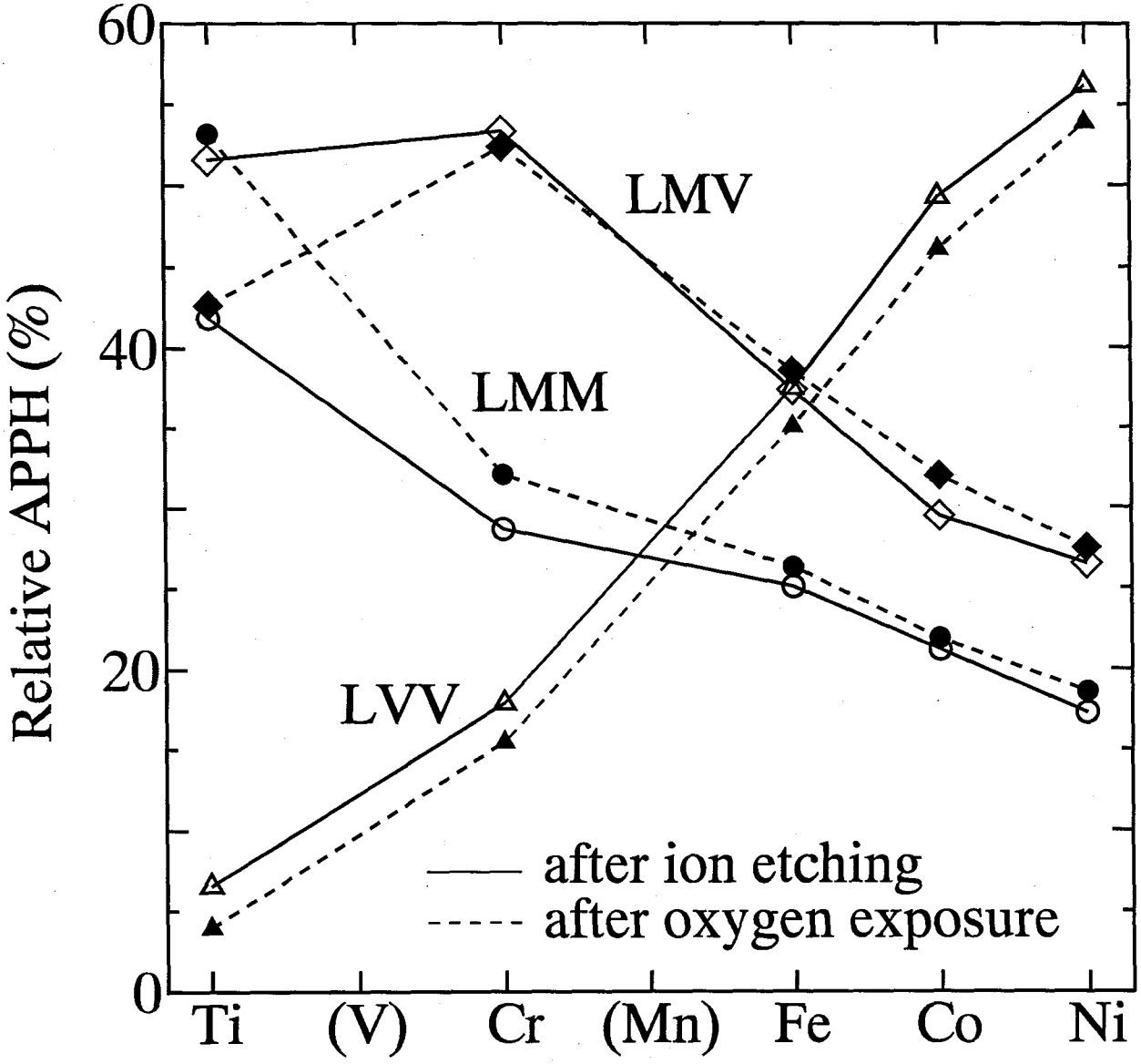

Fig. 4.2.

Change in the relative APPH among the LMM groups of 3d transition–metals upon oxygen exposure(100L).

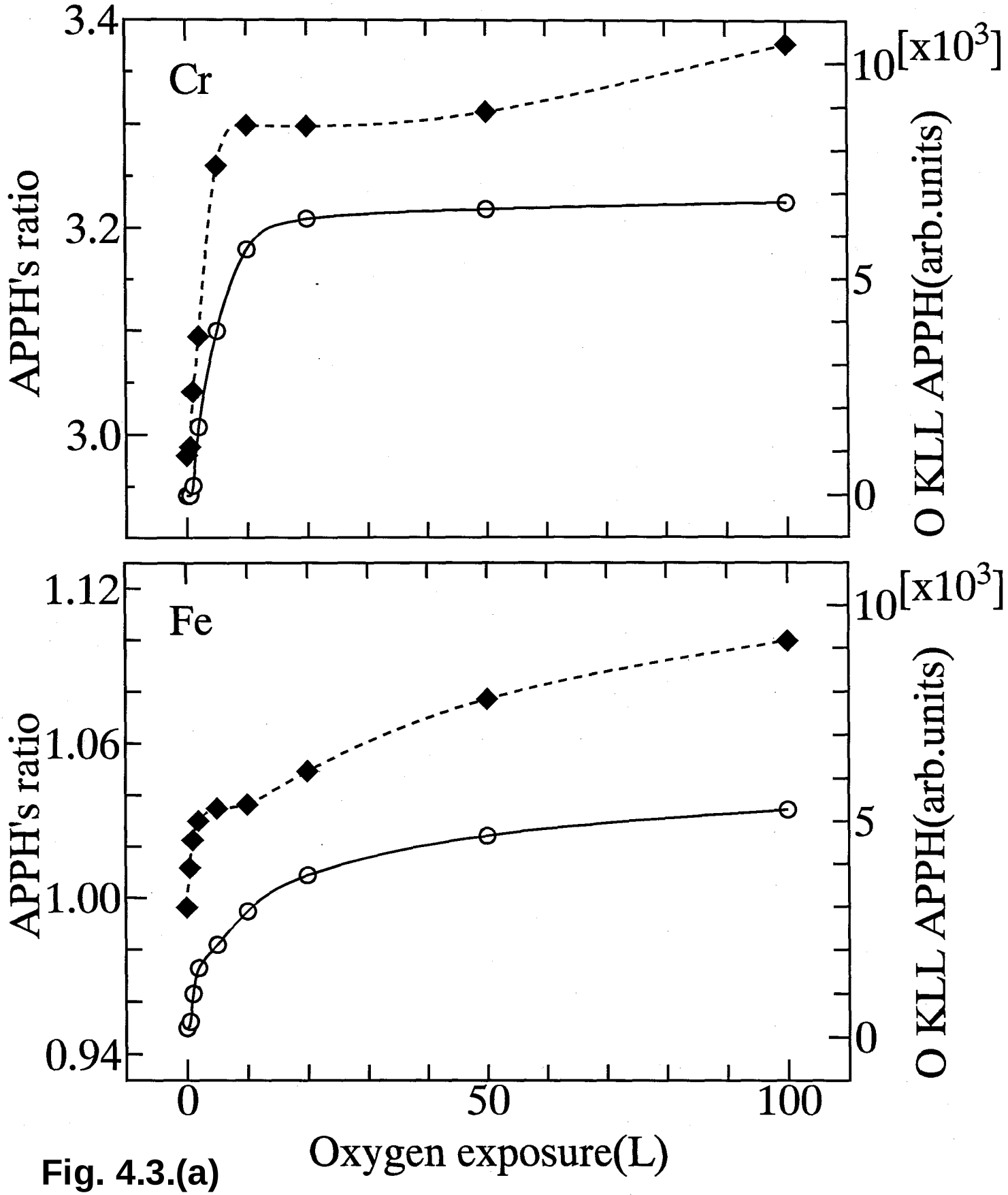

Fig. 4.3.(a)

APPH of O KLL (open circles) and APPH's ratio of LMV/LVV (full squares) as a function of oxygen exposures for Cr and Fe.

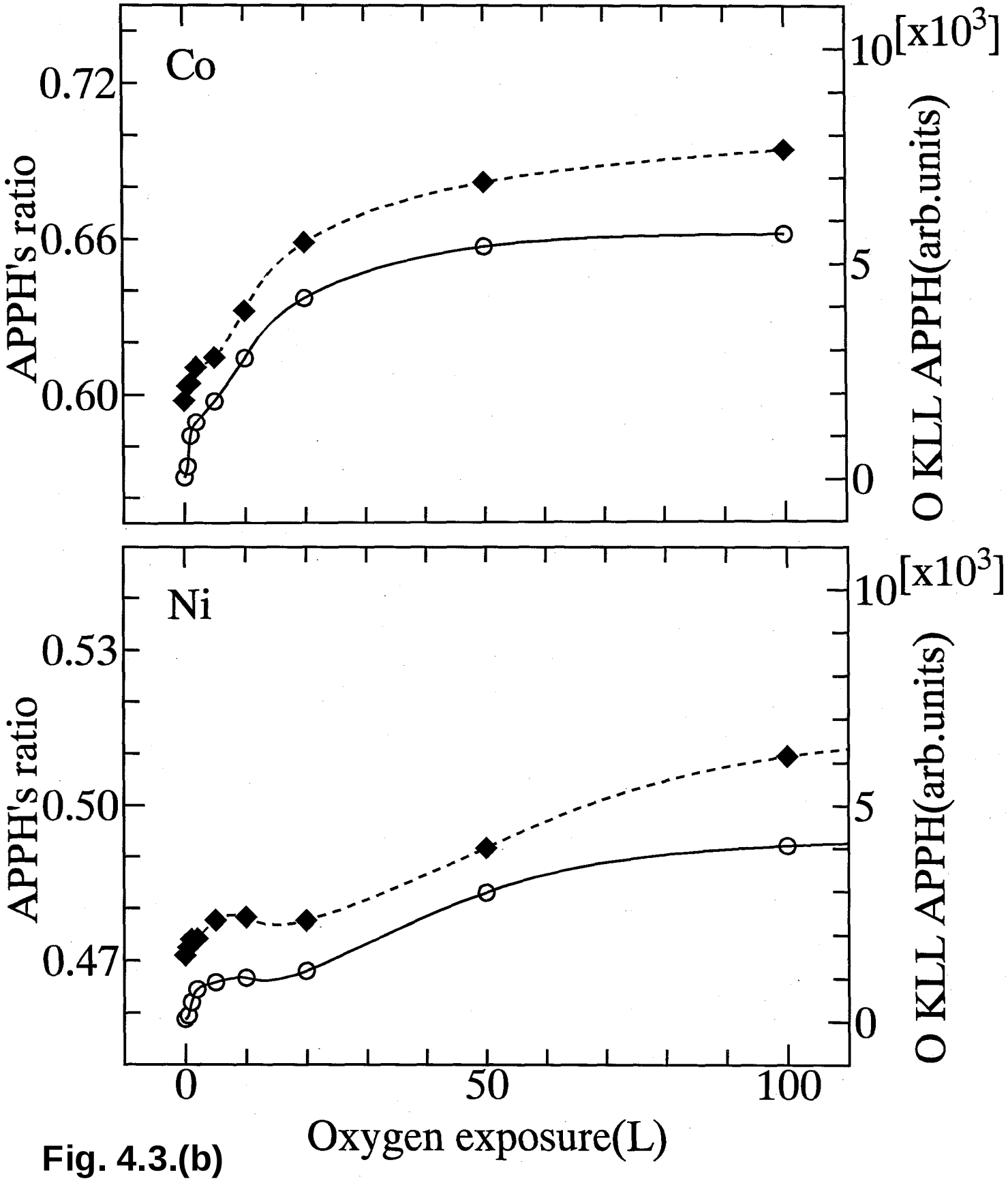

Fig. 4.3.(b)

APPH of O KLL (open circles) and APPH's ratio of LMV/LVV (full squares) as a function of oxygen exposures for Co and Ni.

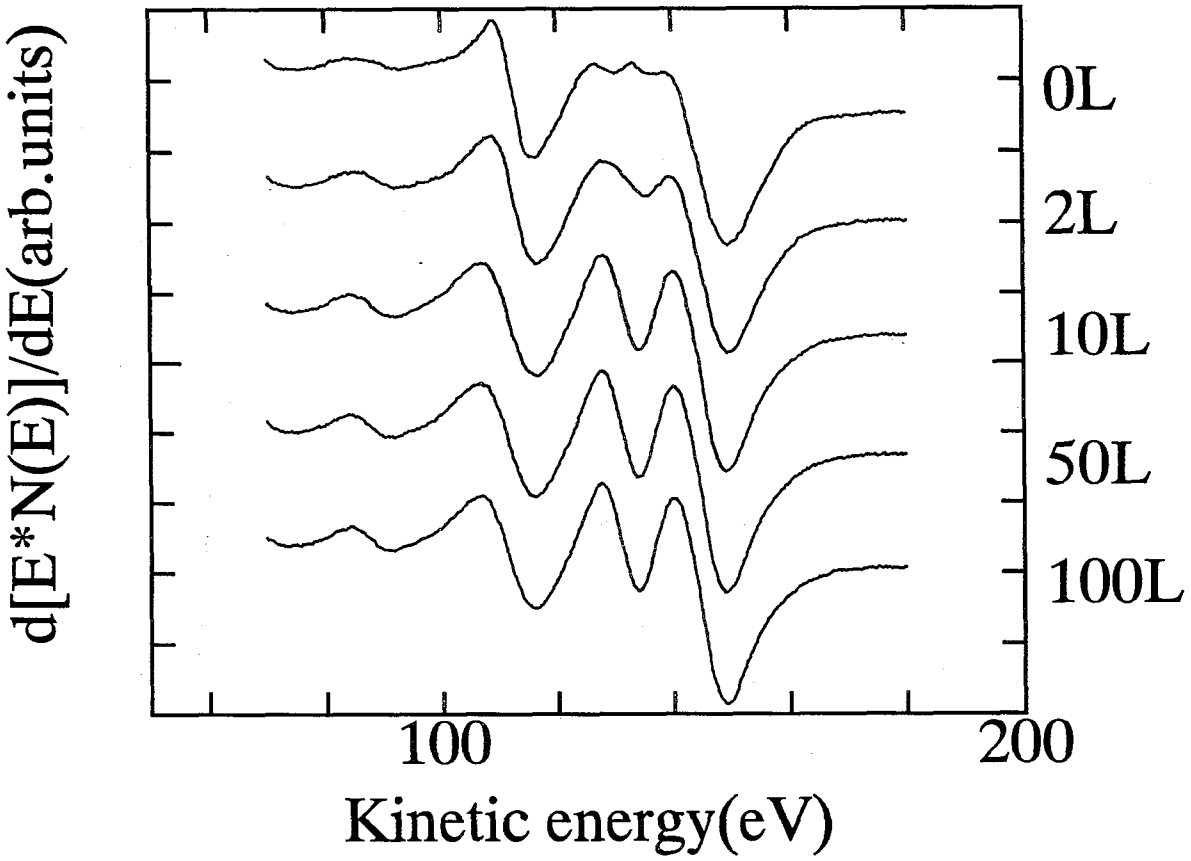

Fig. 4.4. Derivative Tb NOO Auger spectra as a function of kinetic energy for different oxygen exposures.

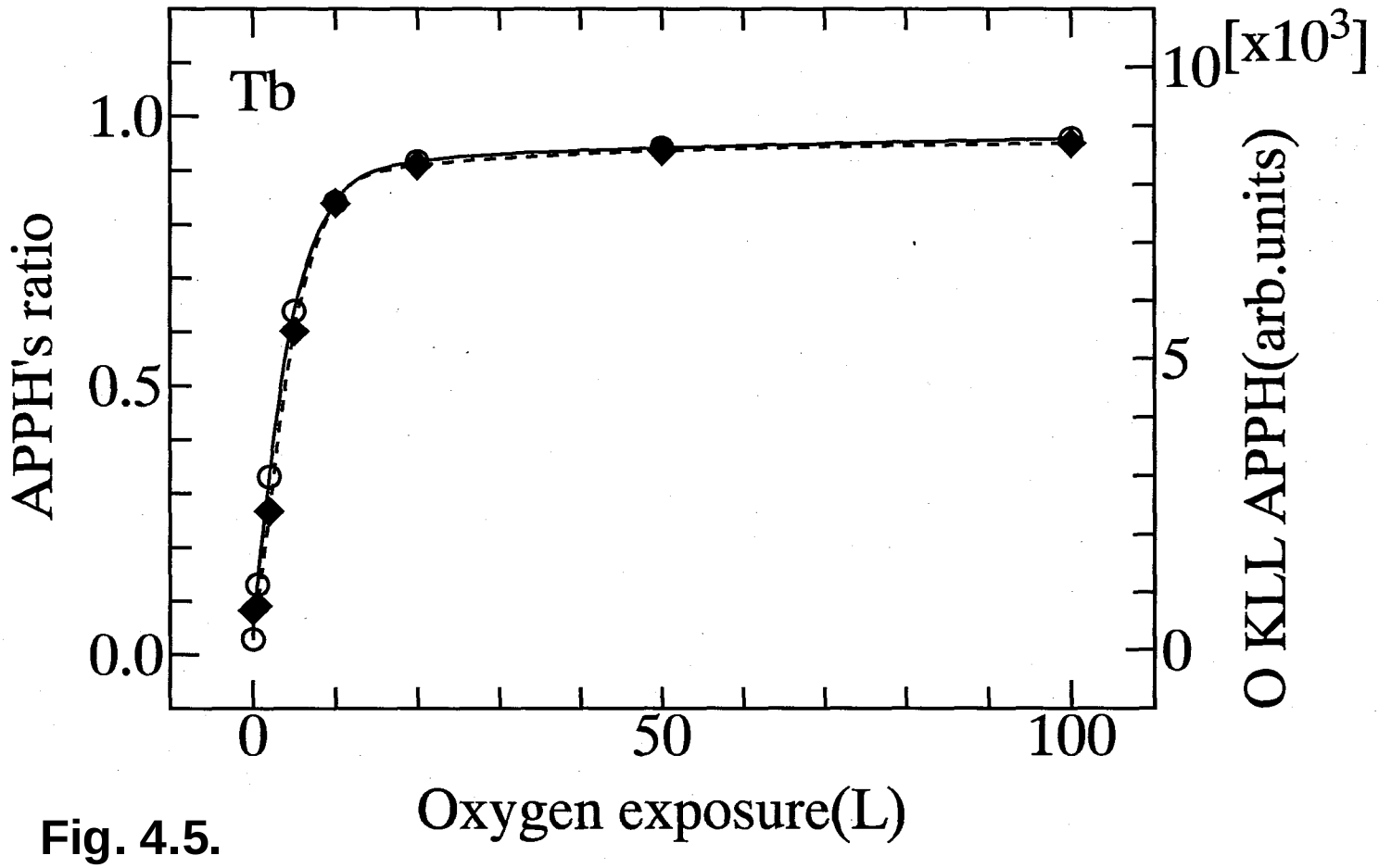

Fig. 4.5.

APPH of O KLL (open circles) and APPH's ratio of Tb oxide/Tb NVV (full squares) as a function of oxygen exposures.

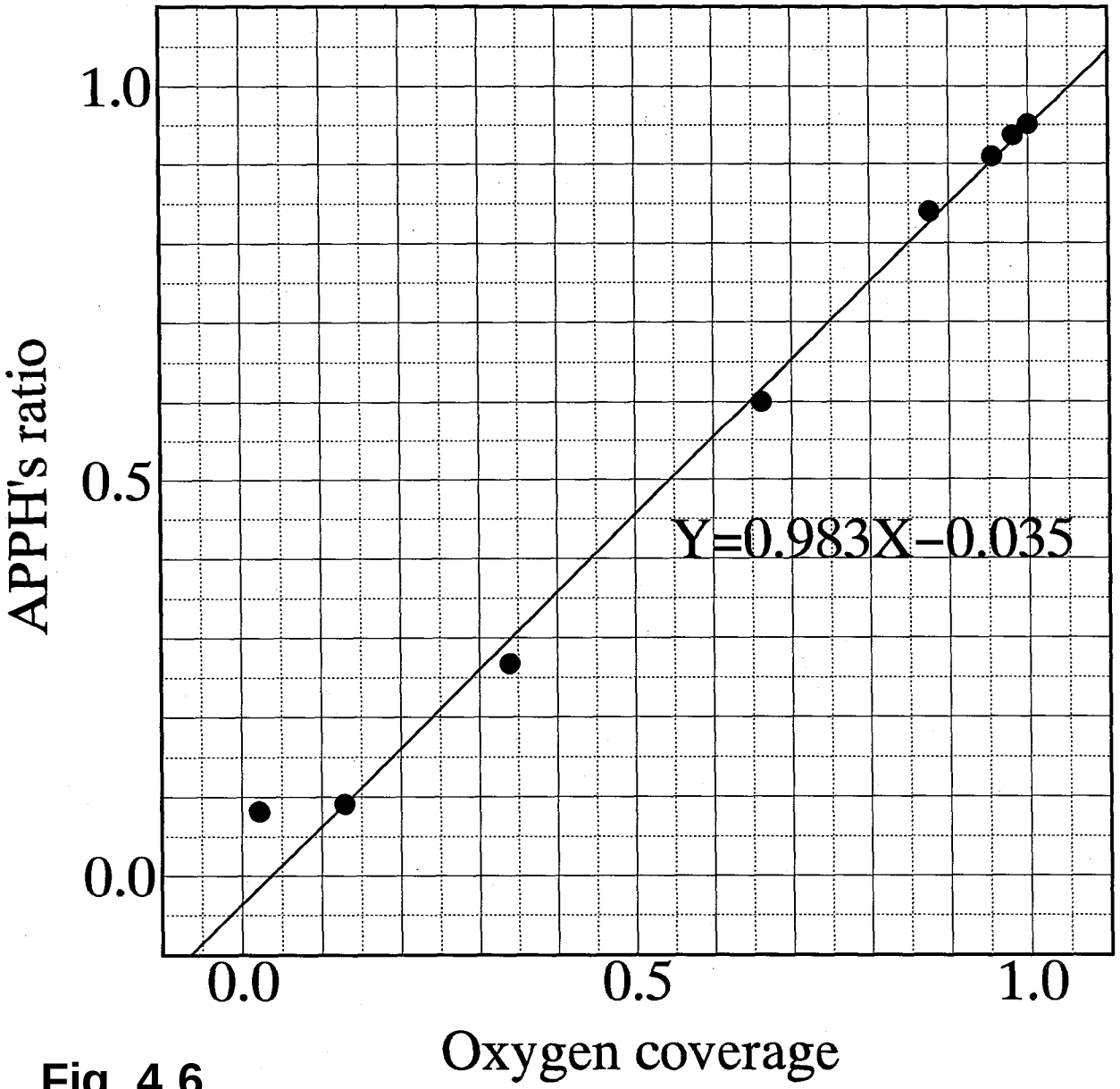

Fig. 4.6.

Relationship between APPH's ratio of Tb oxide/Tb NVV and oxygen coverage.

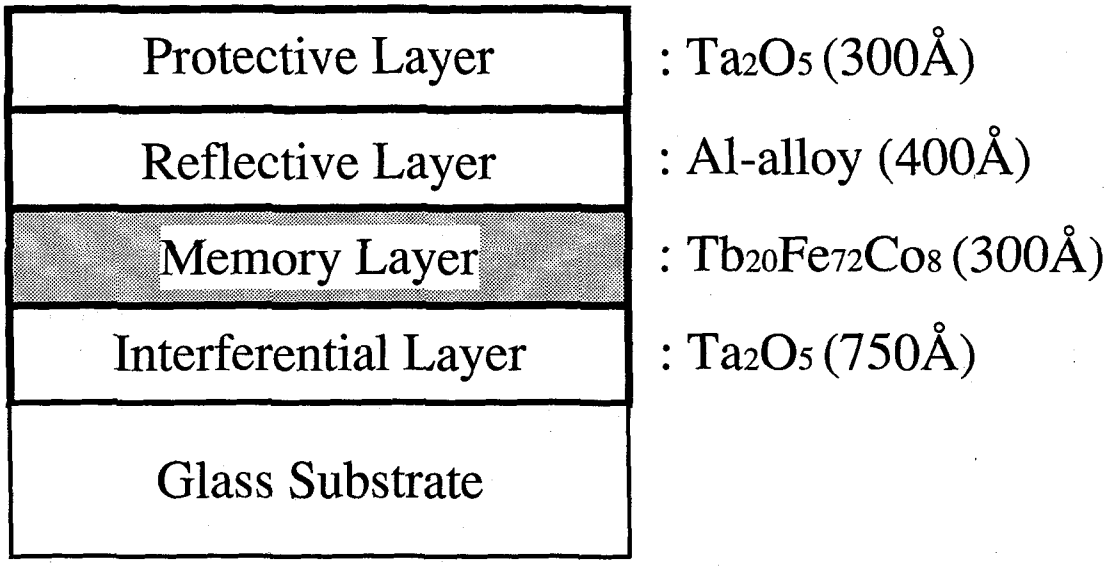

Fig. 4.7. Schematic cross-section of magneto-optical disk (MOD).

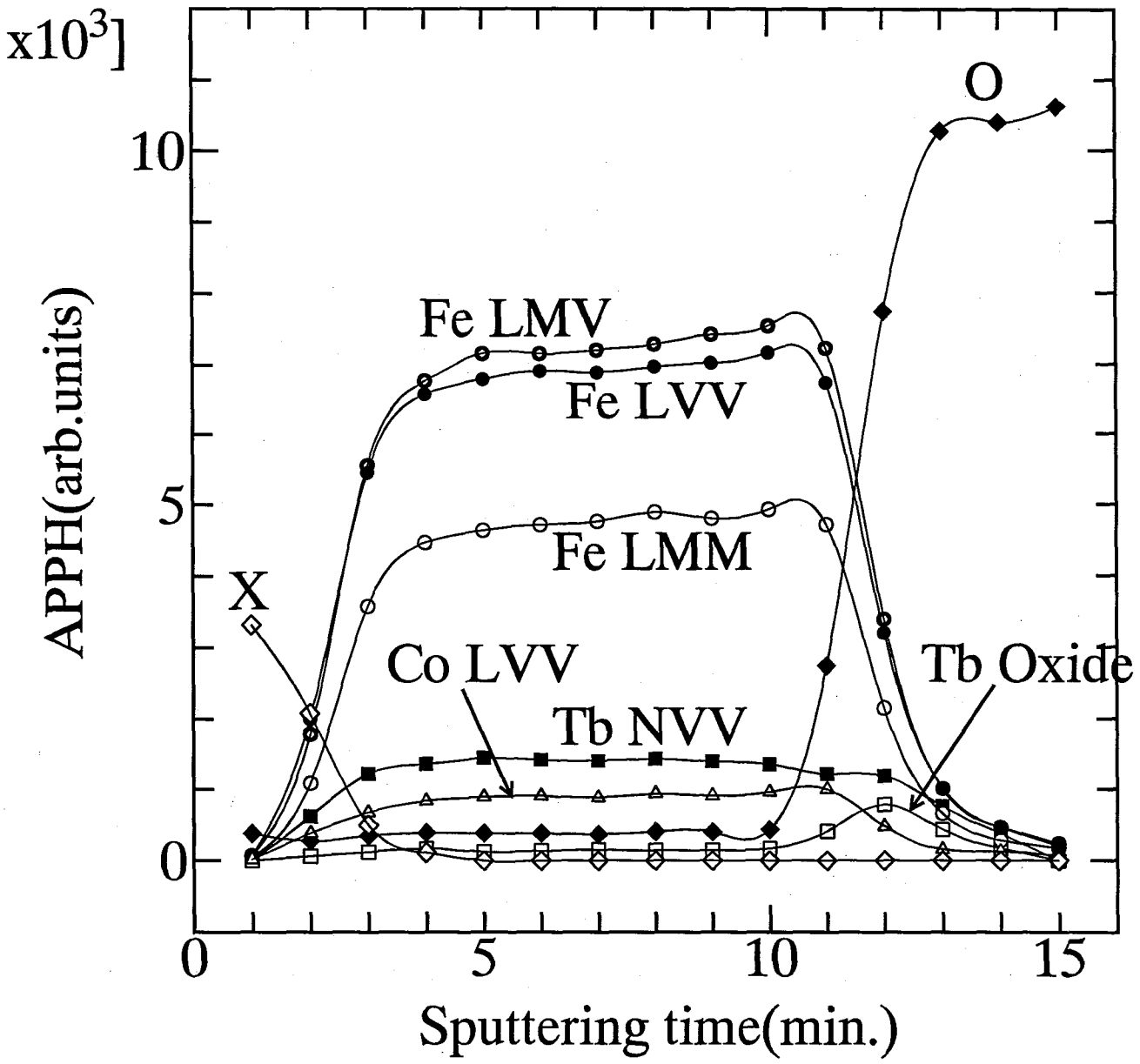

Fig. 4.8. Auger depth profile of MOD.

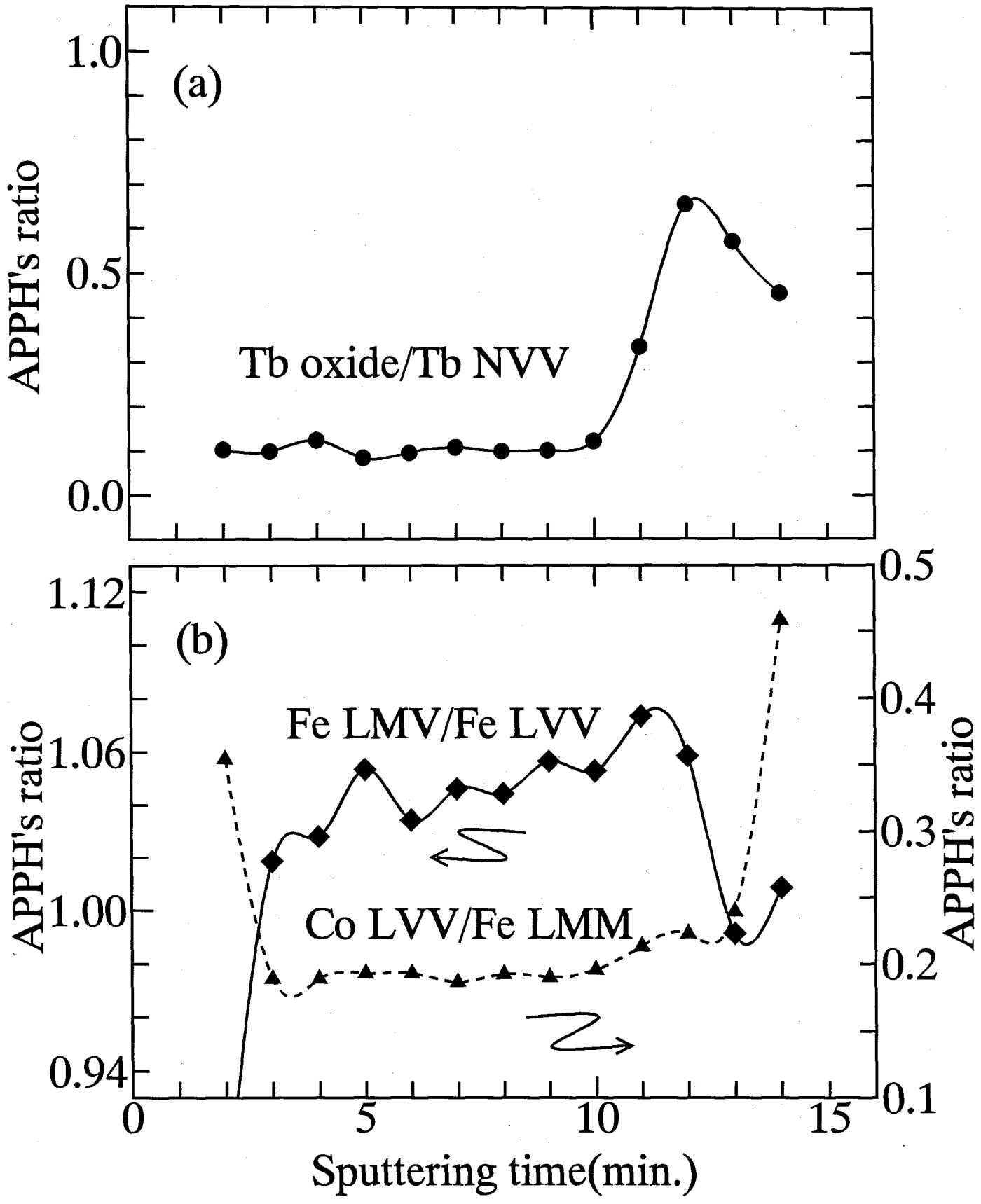

Fig. 4.9. APPH's ratios in Auger depth profile of MOD.
(a)Tb oxide/Tb NVV, (b)Fe LMV/Fe LVV and Co LVV/Fe LMM.

4.2. Initial Oxidation Study of Gd Surface by HR-AES

Abstract

The changes of Auger line shapes in Gd NVV and O KLL as a function of oxygen exposure on Gd was investigated with AES. An additional peak originating from Gd oxide was observed among the NVV line, and the intensity ratio was proposed to be useful as an index of oxidation.

4.2.1. Introduction

A thin layer of alloys between 3d transition metals (TM) and rare earth (RE) have attracted attention in industry for magneto-optical memory media [1]. In the previous section 4.1, a quantitative index of surface oxidation are successfully extracted from the changes in APPH ratio and applied to the interfacial oxidation analysis of a magneto-optical disk.

In this section 4.2, the changes of Auger line shapes in Gd NVV upon oxidation are investigated. Gd NVV spectra are measured in a E*N(E) mode (without differentiation) by the use of the computerized AES detection system, which enables us to measure the direct AES spectra without derivation.

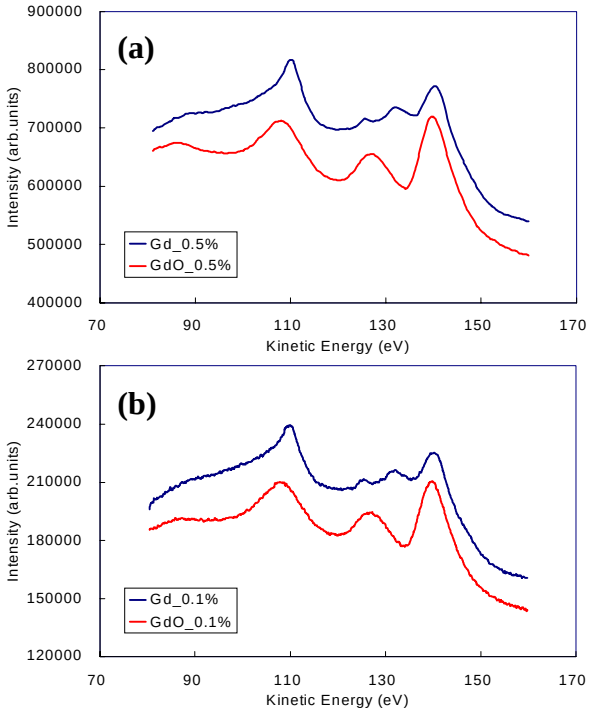

Fig. 4.10. AES narrow-scan spectra of Gd-NOO with energy resolution of (a) 0.5% and (b) 0.1%.

4.2.2. Experimental

Materials

A pure Gd thin film of 185 nm thick was deposited on a Si wafer. To prevent the surface oxidation under atmosphere, a SiN protective layer of 40 nm thick was deposited on the Gd layer. In the AES apparatus, in-situ removal of SiN overlayer was performed by Ar-ion sputtering.

Measurements

The experiments were performed in a FE-AES system of VG Microlab 310-F. The base pressure was less than 1.3 x 10^{-7} Pa. The sputter ion pump of 0.12 m^3/s and titanium sublimation pump were used for pumping the analyzing chamber.

Field emission gun operating at energy of 10 keV, current of 9 nA was used for AES. Auger electrons were acquired with CHA from the raster area of 10 x 10 μm^2 with detection angle of 30 degree from the surface normal. The energy resolution was set to $\Delta E/E$ = 0.5% or 0.1%. Since the line shapes in Gd NVV measured at the energy resolutions of 0.5% and 0.1% are nearly identical (shown in Fig.4.10), the energy resolution was set to 0.5% for Gd NVV measurements. In order to observe the peak energy shift of O KLL, the energy resolution was set to 0.1% for O KLL measurements. Under those conditions it took 15 min to acquire AES spectra of Gd NVV and O KLL. The energy scale of AES spectra was

calibrated by the Seah's reference value for Au, Ag and Cu [3,4].

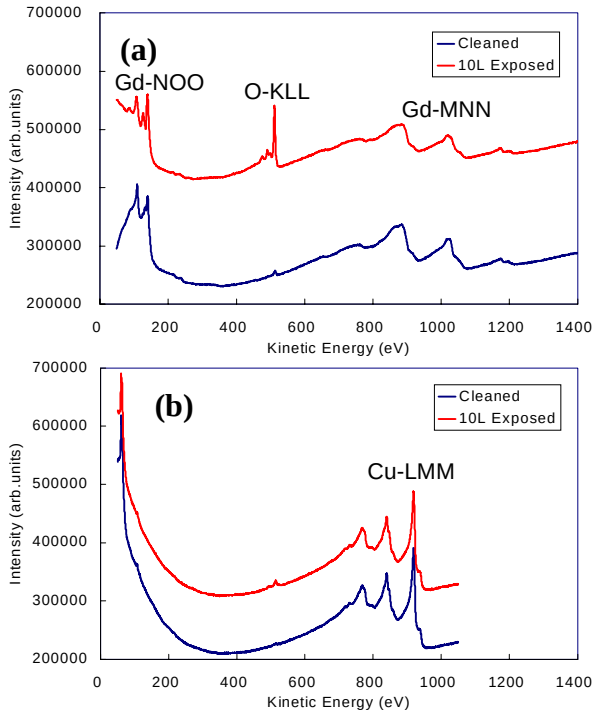

Fig. 4.11. AES wide-scan spectra from (a) Gd and (b) Cu before/after oxygen exposure of 10L.

Ar ion gun operating at energy of 2 keV, current of 200 nA, incidence angle of 48 degree, raster area of 2 x 2 mm^2 was used for removal of SiN overlayer. Some dimples on the surface caused by Ar-ion sputter was observed in the SEM image, the sample was rotated during the sputter in order to prevent the growing of surface roughness. After initial cleaning by Ar-ion sputter, the Gd surface was exposed to oxygen at room temperature. Oxygen was admitted at 1.3 x 10^{-6} Pa into the chamber through a variable leak valve and injected toward the Gd surface using the gas doser.

4.2.3. Results and Discussion

High surface activity of Gd surface

Fig.4.11 shows the wide-scan AES spectra from Gd and Cu before/after oxygen exposure of 10 L. The oxygen peak intensity observed on Gd surface was ten times higher than that on Cu surface. It indicates that Gd surface has a very high activity for oxygen adsorption. In this FE-AES system, the partial pressure of oxidizing residual gas was estimated to be 8 x 10^{-9} Pa during the experiment [11]. The amount of oxidizing residual gas adsorbed on the Gd clean surface during the spectrum acquisition (15 min) is estimated to be 0.05L. The activity of Gd surface is too high to maintain its cleanliness against the residual gas adsorption even under the UHV condition. For example, if one keep the Gd surface cleaned by Ar sputter under the UHV, the Gd surface will completely cover with oxygen after 6 hours [11].

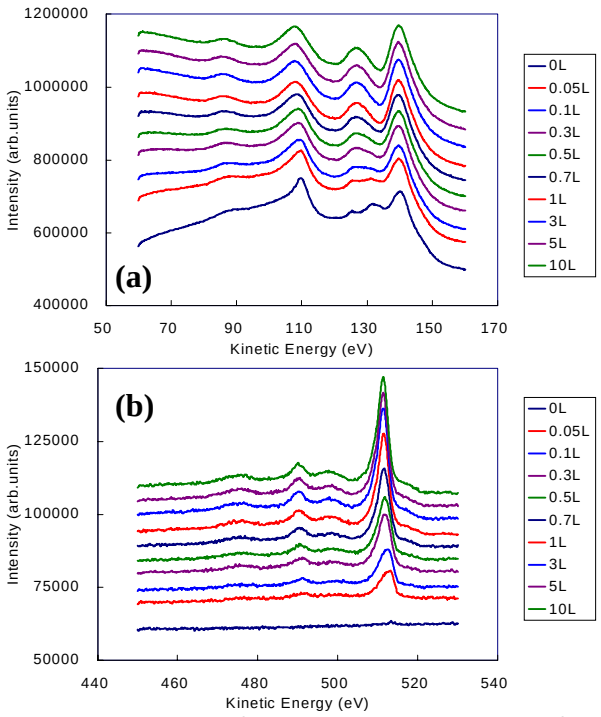

Fig. 4.12 Changes of narrow-scan AES Spectra of (a) Gd-NOO and (b) O-KLL with increasing oxygen exposures. (from the bottom spectrum to the top one)

Oxygen exposure experiments

The line shape changes in Gd NVV and O KLL as a function of oxygen exposure from 0 to 10 L are shown in Figs.4.12(a) and (b). With increasing oxygen exposure a new feature appeared around 125 eV between the main peaks of 110 eV and 140 eV in Gd NVV.

Along with the new feature, the energy shift of the main peak toward the lower energy was observed. These changes are similar to Tb NVV [2] and other rare earth [5-9].

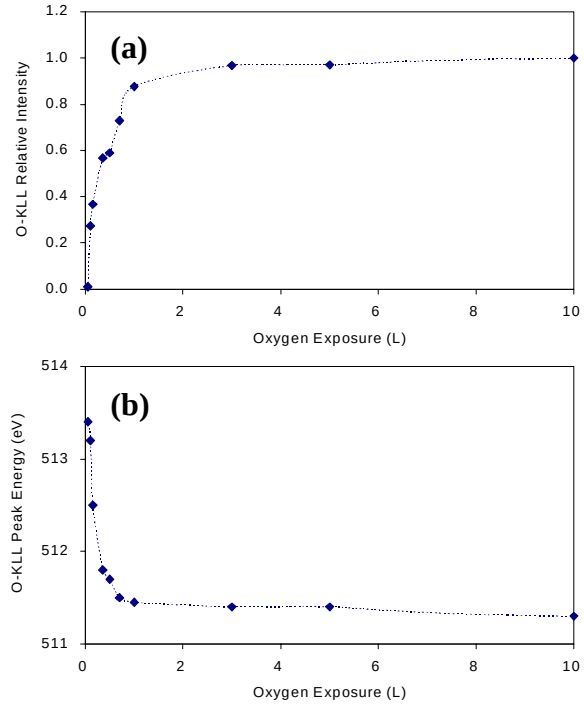

Fig. 4.13 Variation in (a) normalized area intensity and (b) peak energy of O-KLL as a function of oxygen exposures.

As for O KLL, the peak intensity increased and the peak energy slightly shifted toward the lower energy with increasing oxygen exposure. Figs.4.13(a) and (b) show the variation in the normalized intensity and the peak energy of O KLL as a function of oxygen exposure. Here the area intensity of O KLL peak after subtraction of the background by Shirley method was used, and normalized to the saturation intensity. The former rapidly increased at the beginning of oxygen exposure and reached the saturation at between 1 and 3 L. The latter rapidly shifted from 513.4 eV to 511.5 eV after the oxygen exposure of 0.7 L and remained around 511.5 eV against the further oxygen exposure.

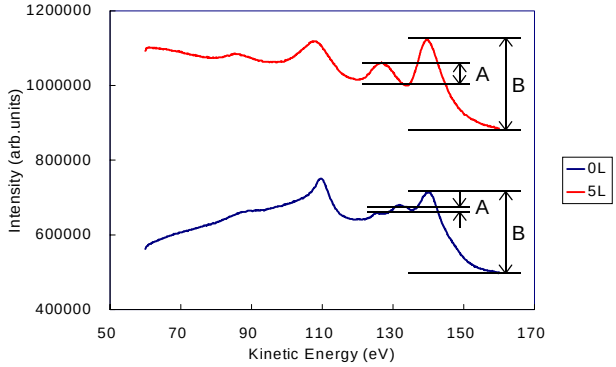

Fig. 4.14. Proposed index for Gd oxidation.

Gd oxidation index

In order to extract the quantitative index of Gd oxidation from the line shape changes on the direct AES spectra, the peak height ratio of A/B was discussed. Where “A” denotes the difference in intensity between the peak around 125 eV and the minimum around 135 eV, and “B” denotes the difference between the peak around 140 eV and the peak tale at 160eV. As an example of the definition for “A” and “B”, two spectra from 0 and 5 L exposed surface are shown in Fig.4.14.

Fig.4.15(a) shows the correlation between the peak height ratio defined above as an index for Gd oxidation and the oxygen exposure. The Gd oxidation index rapidly increases and reaches the saturation at around 1 L. The Gd oxidation index is well correlated with the normalized intensity of O KLL, as shown in Fig.4.15(b). The normalized intensity of O KLL can be regarded as the oxygen coverage, where the oxygen coverage on the saturated surface = 1. Thus, the relationship is described as follows:

[Gd oxidation index]

= 0.348 x [oxygen coverage] – 0.081

The Gd oxidation index proposed here can be used as a quantitative index for the oxygen coverage, which is deeply related with the degree of oxidation.

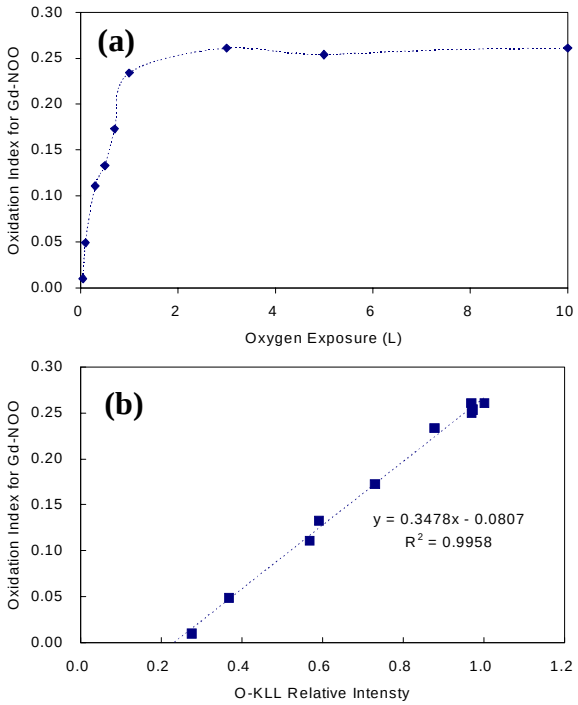

Fig. 4.15 (a) Variation in the oxidation index for Gd-NOO as a function of oxygen exposures.
(b) Correlation between O-KLL intensity and Gd Index.

Initial oxidation process

In Fig.4.13(a) and Fig.4.15(a), it can be seen the small step on the first increasing slope around 0.5 L, corresponding to the oxygen coverage of 0.6. If the final species forming on the oxygen-saturated Gd surface is the highly oxidized species like Gd_2O_3, the oxygen coverage of 0.6 may correspond to GdO formation. GdO is supposed to be an intermediate state formed before the stable species formation on the Gd surface [10]. The small step on the increasing slope means the turning point of the initial oxidation process. In accordance with the small step around 0.5 L, the peak energy shift of O KLL from 513.4 eV to 511.5 eV has just finished around 0.7 L.

According to the UPS and XPS study by Wandelt *et al.* [10] two peaks were observed in O 1s XPS spectra of the evaporated Gd films. At low oxygen exposures the peak was situated at around 530 eV. For the higher exposures second peak at 532.5 eV was growing. It should be pointed out here that the reported energy difference of O 1s between the initial forming species and the following species is similar to our results of O KLL.

Based on the results obtained, the initial oxidation process on the Gd surface is deduced as follows: In the initial stage, oxygen chemisorbed on the Gd surface and formed the intermediate species like GdO. The formation of GdO species was completed after the oxygen exposure of around 0.5 L. Then the intermediate species changed to the more stable species like Gd_2O_3. However, there is not sufficient evidence of the final species at present. Further investigation about the chemical species forming on the Gd surface will be held in the following section 4.3 based on ToF-SIMS results.

4.2.4. Conclusions

Initial oxidation progressing on the Gd surface was studied by AES with adequate energy resolution ranged from 0.5% to 0.1%, where the latter is as high as that of XPS. From the changes in the line shapes of Gd NVV, the quantitative index for Gd oxidation was successfully extracted. The proposed Gd oxidation index is well correlated with the O KLL peak intensity, that is to say, with the oxygen coverage. Along with the line shape changes, small energy shift of the O KLL peak can be observed in the highly energy-resolved spectra.

References

[1] 今村修武, 金属表面技術, 38, 408 (1987).
[2] Y. Abe, A. Kato and T. Nakamura, Surf. Interface Anal., 22, 14 (1994).
[3] M. P. Seah, G. C. Smith and M. T. Anthony, Surf. Interface Anal., 15, 293 (1990).
[4] 鈴木峰晴, 丸山達哉, 大塚芳郎, 小泉光生, 名越正泰, 関根哲, J. Surf. Anal., 3, 589 (1997).
[5] W. Faerber and P. Braun, Surf. Sci., 41, 195 (1974).
[6] D. Weller and D. D. Sarma, Surf. Sci., 171, L425 (1986).

[7] M. Ushio, S. Higuchi, M. Asano, H. Misaki and Y. Nakanishi, Vacuum, 41, 25 (1990).
[8] G. L. P. Berning, H. C. Swart and B. de Witt, Appl. Surf. Sci., 64, 1 (1993).
[9] M. Hirasaka, M. Sekiya and T. Miki, J. Vac. Sci. Technol., A11, 503 (1993).
[10] K. Wandelt and C. R. Brundle, Surf. Sci., 157, 162 (1985).
[11] 阿部芳巳, J. Surface Analysis, 7, 203 (2000).

4.3. In-situ Monitoring of Initial Oxidation on Gd by ToF-SIMS

Abstract

ToF-SIMS is proposed to be applicable to the characterization of initial oxidation state of metal surfaces, because of many advantages such as quick data collection, parallel detection of wide mass range, high surface sensitivity, high mass accuracy, ability for hydrogen and its compounds analysis, and so on. In this work, the initial oxidation state of Gd has been studied with ToF-SIMS, by detecting surface compounds directly as their fragment ions. Under oxygen exposure of 1.0 x 10^{-5} Pa, positive and negative cluster ions, composed of Gd, O and H, were collected at every cycle of 1 s. Characteristic variation in intensities among the typical ions was observed on both positive and negative spectra, which was supposed to be related with the changes of Gd chemical structure. Based on the results obtained, the initial oxidation process on Gd surface was deduced as follows: at first, suboxide of Gd was generated, followed by hydroxide forming, and finally the surface was covered with Gd hydroxide. In conclusion, ToF-SIMS is found to be useful for in-situ monitoring of initial oxidation.

4.3.1. Introduction

ToF-SIMS has been widely used for chemical structure analysis for the organic materials [1], trace element analysis [2], and so on. This is because ToF-SIMS can give information on the surface species by detection of the secondary ions, which are characteristic of chemical species on the surface, with high surface sensitivity, high mass accuracy and the ability for parallel detection of wide mass range. Recently the studies focused on the metal oxide catalyst have been reported [3-7]. Some of the advantages of ToF-SIMS for application to the metal surfaces are (1) quick data collection than electron spectroscopy such as AES or XPS, (2) ability for the detection of hydrogen and hydrogen-containing compounds. The ability of hydrogen detection is expected to enable distinguishing hydroxide from oxide. It can be also expected to be useful for evaluation of the chemical species directly from the characteristic fragmentation pattern of each species, which is very useful for initial oxidation study. But the initial oxidation study on metal surface using SIMS has not been reported since 1970's, when vigorous studies by S-SIMS were performed by Benninghoven [8]. In those days, mass resolution of quadrupole mass spectrometer was quite poor and it was difficult to distinguish the peaks at the same nominal mass. Now a day ToF mass spectrometer is developed, which enables us to obtain the spectra with high mass resolution and short acquisition time over the wide mass range.

In this section, the initial oxidation process of the Gd surface is investigated with ToF-SIMS. Gd is one of rare earth (RE), and RE is very important element in industry, for example, the memory layer for magneto-optical media [9]. In the previous sections, the initial oxidation of Tb and Gd are studied by use of AES [10,11]. Based on the results obtained, quantitative index for surface oxidation can be extracted from the changes in NVV Auger line shapes. But it is difficult to estimate the surface species, such as oxides or hydroxides by the use of AES.

Here I propose a new approach for investigation of the initial oxidation on metal surface by ToF-SIMS through the successively quick data collection in every 1 s under the oxygen exposure.

4.3.2. Experimental

Materials

A pure Gd thin film of 185 nm thick protected by SiN layer was prepared with the

same procedure described in 4.2.2. In the ToF-SIMS apparatus in-situ removal of SiN overlayer was performed by Ar-ion sputtering. Schematic view of cross section and negative total ion image of the sample are shown in Fig.4.16.

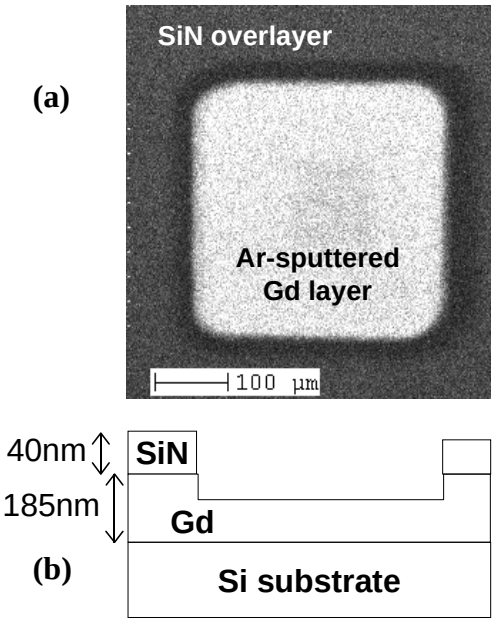

Fig. 4.16. The Gd sample used.
(a) Negative ion image from 500 x 500 μm^2 after the removal of SiN overlayer by Ar sputter and (b) schematic cross section are shown.

Measurements

ToF-SIMS measurements were performed in ION-TOF, TOF-SIMS IV system. A Ga liquid metal ion gun was used for primary ion source. Pulsed $^{69}Ga^+$ ions were dosed on the surface, with energy of 25 keV, current of 3.7 pA, pulse width of 0.7 ns, pulse frequency of 10 kHz, raster size of 109 um x 109 um and incidence angle of 45 degree. Secondary ions emitted from the surface were detected with reflectron-type ToF mass spectrometer in every 1 s. Under these conditions, dose density of Ga^+ primary ions was 1.9 x 10^{11} ions/(cm^2*s). Measurements of positive ions and negative ions were separately performed.

An Ar ion gun, operating at energy of 3 keV, current of 100 nA, raster size of 300 μm x 300 μm, was used for sputter removal of the SiN overlayer. Under these conditions, dose density of Ar^+ ions was 6.9 x 10^{14} ions/cm^2/s.

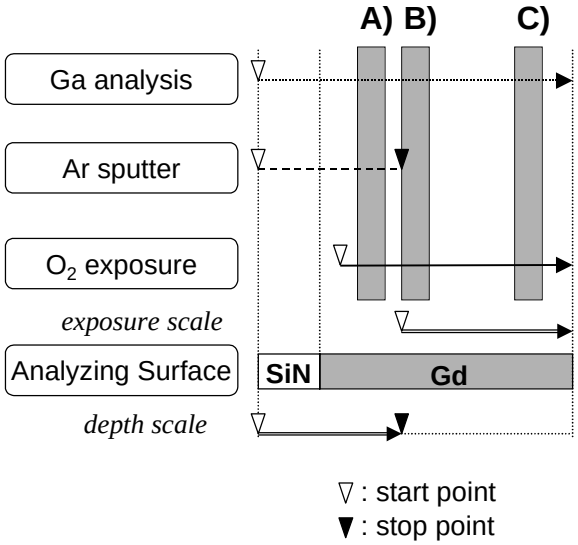

Fig. 4.17. Experimental procedures of oxygen exposure. Characteristic three regions are shown: (A) under both Ar sputter and oxygen exposure, (B) just after the stop of Ar sputter under oxygen exposure, and (C) far after the stop of Ar sputter under oxygen exposure, respectively.

The process of oxygen exposure experiments are illustrated in Fig.4.17 and the details are as follows:

1) A SiN overlayer was completely removed by Ar sputter to reveal the Gd surface. Then pure oxygen gas was introduced to the analytical chamber through a variable leak valve. The pressure of oxygen was controlled as 1.0 x 10^{-5} Pa. Under these conditions, the exposure of oxygen was 7.5 x 10^{-2} L/s.

2) Pulsed two ion beams, Ar^+ for surface sputter and Ga^+ for ToF-SIMS analysis, were alternatively dosed, which is called “interleave” mode. On the Gd surface, oxygen adsorption and Ar sputter competitively occurred. In this work, the rates of oxygen molecules and Ar ions injection were 3 x 10^{13} molecules/(cm^2*s)

and 7 x 10^{14} ions/(cm^2*s), respectively. In this case, the observed spectra correspond to those without oxygen exposure. The oxygen exposure is regarded as 0 L under these conditions.

3) ToF-SIMS analysis by pulsed Ga^+ ion beam was performed till the total oxygen exposure reached at around 50 L just after the stop of Ar sputter.

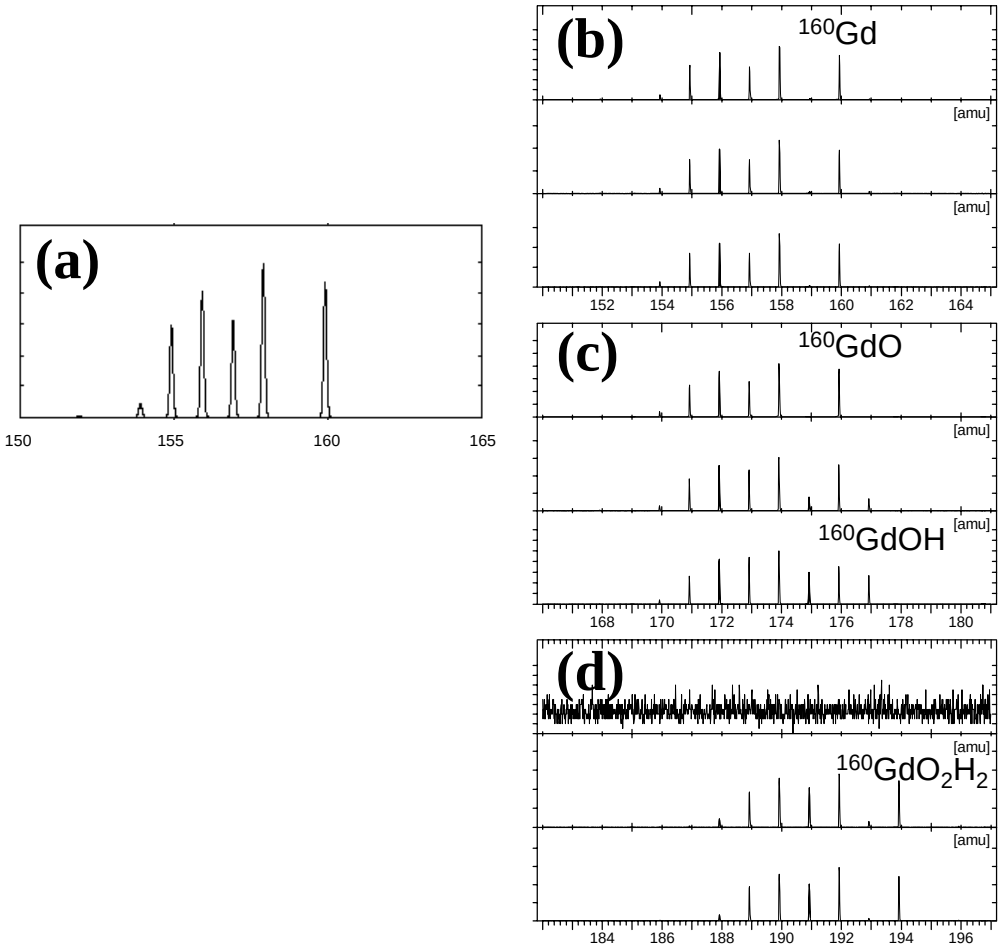

Fig. 4.18. (a) Calculated isotope ratio for Gd. (b-d) Positive ToF-SIMS spectra from Gd surface under oxygen exposure of 1.0 x 10^{-5} Pa, in the mass region of (b) Gd, (c) $GdOH_x$ and (d) GdO_2H_x, respectively. Each panel shows three spectra: (top) under Ar sputter, (middle) after low oxygen exposure, and (bottom) after high oxygen exposure, respectively.

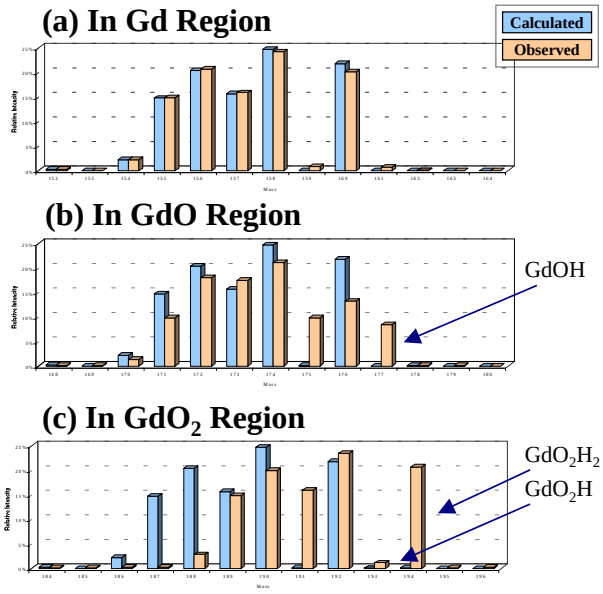

Fig. 4.19. Comparison of calculated isotope ratio for Gd and observed relative peak intensities in positive ToF-SIMS spectra from Gd surface under oxygen exposure of 1.0 x 10^{-5} Pa, in the mass region of (a) Gd, (b) $GdOH_x$ and (c) GdO_2H_x, respectively.

4.3.3. Results and Discussion

Mass spectral analysis

Positive ion mass spectra in the mass region of GdO_xH_y obtained from the Gd surface under Ar sputter, after low and high oxygen exposures are shown in Figs.4.18(b)-(d), respectively. Calculated isotope ratio for Gd, ^{152}Gd : ^{154}Gd : ^{155}Gd : ^{156}Gd : ^{157}Gd : ^{158}Gd : ^{160}Gd = 0.20% : 2.18% : 14.80% : 20.47% : 15.65% : 24.84% : 21.86% [12], is shown in Fig.4.18(a). Observed relative peak intensities in Figs.4.18(b)-(d) are compared with the calculated one in Fig.4.19. Whereas the relative peak intensities observed in the Gd region are coincident with the calculated pattern (Fig.4.19(a)), an additional peaks arising from $GdOH^+$ are observed after the oxygen exposure in the GdO_xH_y region (Fig.4.19(b)). In the GdO_2H_y region (Fig.4.19(c)), $GdO_2H_2^+$ are detected. It is noted that the severe mass interference among the GdO_xH_y peaks should occur because Gd has as many as 7 isotopes. In order to avoid the severe interference, I only discussed the results about ^{160}Gd, which is isolated in the higher mass range among the 7 isotopes and has the secondly high proportion of 21.86%.

Changes in positive ion mass spectra

The overview of positive mass spectra obtained from the Gd surface under Ar sputter, after low and high oxygen exposures are shown in the left part of Fig.4.20. In the mass range *m/z* 0-800, Gd_x (x = 1-4) and $Gd_xO_yH_z$ cluster ions were observed in accordance with their isotope ratio (Fig.4.20(a)). GdO^+ peak was most intense in the GdO_xH_y region, and a $GdO_2H_2^+$ peak appeared after high oxygen exposure (Fig.4.20(b)). Gd_2^+, Gd_2O^+ and $Gd_2O_2^+$ were observed under Ar sputter in the $Gd_2O_xH_y$ region. On the oxygen-exposed surface, Gd_2^+ and Gd_2O^+ were decreasing with increasing oxygen exposure and a $Gd_2O_3H^+$ peak appeared (Fig.4.20(c)).

Changes in negative ion mass spectra

The overview of negative mass spectra of the Gd surface under Ar sputter, after low and high oxygen exposures are shown in the right part of Fig.4.20. In the mass range *m/z* 0-800, Gd_x (x = 1-4) and $Gd_xO_yH_z$ cluster ions were observed in accordance with their isotope ratio (Fig.4.20(a)). GdO^- peak was most intense in the GdO_xH_y region, and $GdO_3H_2^-$ and $GdO_4H_4^-$ peaks appeared after oxygen exposure (Fig.4.20(b)). There were no peaks under Ar sputter in the $Gd_2O_xH_y$ region. On the oxygen-exposed surface, $Gd_2O_4H^-$ and $Gd_2O_5H_3^-$ peaks appeared (Fig.4.20(c)).

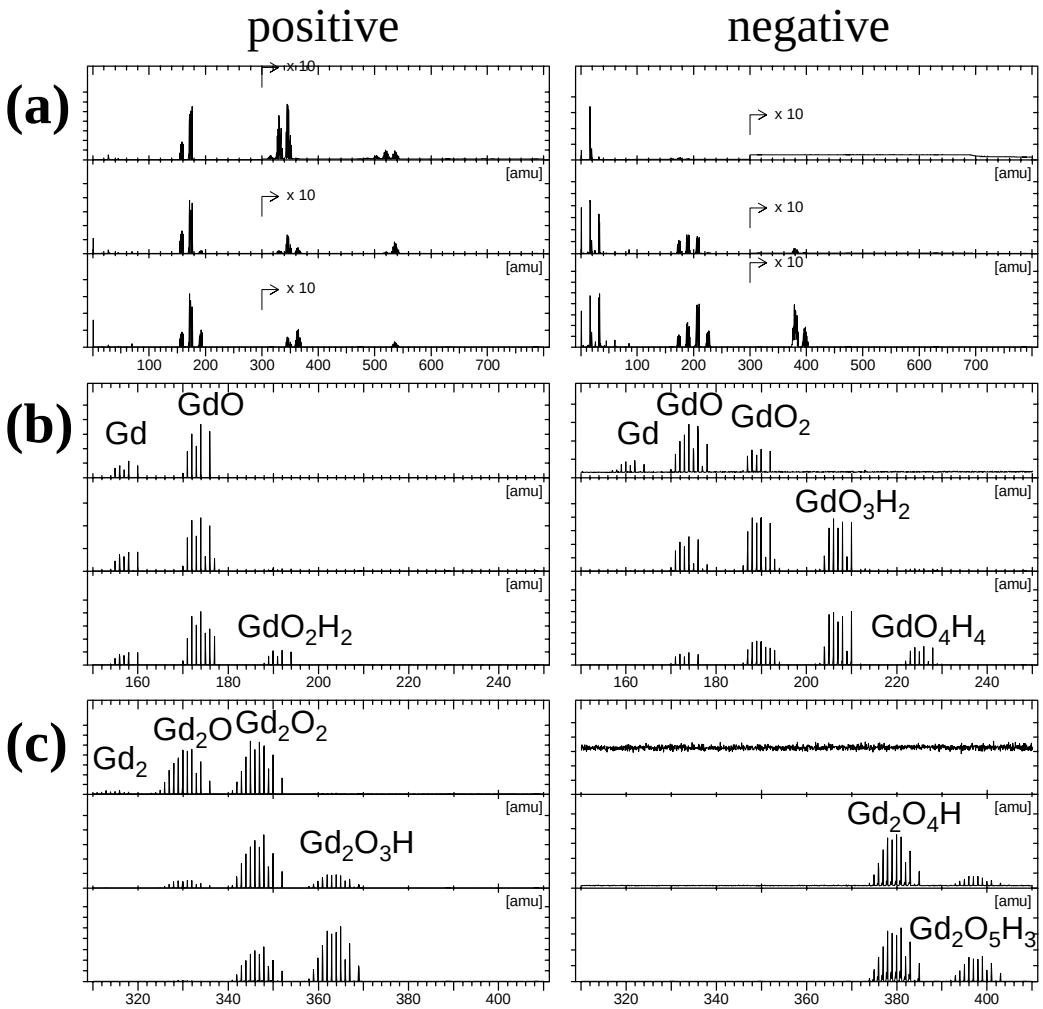

Fig. 4.20. ToF-SIMS Spectra from Gd surface under oxygen exposure of 1.0 x 10^{-5} Pa, in the mass range of (a) *m/z* 0-800, (b) *m/z* 150-250 and (c) *m/z* 310-410, respectively. Each panel shows three spectra: (top) under Ar sputter, (middle) after low oxygen exposure, and (bottom) after high oxygen exposure, respectively.

Estimation of the structure of observed cluster ions

The GdO_xH_y cluster ions are believed to originate from the hydroxide species on the surface. This result suggests that oxygen is dissociatively adsorbed on the Gd surface and then forms the surface hydroxide group as a result of trapping hydrogen from the residual gas.

As discussed in the previous section, the initial oxidation process is deduced as follows: a dissociatively adsorbed oxygen on Gd surface forms an intermediate (like GdO), followed by the formation of Gd_2O_3. According to the UPS and XPS study by Wandelt *et al.* [13], after high exposure of oxygen, Gd_2O_3 changes to the hydroxide. This is consistent with our results that directly indicate the hydroxide formation upon oxygen exposure. However, our results show that the hydroxide formation starts from the initial stage, which is conflict with the Wandelt's results. It is considered to be due to the fact that the information depth of ToF-SIMS is smaller than UPS and XPS, or ToF-SIMS is more sensitive to the hydrogen detection.

Estimated chemical structure for observed cluster ions are shown in Table 4.1. Here the oxidation number of oxygen and hydrogen is regarded as –2 and +1, respectively, and the valence of Gd is formally described.

Table 4.1. Estimated chemical structure for observed cluster ions of $GdO_xH_y^{+/-}$.

Observed ion	Estimated structure
Gd^+	$Gd(I)^+$
GdO^+	$Gd(III)O^+$
$GdOH^+$	$Gd(II)OH^+$
$GdO_2H_2^+$	$Gd(III)(OH)_2^+$
GdO^-	$Gd(I)O^-$
GdO_2^-	$Gd(III)O_2^-$
GdO_2H^-	$Gd(II)O(OH)^-$
$GdO_3H_2^-$	$Gd(III)O(OH)_2^-$
$GdO_4H_4^-$	$Gd(III)(OH)_4^-$

Proposed initial oxidation process

Next, I would like to discuss about the initial oxidation process on the Gd surface, through the inspection of intensity variation of the observed $GdO_xH_y^{+/-}$ cluster ions as a function of oxygen exposure. Figs.4.21(a) and (b) show the variation in intensity among $^{160}GdO_xH_y^{+/-}$ peaks observed in Fig.4.20. In order to examine the order and degree of changes in intensity of each peak shown in Fig.4.21, the intensities normalized to their saturated ones after the high oxygen exposure are plotted versus the oxygen exposure in log scale in Fig.4.22.

With increasing oxygen exposure, the intensities of $Gd(I)^+$ and $Gd(III)O^+$ increased at first, followed by the successive increase of $Gd(II)OH^+$ and $Gd(III)(OH)_2^+$, among the positive ions shown in Fig.4.22(a). In consistent with the variation in positive ions, the intensities of $GdO(I)^-$ and $Gd(III)O_2^-$ increased at first, followed by the increase of $Gd(II)O(OH)^-$ and $Gd(III)O(OH)_2^-$, and finally the intensity of $Gd(III)(OH)_4^-$ increased among the negative ions shown in Fig.4.22(b). It should be pointed out that at the first stage the cluster ions of $Gd(I)O_x^{+/-}$ and $Gd(III)O_x^{+/-}$ without hydrogen atoms appear. At the second stage the cluster ions of $Gd(II)O_x(OH)_y^{+/-}$ and $Gd(III)O(OH)_x^-$ both with oxygen atoms and hydroxyl groups tend to increase. At the final stage after high oxygen exposure the cluster ions of $Gd(III)(OH)_x^{+/-}$ increase.

Based on the results obtained, the initial oxidation process on the Gd surface is deduced as follows:

1st stage: A kind of suboxide state containing both Gd(I) and Gd(III) is formed on the Gd surface at the beginning of oxygen exposure.

2nd stage: By trapping of hydrogen the suboxide state changes to an intermediate state such as hydroxide oxide state containing both Gd(II) and Gd(III) after low oxygen exposure.

3rd stage: By further trapping of hydrogen the intermediate state is immediately stabilized as a hydroxide state containing Gd(III) after high oxygen exposure.

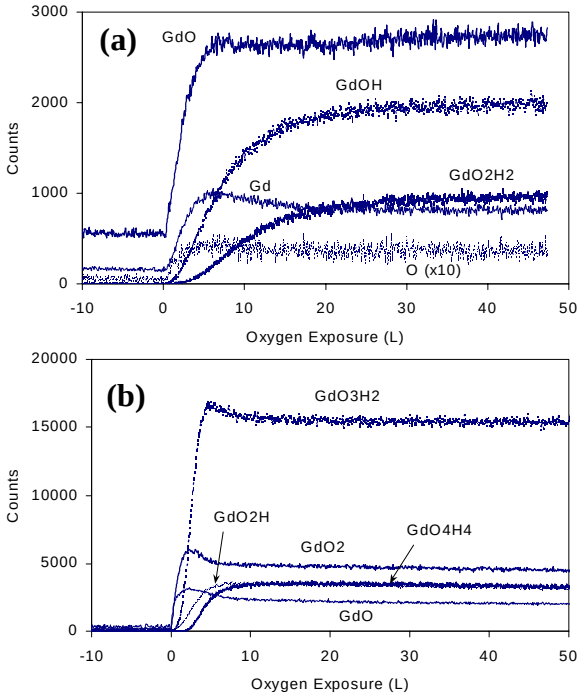

Fig. 4.21. Variation in intensities among $GdO_xH_y^{+/-}$ as a function of oxygen exposure: (a) positive and (b) negative ions, respectively.

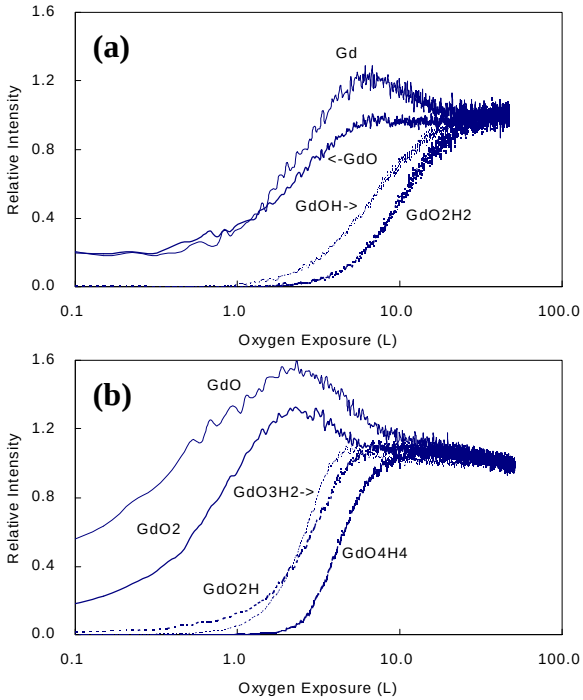

Fig. 4.22. Variation in normalized intensities among $GdO_xH_y^{+/-}$ as a function of oxygen exposure: (a) positive and (b) negative ions, respectively.

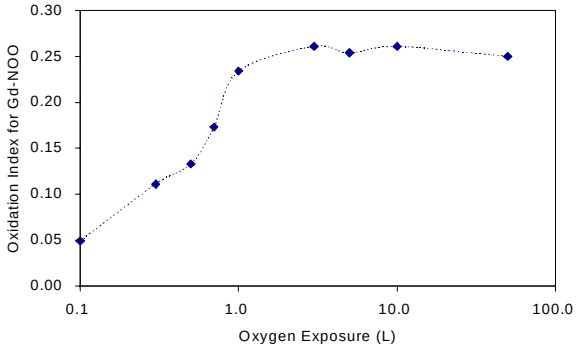

Fig. 4.23. Variation in the oxidation index for Gd-NOO obtained by AES as a function of oxygen exposure.

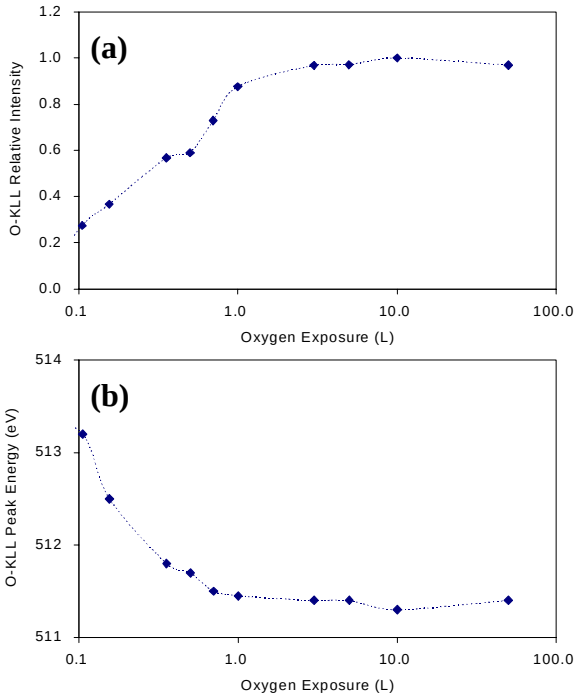

Fig. 4.24. Variation in (a) normalized intensity and (b) peak energy of O-KLL obtained by AES as a function of oxygen exposure.

4.3.4. Proposed initial oxidation process by HR-AES and ToF-SIMS

In previous section 4.2, the initial oxidation process on the Gd surface has been discussed on the basis of HR-AES [11]. In order to discuss the results obtained by ToF-SIMS and HR-AES comparatively, the variations in Gd oxidation index, normalized intensity of O KLL and its peak energy versus the oxygen exposure in log scale are plotted in Fig.4.23 and Fig.4.24, in the same format as Fig.4.22. The Gd oxidation index and O KLL intensity increase with increasing oxygen exposure and saturate around 1 L. At the beginning of oxygen exposure, the O KLL intensity is increasing linearly against the logarithm of oxygen exposure. This behavior is believed to correspond to the suboxide formation at the 1st stage. There is a small step on the slope at ~0.5 L, and this step is interpreted to correspond to the turning point from 1st stage to 2nd stage, where the suboxide state starts to change to the intermediate state. It is considered that the suboxide formed on the Gd surface tends to trap hydrogen forming hydroxide and the sticking probability of oxygen changes. Whereas there is no significant changes on the AES spectra after the 2nd stage, the variation in intensity is still progressing on the ToF-SIMS spectra and the change from the 2nd stage to the 3rd stage is clearly observed. Ability of ToF-SIMS for hydrogen detection enables us to prove the final process in the initial oxidation.

4.3.5. Conclusions

The advanced use of ToF-SIMS is found to be applicable to the in-situ monitoring of initial oxidation of metal surfaces. Characteristic variation in intensity of the typical secondary ions with increasing oxygen exposure is observed and the initial oxidation process on the Gd surface is proposed.

ToF-SIMS has many advantages in quick data collection, parallel detection of wide mass range, high surface sensitivity, high mass accuracy, ability for hydrogen and its compounds detection. Quick data collection and parallel detection enable us to monitor the surface reaction. High mass resolution and high mass accuracy confirm the deduction of surface species correctly. Ability for hydrogen detection is useful to distinguish hydroxide from oxide. These advantages can complement the conventional electron spectroscopic techniques such as AES and XPS.

References

[1] Y. Abe, M. Shibayama and T. Matsuo, Surf. Interface Anal. 30, 632 (2000).
[2] P. Lazzeri, A. Lui, L. Moro and L. Vanzetti, Surf. Interface Anal. 29, 798 (2000).
[3] N. M. Reed and J. C. Vickerman, SIMS VII 793 (Wiley, 1989).
[4] F. De Smet, M. Devillers, C. Poleunis and P. Bertrand, J. Chem. Soc., Faraday Trans. 94, 941 (1998).
[5] D. Briggs and S. R. Bryan, SIMS XII 875 (Elsevier, 2000).
[6] J. C. Vickerman, A. Oakes and H. Gamble, Surf. Interface Anal. 29, 349 (2000).
[7] S. B. Bukallah, M. Houalla and D. M. Hercules, Surf. Interface Anal. 29, 818 (2000).
[8] A. Benninghoven, Surf. Sci. 35, 427 (1973).
[9] 今村修武,金属表面技術 38, 408(1987).
[10] Y. Abe, A. Kato and T. Nakamura, Surf. Interface Anal. 22, 14 (1994).
[11] 阿部芳巳, J. Surf. Anal. 7, 203 (2000).
[12] 国立天文台編, 理科年表 第 72 冊 (丸善, 1999).
[13] K. Wandelt and C. R. Brundle, Surf. Sci. 157, 162 (1985).

Chapter 5

Applications of ToF-SIMS to Magnetic Recording Disks

In this chapter 5, ToF-SIMS is applied to the analysis of magnetic recording disks. There are two main objectives of ToF-SIMS applications in this work. One is the characterization of lubricant films covering on the carbon overcoats. The lubricant film with thickness around 1 nm is a sort of the organic thin film. An analytical tool providing molecular structure information is necessary to characterize the lubricant films, but it has been difficult to obtain sufficient information with conventional surface sensitive techniques. The other is the analysis of micro-corrosion in order to qualify the carbon overcoats. Surface sensitive tool with high sensitivity for trace elements and high spatial resolution is necessary for detection of localized trace elements on the surface. For the application of ToF-SIMS to the micro-corrosion analysis, its information depth is carefully discussed.

5.1. Characterization of Lubricant Films on Magnetic Recording Disks by ToF-SIMS

Abstract

The structural characterization of Z-DOL, which is currently the lubricant of choice for magnetic recording disks, formed as films of variable thickness on carbon overcoated disks has been studied by ToF-SIMS. The relationship between the peak intensity of dominant fragment ions in the positive mass spectra and the lubricant thickness was carefully examined. The $CF_3^+/C_2F_5^+$ intensity ratio is found to be useful as an index of the lubricant thickness. The monomer ratio between ethylene and methylene units of the Fomblin backbone can be extracted from the plot of normalized intensity of $C_2F_4O^+$ against the $CF_3^+/C_2F_5^+$ ratio. The chemical bondability of the lubricant to the carbon overcoat surface can be examined through a plot of normalized intensity of $CF_2CH_2OH^+$ against the $CF_3^+/C_2F_5^+$ ratio.

5.1.1. Introduction

In magnetic recording media, surface lubrication is essential to avoid catastrophic wear and consequent signal loss. Perfluoro-polyethers (PFPEs) are currently the lubricant of choice for magnetic disks [1-10]. One of the commercially available and most-often used PFPEs is Fomblin Z-DOL. Z-DOL has hydroxyl end groups and the following structure: $HO\text{-}CH_2\text{-}CF_2O\text{-}(C_2F_4O)_m\text{-}(CF_2O)_n\text{-}CF_2\text{-}CH_2OH$.

The hydroxyl end groups play crucial role in the chemical bonding to the carbon overcoats. Schematic representation of the chemical interaction between the Fomblin Z-DOL and the functional group on the carbon overcoat surface is shown in Fig.5.0.0. The Z-DOL molecules bonded to the carbon surface are believed to form a “bonded layer”, which has high resistivity against the wear at the head-disk interface (HDI). The bonded layer must be covered with free Z-DOL molecules, which is called “free layer”, in order to reduce the friction force.

Lubricant properties such as thickness, uniformity, impurity content and bondability to the overcoat surface are important parameters for assuring proper functionality of the magnetic recording disks. ToF-SIMS is a suitable technique for analysis of lubricant properties because of high sensitivity, a wide mass range, high mass resolution and high lateral resolution [11,12].

In this section 5.1, the structural characterization of Z-DOL films of variable thickness on carbon overcoats is performed with ToF-SIMS. From a statistical point of view, relative intensities of key fragments are found to be correlated with some lubricant properties.

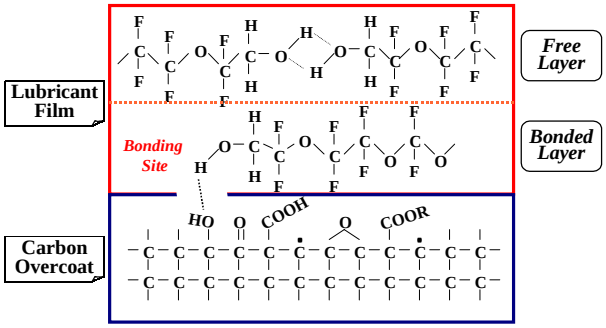

Fig. 5.0.0. Schematic representation of the Fomblin Z-DOL film coated on the carbon overcoat.

5.1.2. Experimental

Materials

The four kinds of Z-DOL lubricants, denoted A, B, C and D, which are listed in Table 5.1, were purchased from Ausimont of Italy. The number-average molecular weight (M_n) and weight-average molecular weight (M_w) measured by gel permeation

chromatography (GPC), and the monomer ratio between ethylene and methylene units of the Fomblin backbone, *m/n*, measured by nuclear magnetic resonance spectroscopy (NMR) are summarized in Table 5.1.

Table 5.1. Lubricants used.

Lubricant	M_n	M_w	m/n
A	1800	2000	0.87
B	5100	5600	1.10
C	4300	5900	0.68
D	3900	4900	0.96

Table 5.2. Samples of Z-DOL films used.

Sample number	Lubricant	Thickness (nm)	Anneal	Wash-off with PF
#1	A	1.6	**none**	none
#2	B	1.1	**none**	none
#3	B	1.6	**none**	none
#4	A	1.0	100℃	none
#5	A	4.3	100℃	none
#6	A	1.5	100℃	none
#7	A	0.7	100℃	none
#8	A	1.0	100℃	none
#9	A	1.4	100℃	none
#10	A	2.2	100℃	none
#11	A	1.5	100℃	none
#12	C	1.0	100℃	none
#13	C	1.3	100℃	none
#14	C	1.1	100℃	none
#15	C	1.4	100℃	none
#16	C	1.4	100℃	none
#17	D	1.1	100℃	none
#18	D	1.4	100℃	none
#19	D	1.1	100℃	none
#20	D	1.4	100℃	none
#21	D	1.7	100℃	none
#22	B	1.1	100℃	none
#23	B	1.5	100℃	none
#24	A	1.1	**150℃**	none
#25	A	1.1	**150℃**	none
#26	A	1.5	**150℃**	none
#27	A	0.9	**200℃**	none
#28	A	0.7	100℃	**done**
#29	A	1.1	100℃	**done**
#30	A	0.9	100℃	**done**
#31	A	1.0	**150℃**	**done**
#32	A	1.0	**150℃**	**done**
#33	A	1.3	**200℃**	**done**

The Z-DOL lubricated samples used were 33 dip-coated films with the thickness ranged from 0.7 to 4.3 nm on the 15 nm thick nitrogenated carbon overcoat, tabulated in Table 5.2. Below the overcoat, a magnetic layer of 25 nm thick CoCrTaPt alloy and an

underlayer of 40 nm thick Cr were deposited on a NiP-plated Al substrate.

The thickness of the Z-DOL films was controlled by the solution concentration and drain speed, and measured by Fourier-transform infrared spectroscopy (FTIR) [13] and/or XPS [14] after the following treatments: annealing up to 100, 150 and 200 degree C, respectively, and/or washing with perfluorocarbon (PF) solvent.

These samples can be categorized into four groups: #1-#3 are "not annealed", #4-#23 are "normally annealed", #24-#27 are "highly annealed" and #28-#33 are "solvent-washed". An annealing can lead to increase the proportion of the chemically bonded lubricant, and the annealing at higher temperature is more effective. A solvent washing technique can be used to evaluate the chemical bondability of lubricants, because by the washing process physically bonded lubricant is almost removed from the disk surface and chemically bonded lubricant is selectively remained [7,8].

Measurements

ToF-SIMS was performed in a PHI TRIFT II system with a pulsed Ga liquid metal ion gun operating at 12 keV, 600 pA DC. The beam raster size was 40 x 40 μm^2. The mass resolution, $m/\Delta m$, for $CF_2CH_2OH^+$ at *m/z* 81 was always achieved over 10000. Positive ToF-SIMS spectra for the mass range of *m/z* 0-400 were acquired within 3 minutes. Under these conditions, total primary ion dose was estimated to be 8 x 10^{12} ions/cm^2, one order higher than the generally accepted static limit [15].

5.1.3. Results and Discussion

Reproducibility of peak intensities

At the beginning of the statistical discussion, the reproducibility of the intensities for typical peaks in ToF-SIMS spectra is examined. Positive ion mass spectra were measured 6 times from the different areas on the surface of sample #8. For this particular PFPE film, the dominant peaks are observed in positive ToF-SIMS spectra at *m/z* 12, 31, 47, 50, 69, 81, 97, 100, 116, 119 and 163 corresponding to positive fragment ions of C^+, CF^+, CFO^+, CF_2^+, $CFCHOH^+$, CF_3^+, $CF_2CH_2OH^+$, $C_2F_3O^+$, $C_2F_4^+$, $C_2F_4O^+$, $C_2F_5^+$ and $C_3F_5O_2^+$, respectively, in agreement with previous works [1-6,9,10]. The peaks at *m/z* 61 and 81 are characteristic of Z-DOL, originating from the hydroxyl end groups of $-CF_2-CH_2OH$.

The possible fragmentation paths of the Fomblin Z-DOL backbone and end group are shown in Figs.5.0.1(a)-(c). The ether bonding in the backbone tends to cleave by the energetic transfer from the primary ions. Typical fragment ions mentioned above can be generated through the C-O bond cleavage, followed by F addition or dissociation.

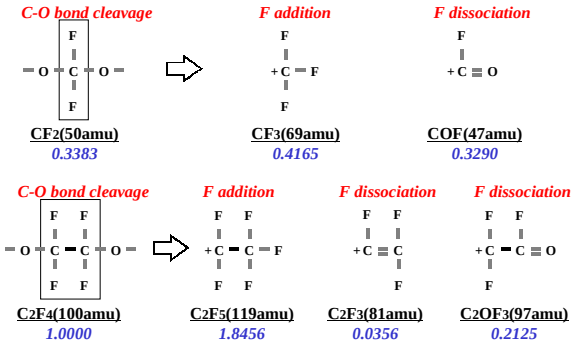

Fig. 5.0.1(a). Typical fragmentation paths from the Fomblin Z-DOL backbone. Peak intensities normalized to that of $C_2F_4^+$ obtained from the sample #5 are shown *in italic*.

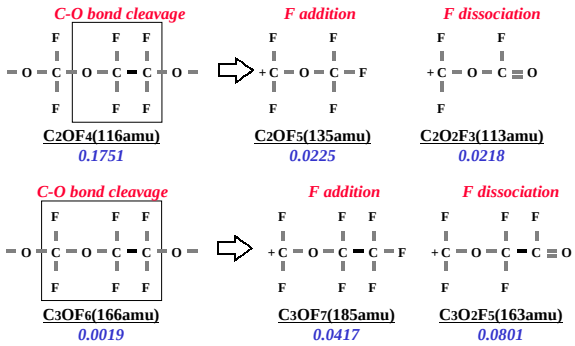

Fig. 5.0.1(b). Typical fragmentation paths from the Fomblin Z-DOL backbone. Peak intensities normalized to that of $C_2F_4^+$ obtained from the sample #5 are shown *in italic*.

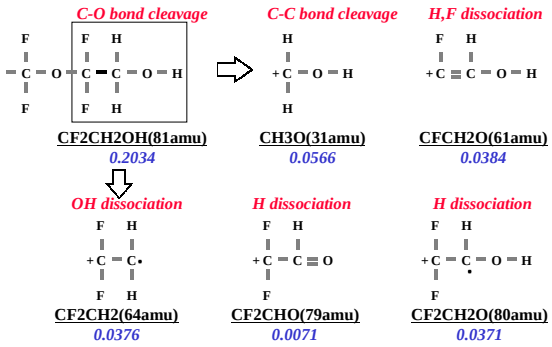

Fig. 5.0.1(c). Typical fragmentation paths from the Fomblin Z-DOL end group. Peak intensities normalized to that of $C_2F_4^+$ obtained from the sample #5 are shown *in italic*.

Averaged intensities normalized to that of $C_2F_4^+$ and their coefficient of variation among 6 measurements are tabulated in Table 5.3. The latter is typically below 5% and quite good reproducibility is obtained, which ensures the following discussion based on these typical peak intensities.

Table 5.3. Reproducibility of typical peak intensities among 6 times measurements.

Fragment Ion	Mass	Average Intensity	Coefficient of Variation
C	12	3.955	1.6%
O	16	0.026	3.0%
F	19	0.050	1.5%
CF	31	1.924	0.8%
COF	47	0.547	0.6%
CF2	50	0.650	0.8%
C2H2OF	61	0.035	0.7%
C2F2	62	0.011	3.7%
COF2	66	0.048	1.3%
CF3	69	0.555	0.4%
C2F3	81	0.042	1.5%
C2H3OF2	81	0.157	1.1%
C2OF3	97	0.160	1.0%
C2F4	100	1.000	-
C2OF4	116	0.139	0.8%
C2F5	119	1.346	0.7%
C3O2F5	163	0.040	0.9%
C3OF7	185	0.017	3.2%

Ratio of $CF_3^+/C_2F_5^+$ as an index of the lubricant thickness

In general, intensity in higher mass range is increased as the lubricant thickness increases. For example, Fig.5.0.2 shows the positive ToF-SIMS spectra obtained from the sample #7, #9 and #10 with thickness of 0.7, 1.4 and 2.2 nm, respectively. Relative intensities of the typical peaks normalized to that of CF_2^+ are shown in Fig.5.0.3. In the lower mass region the normalized intensities are decreasing with increasing thickness. On the contrary, the normalized intensities in the higher mass region are increasing. It should be emphasized that the fragmentation pattern of typical peaks obtained from the lubricant films strongly depends on its thickness.

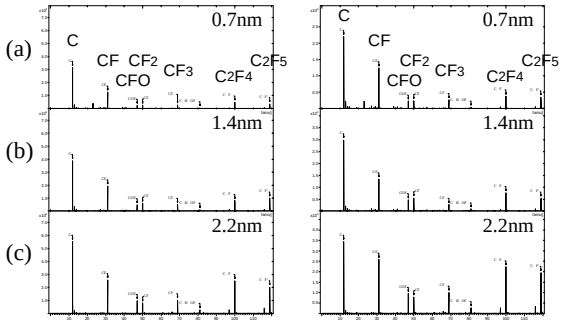

Fig. 5.0.2. Positive ToF-SIMS spectra from the Z-DOL films with thickness of (a) 0.7 nm, (b) 1.4 nm and (c) 2.2 nm, respectively. In (left) the same intensity scale; (right) the normalized intensity scale.

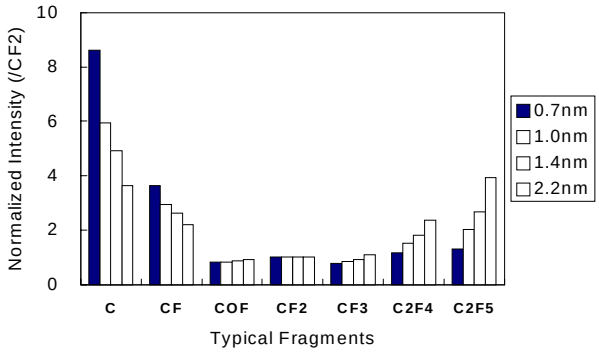

Fig. 5.0.3. Variation in intensity of typical fragment peaks obtained from the Z-DOL films with various thickness (#7-#10).

In order to introduce the thickness index, the thickness dependence of the intensity ratio between the adequate peaks is inspected. Fig.5.1 shows the ratio of $CF_3^+/C_2F_5^+$ in

intensity on each ToF-SIMS spectrum as a function of the lubricant thickness measured by FTIR. The relationship between the thickness and the ratio is almost uniform. It is explained by the fact that the energetic transfer from the primary ion to the lubricant film increases as the thickness decreases and the fragmentation is accelerated. In this case, the intensity of CF_3^+ increases compared with that of $C_2F_5^+$. Thus the $CF_3^+/C_2F_5^+$ ratio is supposed to be useful as an index of the lubricant thickness.

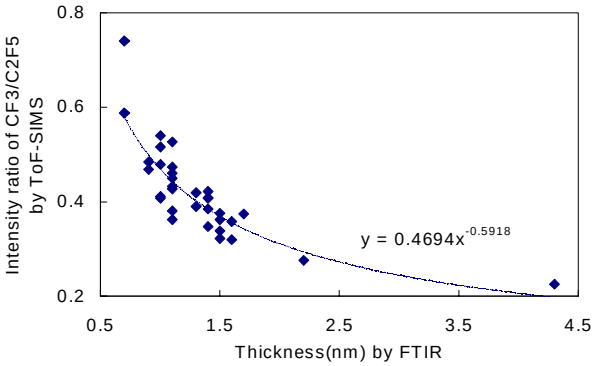

Fig. 5.1. Relationship between the lubricant thickness by FTIR and the ratio of $CF_3^+/C_2F_5^+$ by TOF-SIMS.

Monomer ratio of the Fomblin backbone

In Figs.5.2, 5.3 and 5.5, the intensities of three dominant fragments, $C_2F_3^+$, $C_2F_4O^+$ and $CF_2CH_2OH^+$, respectively, are plotted as a function of $CF_3^+/C_2F_5^+$ ratio. Each peak intensity is normalized to the $C_2F_4^+$ intensity on each spectrum, which is the dominant fragment originating from the backbone.

At first, the difference in behaviors of $C_2F_3^+$ and $C_2F_4O^+$, both of which are originated from the Fomblin backbone, is discussed. In the plot of $C_2F_3^+$, only a simple relationship among all the samples is seen in Fig.5.2. On the contrary, $C_2F_4O^+$ clearly shows the dependence upon the kind of lubricants in Fig.5.3.

Fig.5.4 shows the relationship between the *m/n* ratio of each lubricants measured by NMR and the normalized intensity of $C_2F_4O^+$ expected at $CF_3^+/C_2F_5^+$ = 0.4. The expected values of $C_2F_4O^+/ C_2F_4^+$ were estimated from Fig.5.3. It is clearly shown that the estimated $C_2F_4O^+$ intensity decreases as the *m/n* ratio increases.

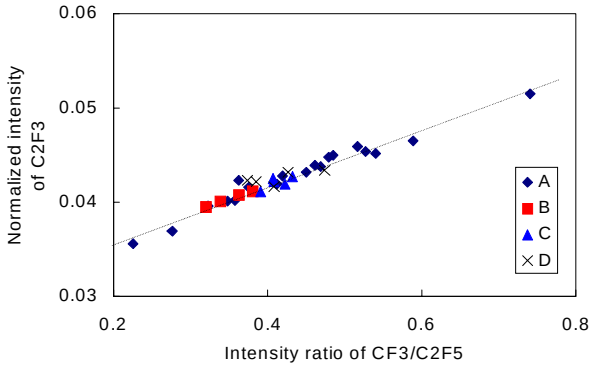

Fig. 5.2. Normalized intensity of $C_2F_3^+$ versus the ratio of $CF_3^+/C_2F_5^+$.

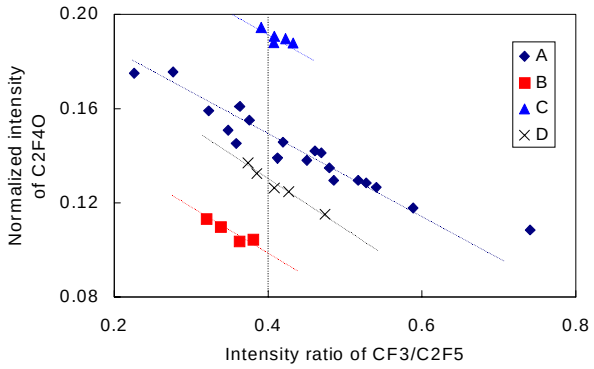

Fig. 5.3. Normalized intensity of $C_2F_4O^+$ versus the ratio of $CF_3^+/C_2F_5^+$.

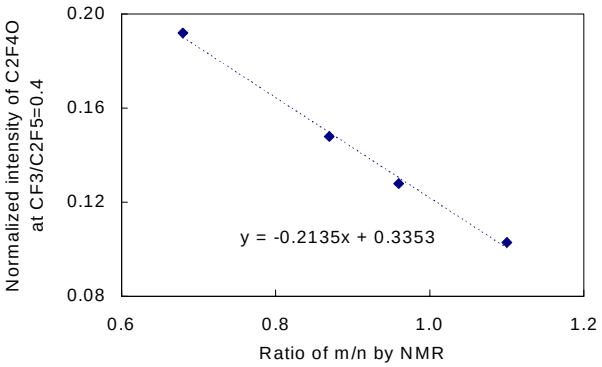

Fig. 5.4. Relationship between the normalized intensity of $C_2F_4O^+$ expected at $CF_3^+/C_2F_5^+$ =0.4 and the *m/n* ratio measured by NMR.

In general, the neighboring pair of methylene units increases as the *m/n* ratio decreases. It can be explained by the fact that the $C_2F_4O^+$ fragment can be generated from the neighboring pair of methylene units, but the $C_2F_3^+$ or $C_2F_4^+$ fragment can not. For this reason, the dependence upon the *m/n* ratio may be observed in the plot of $C_2F_4O^+/ C_2F_4^+$ (Fig.5.3), but not in the plot of $C_2F_3^+/ C_2F_4^+$ (Fig.5.2). Thus, information on the monomer ratio can be extracted using these plots.

The monomer ratio of lubricants as liquid can be measured by NMR before the coating. After the dip-coating, it is quite difficult to examine the monomer ratio actually as films on the disks. The monomer ratio is one of the important parameter to consider the proper functionality for wear resistance. The method mentioned above enables us to evaluate the monomer ratio of the lubricant films.

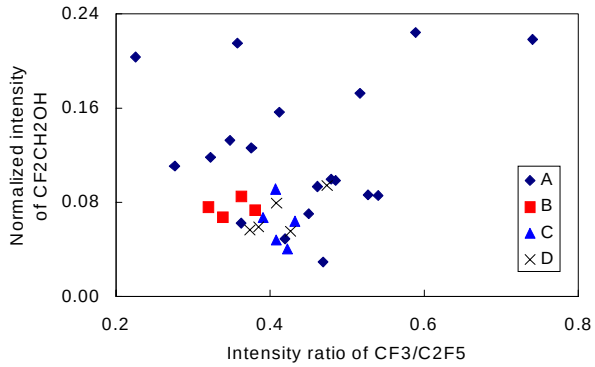

Fig. 5.5. Normalized intensity of $CF_2CH_2OH^+$ versus the ratio of $CF_3^+/C_2F_5^+$.

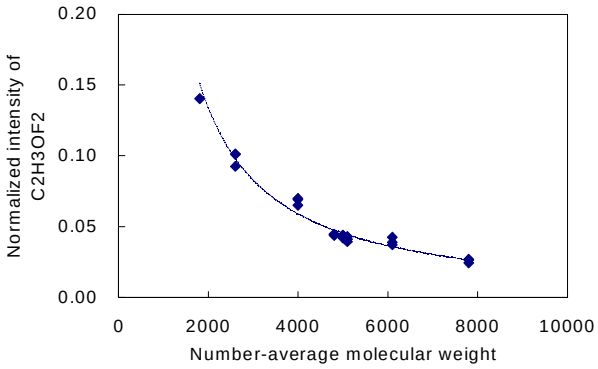

Fig. 5.6. Relationship between the normalized intensity of $CF_2CH_2OH^+$ and the *Mn* measured by GPC.

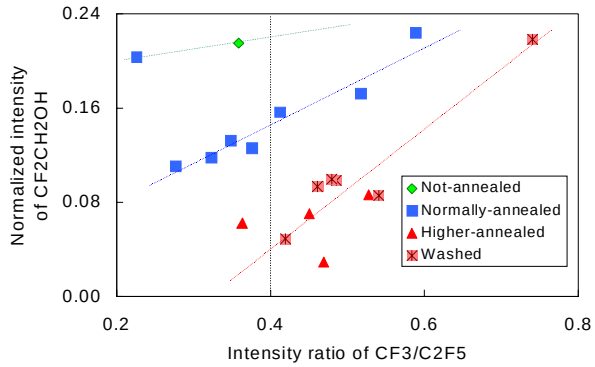

Fig. 5.7. Normalized intensity of $CF_2CH_2OH^+$ versus the ratio of $CF_3^+/C_2F_5^+$ in the case of lubricant A (*Mn*=1800).

Chemical bondability to the carbon surface

A unique behavior is observed for $CF_2CH_2OH^+$. The plot of $CF_2CH_2OH^+$ as a function of $CF_3^+/C_2F_5^+$ ratio (shown in Fig.5.5) is found to be quite different from those of $C_2F_3^+$ and $C_2F_4O^+$. The fragment of $CF_2CH_2OH^+$ is originating from the hydroxyl end groups and deeply related with the chemical bonding to the carbon overcoats, as shown in Fig.5.0.0.

Here it should be pointed out that the normalized intensity of $CF_2CH_2OH^+$ is varied with molecular weights [4], as shown in Fig.5.6. This is because the increase of M_n will lead to an increase of the backbone fragments in intensity. Considering the dependence of $CF_2CH_2OH^+/C_2F_4^+$ on M_n, the limited samples of the lubricant A (M_n = 1800) is shown in Fig.5.7. It is observed that the highly annealed and the solvent-washed samples show the lower intensity of $CF_2CH_2OH^+$. They were considered to be almost chemically bonded through the treatments. For example, the typical chemical bondability estimated from the remaining thickness measured by FTIR after the solvent washing was 20% for not annealed, 43% for normally annealed, 74% for 150 degree C-annealed and 100% for 200 degree C-annealed samples, respectively (see Fig.5.0.5). Fig.5.8 shows the relationship between the bonding ratio measured by FTIR and the normalized intensity of $CF_2CH_2OH^+$ expected at $CF_3^+/C_2F_5^+$ = 0.4. The expected values of $CF_2CH_2OH^+/C_2F_4^+$ were estimated from Fig.5.7. It is clearly shown that the estimated $CF_2CH_2OH^+$ intensity decreases as the bonding ratio increases.

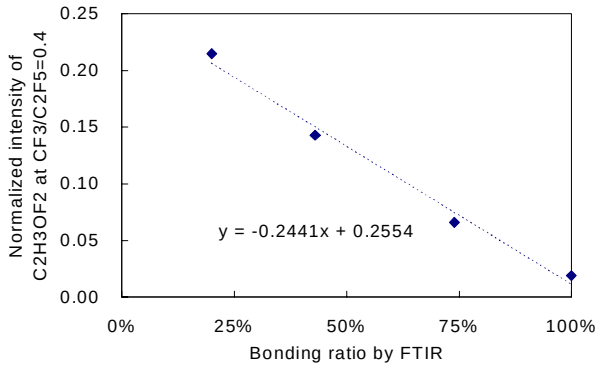

Fig. 5.8. Relationship between the normalized intensity of $CF_2CH_2OH^+$ expected at $CF_3^+/C_2F_5^+$ =0.4 and the bonding ratio by FTIR.

In contrast with the increase of chemical bondability, the $CF_2CH_2OH^+/C_2F_4^+$ ratio is suppressed, meaning that the chemical bonding between the lubricant and carbon overcoat surface causes the decrease of fragmentation probability from the hydroxyl end groups. Thus the chemical structure of lubricant films such as chemical bondability can be examined using this plot.

It is the first report describing that the ionization probability from the functional end groups concerned with the chemical bonding strongly depends on the chemical interaction between the organic molecules and the substrate atoms.

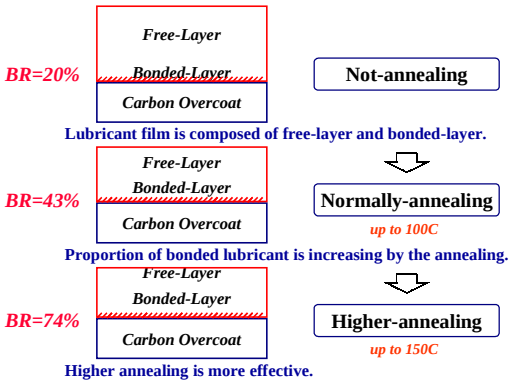

Fig. 5.0.5. Schematic representation of changes in the bonding ratio of the Fomblin Z-DOL films on carbon overcoat.

5.1.4. Conclusions

Based on the results obtained, it is concluded that some useful information on chemical structure of Z-DOL films can be extracted from the careful analysis of the relative intensity of key fragment ions on the ToF-SIMS spectra.

Most interesting result is that the ionization probability from the bonding sites is characteristically reduced by the chemical interaction. Thus, the intensity of characteristic peaks originating from the bonding sites can be used as an index of the chemical bondability.

References

[1] T. J. Schuerlein, C. A. Evans and P. M. Lindley, Proc. SIMS XI, 615 (Wiley, 1998).
[2] L. J. Huang, Y. Hung and S. Chan, Proc. SIMS XI, 563 (Wiley, 1998).
[3] L. J. Huang, Y. Hung and S. Chang, IEEE Trans. Magn., 33, 4551 (1997).
[4] J. G. Newman and K. V. Viswanathan, J. Vac. Sci. Technol. A, 8, 2388 (1990).
[5] P. H. Kasai and A. M. Spool, J. Phys. Chem. B, 102, 7331 (1998).
[6] A. M. Spool and P. H. Kasai, Macromolecules, 29, 1691 (1996).
[7] K. Merchant, P. Mee, M. Smallen and S. Smith, IEEE Trans. Magn., 26, 2688 (1990).
[8] H. J. Lee, R. Zubeck and D. Hollars, J. Vac. Sci. Technol. A, 11, 711 (1993).
[9] V. J. Novotny, X. Pan and C. S. Bhatia, J. Vac. Sci. Technol. A, 12, 2879 (1994).
[10] T. Hoshi, M. Tozu, R. Oiwa and L. Zhanping, Appl. Surf. Sci., 121/122, 146 (1997).
[11] A. Benninghoven, Surf. Sci., 299/300, 246 (1994).
[12] D. Johnson, A. J. Paul, P. Humphrey, N. M. Reed and J. C. Vickerman, Proc. SIMS VII, 911 (Wiley, 1990).
[13] V. J. Novotny, I. Hussla, J. M. Turlet and M. Philpott, J. Chem. Phys., 90, 5861 (1989).
[14] M. F. Tony and C. M. Mate, IEEE Trans. Magn., 34, 1774 (1998).
[15] D. Briggs and M. J. Hearn, Vacuum, 36, 1005 (1986).

5.2. Characterization of Molecular Ions from Fomblin Z-DOL on Ag Sustrate

Abstract

There is great difficulty in obtaining molecular ions from the lubricant films on magnetic recording disks. With the assistance of Ag cationization, quasi-molecular ions of $(Ag+M)^+$ from Fomblin Z-DOL cast on Ag substrate were successfully observed on the positive ToF-SIMS spectra. Considering the mass interference between oligomers, detailed distributions of molecular weight (M_n) and monomer ratio (*m/n*) could be extracted. The average values of M_n and *m/n* obtained by ToF-SIMS are in good agreement with those obtained by other conventional techniques such as NMR, and thus ToF-SIMS is proved to have enough potential to characterize lubricant film.

5.2.1. Introduction

In magnetic recording media, surface lubrication is essential to avoid catastrophic wear and consequent signal loss. PFPEs are currently the lubricant of choice for magnetic disks. One of the commercially available and most-often used PFPEs is Fomblin Z with hydroxyl end groups (Z-DOL).

Lubricant properties of films on disks are important parameters for assuring proper functionality of the magnetic disks. ToF-SIMS is a suitable technique for analysis of lubricant properties because of high surface sensitivity, a wide mass range, high mass resolution, and high lateral resolution [1]. The chemical structure of Fomblin Z-DOL films has been thus studied by ToF-SIMS [2] as mentioned in previous section 5.1, where a detailed analysis of relative intensities among typical fragment ions originated from Z-DOL are related with some useful lubricant properties, such as thickness, average molecular weight, average monomer ratio, bonding ratio to the carbon surface and so on. But there is still great difficulty in obtaining molecular ions from the lubricant films on actual disks.

In this section 5.2, I have tried to get more direct information from ToF-SIMS with the assistance of Ag cationization [3-5]. Ag cationization method is known to be very useful for detection of heavy oligomer ions as cluster ions formed between Ag and oligomer. Here, the first application of this method to the Fomblin Z-DOL, which is the most important lubricant for magnetic recording media is reported.

5.2.2. Experimental

Materials

Lubricants of Fomblin Z-DOL with different molecular weight were purchased from Ausimont, Italy. Their number-average molecular weight (M_n) ranged from 1900 amu to 5900 amu, and monomer ratio between ethylene and methylene units of the Fomblin backbone, *m/n*, ranged from 0.94 to 1.1, measured by NMR. For Ag cationization, tested lubricants were dissolved in fluorocarbon solvent at the concentration of 0.7 g/L and drops were cast onto the Ag substrate. Prior to the sample deposition, the Ag substrate was etched using nitric acid. After the several acid-treatment, the Ag surface was significantly roughened.

Measurements

ToF-SIMS measurements were performed in ION-TOF, TOF-SIMS IV apparatus. Ga liquid metal ion gun operating at energy of 25 keV, current of 0.33 pA, bunched pulse width of 0.7 ns, pulse frequency of 3.3 kHz was used as a primary ion source. Positive secondary ions were acquired within 2 min from the raster area of 305 x 305 μm^2. Under these conditions, total primary ion dose was 2.3 x 10^{11} ions/cm^2, which is under static limit, and

mass resolution of m/Δm was achieved over 10000 at *m/z* 81 ($CF_2CH_2OH^+$, characteristic of Z-DOL).

5.2.3. Results and Discussion

Large area imaging

Prior to mass spectrum acquisition, large area imaging by use of stage raster was performed in order to check the uniformity of the lubricant film cast on Ag substrate.

Fig.5.10 shows a typical secondary ion images of Ag_7^+ from the substrate, $(Ag+M)^+$ from the lubricant, and total ions, obtained from the stage raster area of 8 x 8 mm^2. It can be seen the half of oval area is covered with Z-DOL. Mass spectra extracted from the selected areas in covered and uncovered regions are also shown in Fig.5.10. Many peaks arising from the lubricant film were observed over *m/z* 1000, which were characteristic of the covered region. Although some features due to the surface roughness were observed, the obtained $(Ag+M)^+$ image showed almost constant distribution in intensity within the covered region and ensured the uniformity of the film thickness. Thus the mass spectrum acquisition could be performed without special attention to the sampling position.

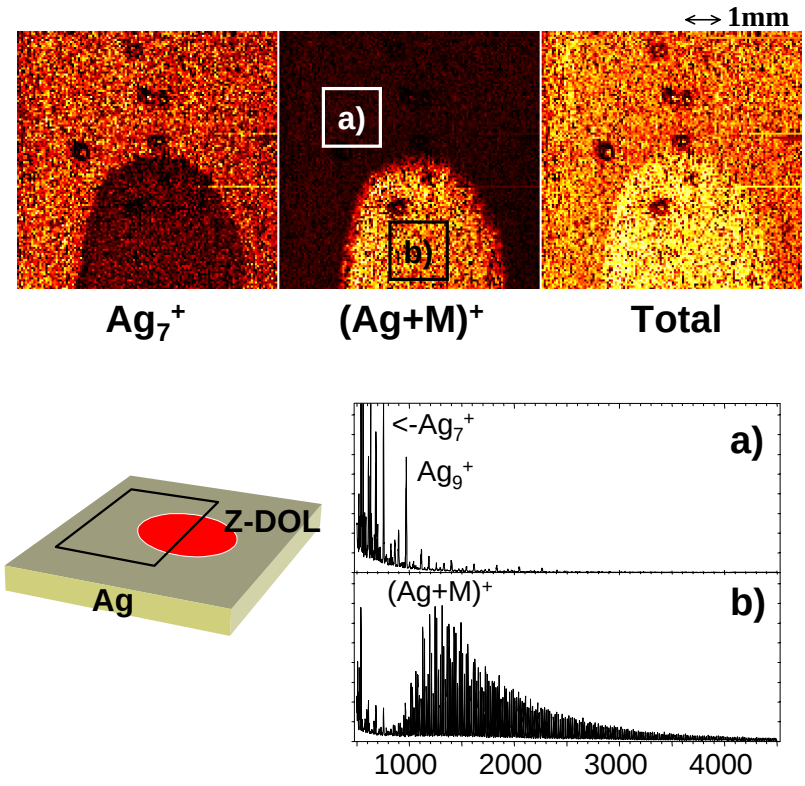

Fig. 5.10. Positive secondary ion images of Ag^+, $(Ag+M)^+$ and total ions obtained from Z-DOL 2000 cast on Ag substrate (top); field view of 8 x 8 mm^2.
Schematic view of sampling area is also shown (lower left).
Mass spectra extracted from selected areas a) and b) indicated in the image (lower right).

Analysis of molecular ions

Fig.5.11 shows positive ToF-SIMS spectra obtained from the various lubricants cast on Ag substrate. The sampling areas were almost center of the drops. On the spectra, many peaks were observed in oligomer region in accordance with each molecular weight. Line shapes composed of many oligomer peaks were different from each other, which were supposed to be related with the differences of molecular weight distribution.

Ag is believed to act as a catalyst in the ionization process of oligomer but the detailed mechanism is still in dispute. Fig.5.11 is the first observation of the molecular ions from Fomblin Z-DOL, which is enabled by the interaction between organic molecules and substrate Ag atoms.

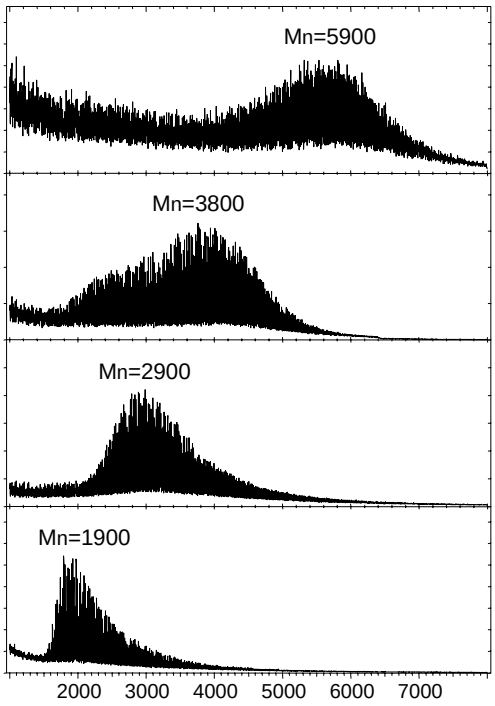

Fig. 5.11. Positive ToF-SIMS spectra of Fomblin Z-DOL with various molecular weight cast on Ag.

In this section, the spectrum obtained from Z-DOL 2000 with M_n = 1900 will be discussed in detail. Overview and interested parts of its spectrum are shown in Fig.5.12. Typical fragments originated from Fomblin backbone were dominantly observed in the mass range of *m/z* 0-200 (Fig.5.12(b)), in agreement with previous work [2]. In the higher mass range, quasi-molecular ions of $(Ag+M)^+$ were clearly observed, as expected, around *m/z* 2000 (Fig.5.12(c)). Other quasi-molecular ions such as $(M+H)^+$, $(M-H)^+$, $(M-OH)^+$ or $(Ag+M_2)^+$, $(Ag_2+M)^+$ were not observed. Oligomer peaks in this region appeared at typical interval of 16 amu (Fig.5.12(d)), due to the wide distribution of repeat number, *m* and *n*. Because the ethylene and methylene units have 116 amu and 66 amu, respectively, Δm = -1 and Δn = +2 lead to Δmass = +16.

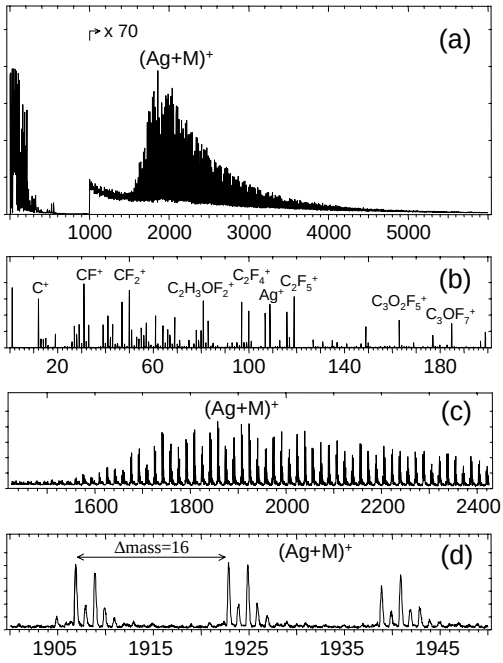

Fig. 5.12. Positive ToF-SIMS spectrum of Fomblin Z-DOL 2000 cast on Ag substrate.

Fig.5.13 shows typical peaks of $(Ag+M)^+$ expected for <m = 10, n = 6> (a) and <m = n = 9> (b), and the calculated isotope ratio for <m = n = 9> (c). While the peaks in (b) have the almost same relative intensities as the calculation, the peaks in (a) have an additional component, noticed by " * ". This additional component could be attributed to the mass interference between two oligomers with different repeat number, because Δm = -4 and

Δn = +7 led to Δmass = -2. Thus data treatments for separation of the mass interference should be taken into consideration in the case of severe overlapping.

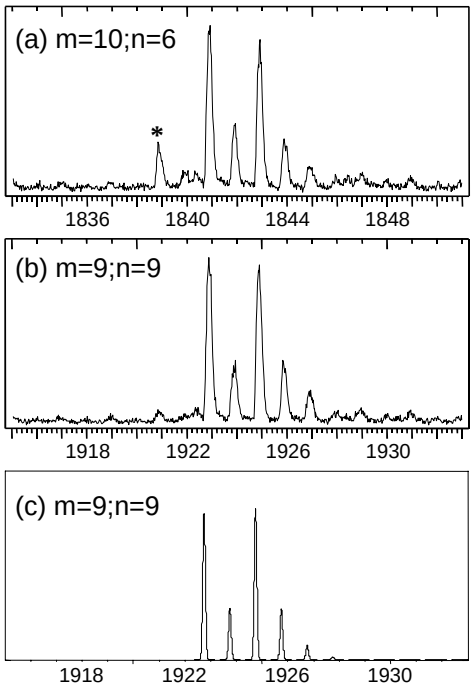

Fig. 5.13. Typical peaks of $(Ag+M)^+$ expected for (a) m=10, n=6; (b) m=n=9. Calculated isotope ratio for m=n=9 is also shown in (c).

Distribution of molecular weight and monomer ratio

Considering the mass interference mentioned above, it could be easy to obtain the peak intensity of selected oligomer ion with repeat number <m, n>, using following chemical formula:

$C_2H_3OF_2O(C_2F_4O)_m(CF_2O)_nC_2H_3O\ F_2$+Ag
= $C_{2m+n+4}H_6O_{m+n+3}F_{4m+2n+4}$Ag.

For example, typical peaks of $(Ag+M)^+$ among the series of m = 9 and n = 5-14 are shown in Fig.5.14. In this way, detailed distribution of both molecular weight and monomer ratio was successfully extracted from the intensity variation of $(Ag+M)^+$.

The variation in intensity among 70 peaks in the series of m = 7-12 is shown in Fig.5.15 as a function of mass (m/z) and m/n. The distribution width tended to be broader with increasing m.

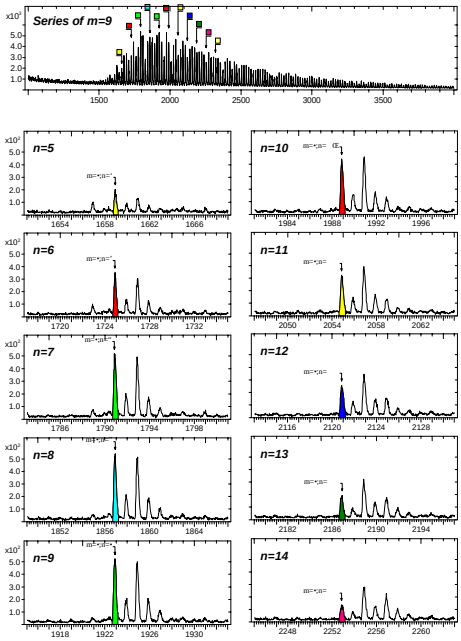

Fig. 5.14. Typical peaks of $(Ag+M)^+$ among the series of m=9 and n=5-14.

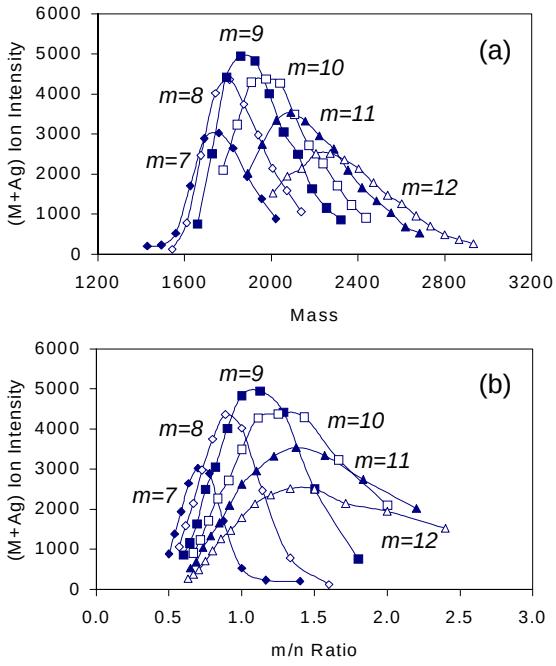

Fig. 5.15. Intensity variation of $(Ag+M)^+$ among the series of m=7-12 as a function of (a) m/z and (b) monomer ratio.

Lubricant properties of M_n and m/n could be calculated from the peak intensities of $(Ag+M)^+$ as follows [4]:

$$M_n = \Sigma I_{i,j} M_{i,j} / \Sigma I_{i,j},$$
$$m/n = \Sigma R_{i,j} M_{i,j} / \Sigma I_{i,j},$$

where $I_{i,j}$ = integral counts for the oligomer ion with repeat number <i, j>, $M_{i,j}$ = mass of the oligomer with <i, j>, and $R_{i,j}$ = monomer ratio of the oligomer with <i, j>. Dominant 54 peaks over 1000 counts, expected for <*m*, *n*> = <7, 8-13>, <8, 7-14>, <9, 6-14>, <10, 5-14>, <11, 5-15> and <12, 5-14>, were used for calculation. Determined M_n and *m/n* for Fomblin Z-DOL 2000 are summarized in Table 5.4. In conclusion, the average values obtained by ToF-SIMS are in good agreement with NMR, ensuring the data analysis described above.

Table 5.4. Comparison of lubricant properties obtained by NMR and ToF-SIMS.

Properties	NMR	ToF-SIMS
Number-average molecular weight	1.9×10^3	1.9×10^3
Monomer ratio of *m/n*	1.1	1.1

5.2.4. Conclusions

With the assistance of Ag cationization, the quasi-molecular ions of $(Ag+M)^+$ from Fomblin Z-DOL cast on Ag substrate was successfully detected. According to the data analysis of intensity variation in $(Ag+M)^+$, not only the average values of both molecular weight and monomer ratio, which are consistent with NMR, but also the detailed distribution of them were obtained. It is proved that ToF-SIMS has enough potential to characterize a lubricant film when it cast on the Ag substrate.

References

[1] A. Benninghoven, Angew. Chem. Int. Ed. Engl., 33, 1023 (1994).

[2] Y. Abe, M. Shibayama and T. Matsuo, Surf. Interface Anal., 30, 632 (2000).

[3] I.V. Bletsos, D.M. Hercules, D. vanLeyen and A. Benninghoven, Macromolecules, 20, 407 (1987).

[4] D. van Leyen, B. Hagenhoff, E. Niehuis, A. Benninghoven, I.V. Bletss and D.M. Hercules, J. Vac. Sci. Technol., A7, 1790 (1989).

[5] I.V. Bletsos, D.M. Hercules, D. Fowler, D. vanLeyen and A. Benninghoven, Anal. Chem., 62, 1275 (1990).

5.3. Characterization of Micro-corrosion on Magnetic Recording Disks by ToF-SIMS and AAS

Abstract

In order to qualify thin carbon overcoats (ranged from 5-11nm) on magnetic recording disks, the Co micro-corrosion from the magnetic layer to the surface after the stressed corrosion test (at 85 degree C and 80% RH for 4 days) has been studied by ToF-SIMS. Analysis of water-extracted Co with AAS was also performed to check the results obtained by ToF-SIMS. Whereas the almost linear correlation of these two measurements can be obtained from the overcoats above 7 nm, the Co intensity detected by ToF-SIMS is much higher than the Co amount detected by AAS from the overcoat of 5 nm. According to the dependency upon the beam energy, it is clearly shown that the relative intensity of Co can be varied with primary beam energy, and the lower energy (less than 7 keV) should be recommended in the case of Co migration analysis of thinly overcoated (below 7 nm) disks. Based on the results obtained, it is found that if the beam energy used is too high or the overcoat is too thin, Co from the magnetic layer may be detected through the thin overcoat film by ToF-SIMS.

5.3.1. Introduction

Carbon overcoats are widely used for magnetic recording disks as a protective layer against wear and corrosion from interaction at the head-disk interface (HDI). With the requirement of higher data storage capacity, the thin-film media industry has recently focused on developing a thinner overcoat with better wear and corrosion resistivity.

Corrosion of the thin film disks under environmental conditions is believed to be an electrochemical process, which requires the presence of water on the surface [1,2]. Schematic view of micro-corrosion mechanism is shown in Fig.5.16. In order to qualify thinner overcoats, corrosion test stressed under high temperature and high humidity is frequently used to examine whether the migration of cobalt from the magnetic layer to the surface has occurred or not. It is well known that the corrosion stress leads to selective migration of Co from the magnetic layer which is dependent on disk overcoat composition and structure [5].

ToF-SIMS is a suitable technique for Co migration analysis because of extremely high surface sensitivity and high lateral resolution [3,4]. In this section 5.3, the characterization of Co migrated to the surface is performed using ToF-SIMS as well as with atomic absorption spectrometry (AAS), which is a technique with good quantification and poor lateral resolution.

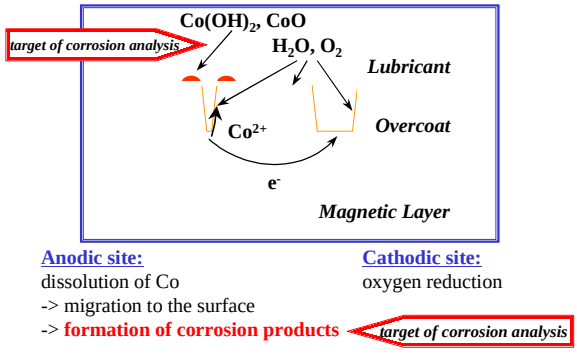

Fig. 5.16. Schematic view of micro-corrosion mechanism on the magnetic recording disk.

5.3.2. Experimental

Materials

The thin film disks used had a 1.2 nm lubricant layer and a different carbon overcoat above a magnetic layer of 25 nm CoCrTaPt alloy. Below the magnetic layer, an underlayer of 40 nm Cr was underlying on a NiP-plated Al substrate. The lubricant was Fomblin Z-DOL.

The lubricant thickness was measured by FTIR [12] and/or XPS [13]. The overcoats were hydrogenated carbon prepared by chemical vapor deposition (CVD) or DC magnetron sputter, and their thickness was ranged from 5 nm to 11 nm (tabulated in Table 5.5). Thickness of overcoats was estimated by EPMA calibrated by TEM. Samples of B-E or F-G with the same preparation and the same thickness were deposited under various conditions, respectively, which probably led to the different carbon density or hydrogen content on the analogy of other measurements by hydrogen forward scattering spectrometry - Rutherford back scattering spectrometry (HFS-RBS).

Table 5.5. Carbon overcoats of tested samples.

Sample name	Preparation	Thickness (nm)
A*1	CVD	5
B*1	CVD	7.5
C*1	CVD	7.5
D*1	CVD	7.5
E*1	CVD	7.5
F*2	Sputter	11
G*2	Sputter	11

*1 Carbon density of CVD samples may be varied as follows: A and B > C > D > E.

*2 Hydrogen content of sputtered samples may be varied as follows: F > G.

The disks then subjected to high temperature (85 degree C) and high humidity (80% RH) in a humidity chamber for 4 days. The ramp up rate of the temperature and humidity was kept minimum to avoid possible water condensation on the disk surface.

Measurements

ToF-SIMS was performed in a PHI TRIFT II system with a pulsed Ga liquid metal ion gun operating at various energies of 2, 7, 12 and 22 keV. In this system, the "beam-energy dependent" experiments were performed. The beam current was set to 600 pA DC and the typical beam raster size was 40μm x 40μm. The sample holder was biased with a 3 kV positive voltage at the acquisition of positive ions. Positive ToF-SIMS spectra and images were obtained from the disks after the stressed corrosion test (at 85 degree C and 80% RH for 4 days).

AAS analysis of Co cation dissolved in water was also performed to check the results obtained by ToF-SIMS. For the AAS measurements, the tested disks were steeped in water for 30 minutes at room temperature in order to extract the corrosion products on the surface. Before the stressed corrosion test, Co was not detected from all the samples by AAS.

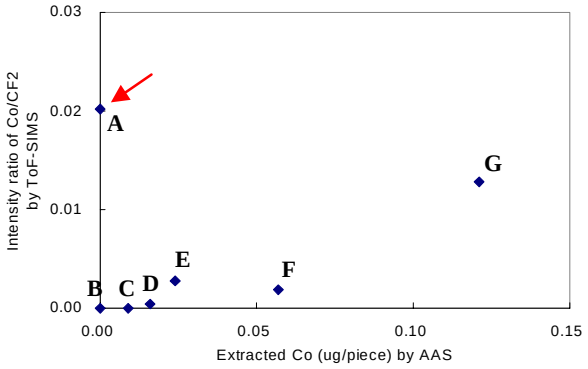

Fig. 5.17. Relationship between ToF-SIMS and AAS.

5.3.3. Results and Discussion

On the ToF-SIMS spectra obtained by 7 keV beam, the $C_xF_y^+$ type of fragments originating from the backbone of lubricant were dominated as previously reported [7-9], and Co^+ peak was additionally observed at 58.93 atomic mass unit (amu) from the sample A, D, E, F and G. Fig.5.17 shows the relationship between the ratio of Co^+/CF_2^+ in intensity by ToF-SIMS and the Co amount detected by AAS. In the AAS measurements, the limit of quantification for Co was estimated to be 0.005 ug/piece, which corresponded to 4 x 10^{11} atoms/cm^2. On the ToF-SIMS spectra, intensity over 50 counts was regarded as a peak after the data acquisition for 3 minutes. At this conditions total primary ion dose was estimated to be 8 x 10^{12} ions/cm^2, several times higher

than the generally accepted static limit [10], in order to ensure whether the Co^+ peak was present or not on the spectrum.

The almost linear correlation of these two measurements is obtained except sample A (noticed by an arrow in Fig.5.17), which has the thinnest overcoat of 5 nm. In the case of sample A, the Co^+ intensity obtained by ToF-SIMS is much higher than AAS.

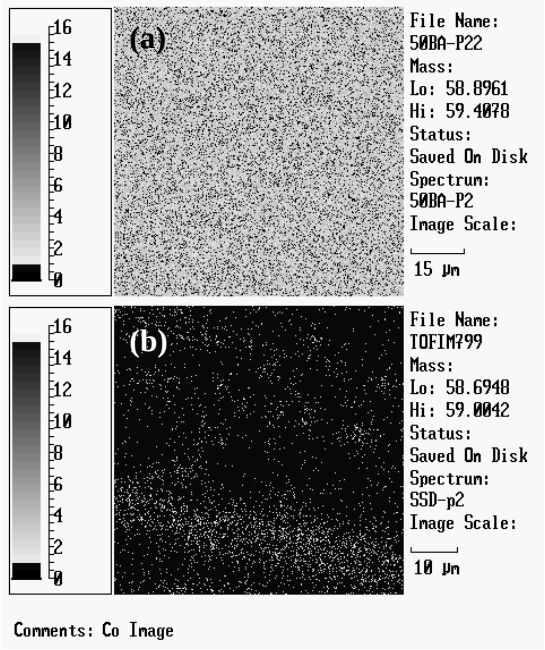

Fig. 5.18. Positive ToF-SIMS images of Co from the sample of (a) A and (b) G, respectively, obtained by 22keV beam.

The ToF-SIMS imaging of sample A also shows some different behavior from those of other samples. Figs.5.18(a) and (b) show the Co^+ distribution from the sample A and G, respectively, obtained by 22 keV beam. The lateral resolution was less than 1μm. The Co^+ distribution of sample G correlates with the texture lines in agreement with previous works [5,6], while an uniform coverage is only observed from the sample A. There is no sign of Co corrosion on the sample A from the ToF-SIMS imaging, because characteristic distribution arising from heterogeneous corrosion products was not observed on the surface. For example, some typical distributions of Co^+ on the other samples, where the micro-corrosion unambiguously occurred, are shown in Fig.5.19. Figs.5.19(a) and (b) show the Co^+ images obtained from the different samples with/without texturing. Corrosion tends to occur along the texture lines shown in Fig.5.19(b). Figs.5.19(c) and (d) show the Co^+ images obtained from the same sample by the different beam energy of 12 keV and 22 keV. These results clearly show the differences of Co^+ distribution according to the beam energy.

To understand the difference between the sample A and others, the dependency of the Co^+ intensity upon the primary beam energy was examined. Fig.5.20 shows the positive ToF-SIMS spectra obtained by 2, 7, 12 and 22 keV beam, respectively, from the sample A. In this system, an incidence angle becomes near normal as the primary beam energy increases (for example, 75 degree for 2 keV, 45 degree for 7 keV, 41 degree for 12 keV, and 38 degree for 22 keV [11]). The mass resolution of $m/\Delta m$ for Co^+ was over 7000 at 2, 7, 12 keV or about 3000 at 22 keV. Fig.5.21 shows the normalized intensity of CF^+, $C_2F_4^+$ and Co^+ (shown in Fig.5.20) against the beam energy. All intensities shown in Fig.5.21 are normalized to the CF_2^+ intensity of each spectrum. Whereas the relative intensities of CF^+ and $C_2F_4^+$, originating from the lubricant, are almost independent on primary beam energy in agreement with previous work [11], the relative intensity of Co^+ can be varied by the choice of primary beam energy.

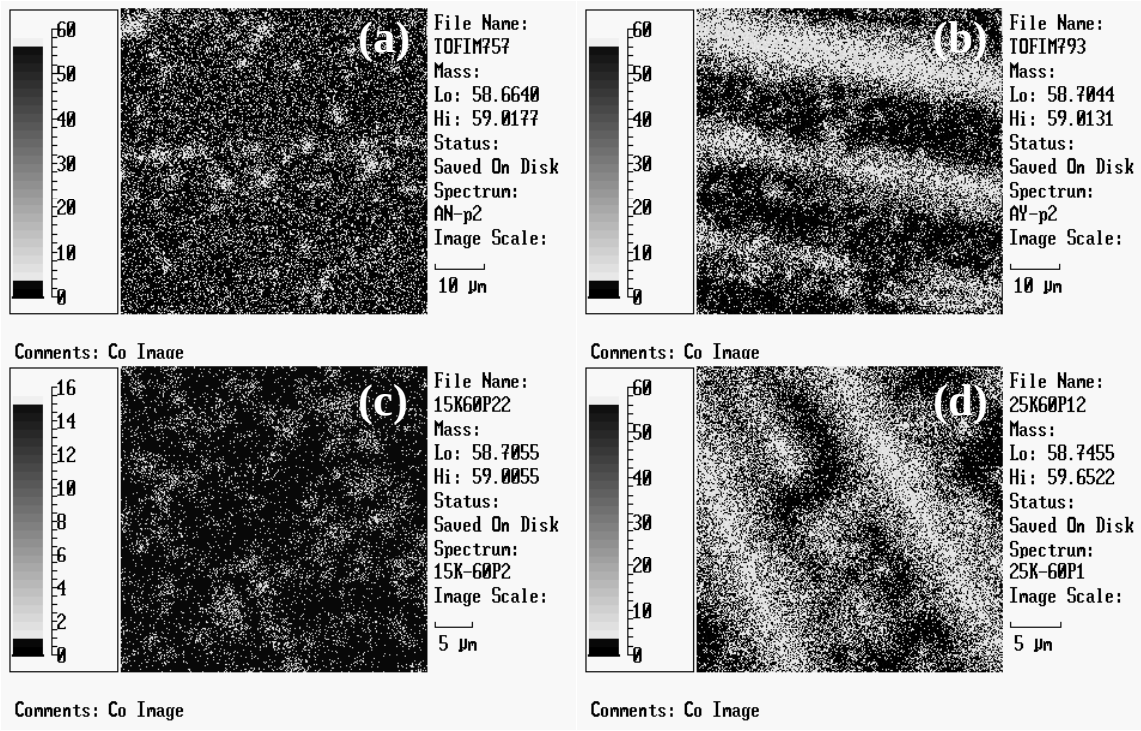

Fig. 5. 19. Some examples of Co images.
By 22 kev beam from the sample (a) without texturing and (b) with texturing.
From the same sample by different beam energy of (c) 12 keV and (d) 22 keV.

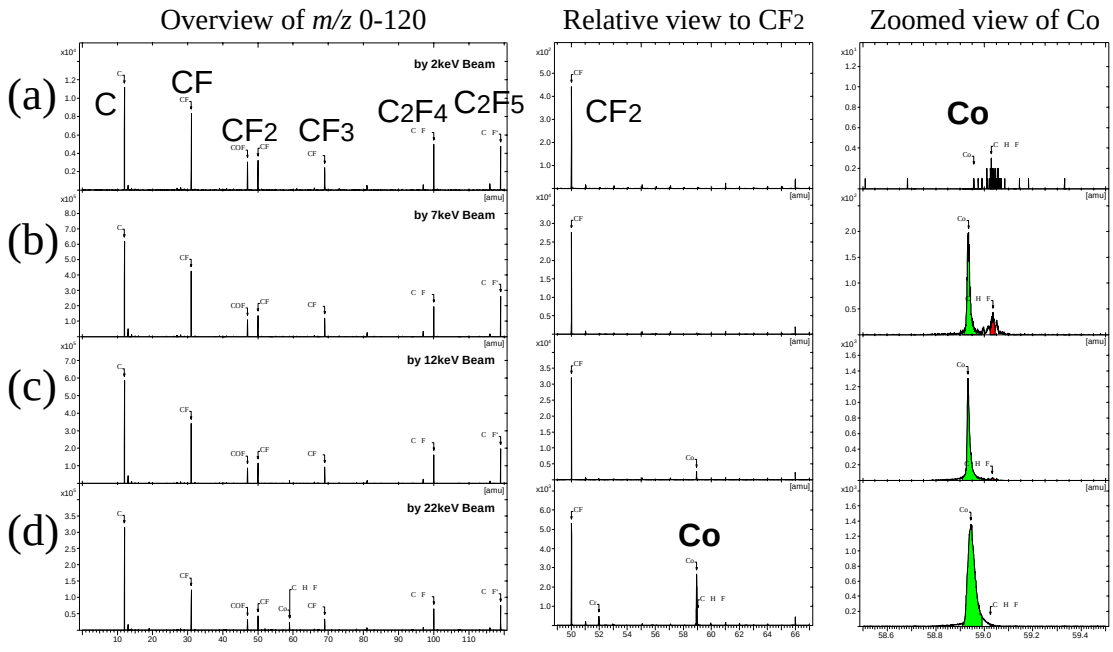

Fig. 5.20. Positive ToF-SIMS spectra from the sample A by (a) 2keV, (b) 7keV, (c) 12keV and (d) 22keV beam, respectively.
The region of Co^+ peak is zoomed from the left to the right.

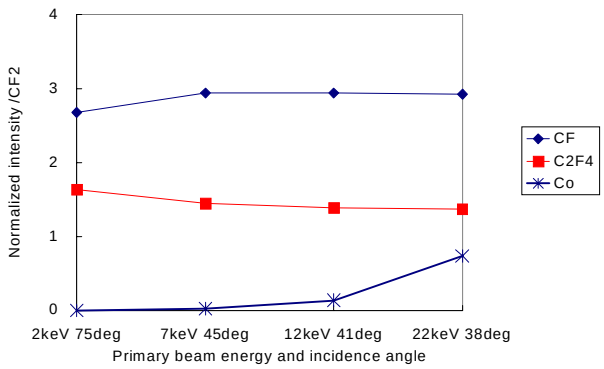

Fig. 5.21. Changes of normalized intensities as a function of primary beam energy and incidence angle.

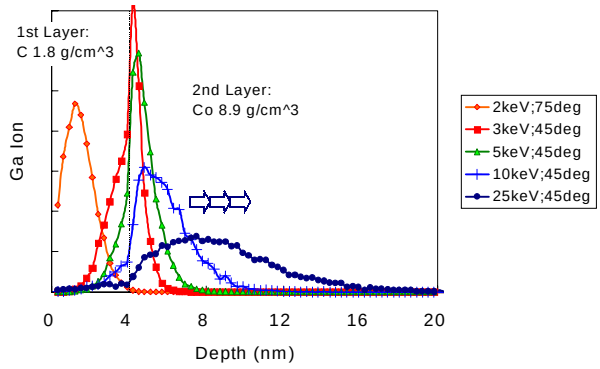

Fig. 5.22. TRIM simulation results. Ga ions of the several energy are injected to the sample of C 4 nm / Co 26 nm.

To confirm the change in information depth of Co^+ according to the beam energy, simulations with TRIM code [14] are performed. The results are shown in Fig.5.22 on the assumption that Ga primary ions are injected to the layer structure sample, whose 1st layer is composed of carbon and its density is 1.8 g/cm^3, and 2nd layer is composed of cobalt and its density is 8.9 g/cm^3. The distribution in depth of the injected Ga ions is representing. Use of the lower beam energy can effectively reduce the injection depth. But the lower beam energy below 10 keV has some disadvantages in mass resolution and spatial resolution. High-mass resolution and sufficient spatial resolution are essential to the ToF-SIMS applications. And it should be noticed that the injection depth does not define the information depth of ToF-SIMS. Further discussion will be held about the ToF-SIMS information depth in the following section 5.4.

5.3.4. Conclusions

Based on the results obtained, it is concluded that the relative intensity of Co^+ is strongly dependent on the primary beam energy and the lower energy should be recommended in the case of Co migration analysis of thinly overcoated (probably below 7 nm) disks. If the beam energy used is too high or the overcoat tested is too thin, Co from the magnetic layer may be detected through the thin overcoat film and some misjudgments may be extracted in the qualification of thin overcoats.

References

[1] V. Novotny and N. Staud, J. Electrochem. Soc., vol. 135, 2931 (1988).
[2] C. C. Wang, R. W. J. Chia, J. K. Lee and W. T. Tang, J. Vac. Sci. Technol. A, vol. 16, 1745 (1998).
[3] A. Benninghoven, Surf. Sci., vol. 299/300, 246 (1994).
[4] A. Benninghoven, Angew. Chem. Int. Ed. Engl., vol. 33, 1023 (1994).
[5] L. J. Huang, Y. Hung and S. Chang, IEEE Trans. Magn., vol. 33, 3154 (1997).
[6] T. J. Schuerlein, C. A. Evans and P. M. Lindley, Proc. SIMS XI, 615 (Wiley 1998).
[7] J. G. Newman and K. V. Viswanathan, J. Vac. Sci. Technol. A, vol. 8, 2388 (1990).
[8] P. H. Kasai and A. M. Spool, J. Phys. Chem. B, vol. 102, 7331 (1998).
[9] Y. Abe, M. Shibayama and T. Matsuo, Surf. Interface Anal., 30, 632 (2000).
[10] D. Briggs and M. J. Hearn, Vacuum, vol. 36, 1005 (1986).
[11] T. Hoshi, M. Tozu, R. Oiwa and L. Zhanping, Appl. Surf. Sci. vol. 121/122, 146 (1997).
[12] V. J. Novotny, I. Hussla, J.-M. Turlet and M. Philpott, J. Chem. Phys., vol. 90, 5861 (1989).
[13] M. F. Toney and C. M. Mate, IEEE Trans. Magn., vol. 34, 1774 (1998).
[14] J. F. Zieger, web site, http://www.srim.org/.

5.4. Estimation of ToF-SIMS Information Depth in Micro-corrosion Analysis

Abstract

In order to qualify the micro-corrosion analysis of magnetic recording disks by ToF-SIMS, the information depth of Co^+ is studied by measuring the depth profiles with dual-beam ToF-SIMS. On the carbon overcoat of 4 nm thickness, the Co^+ intensity originating from the underlying magnetic layer was estimated as 0.85% of Co^+ intensity at the interface, using λ = 0.84 nm for the analytical conditions used. It was not negligible because Co^+ intensity at the interface was significantly enhanced by the presence of the interfacial oxidation. Thus not only Co migrated to the surface but also Co contributed from the magnetic layer may be detected by ToF-SIMS in the case of thinly overcoated disks.

5.4.1. Introduction

In the previous section 5.3, the corrosion behavior of thinly overcoated disks is characterized by ToF-SIMS as well as with AAS, which is a technique with good quantification of Co cation dissolved in water. Almost linear correlation of these two measurements is obtained except for the sample overcoated below 5 nm, whose Co^+ intensity was much higher than AAS. According to the dependency of relative intensities upon the beam energy [5,6], it was clearly shown that the Co^+ peak increased relatively as the primary beam energy increased, resulting in the increase of contribution from the underlying layer.

In the previous investigation, one question: "How much Co^+ may be detected from the magnetic layer through the thin overcoat by ToF-SIMS?" emerged. To solve this issue comparative depth profiling by ToF-SIMS and AES has been tried in order to discuss the ToF-SIMS information depth.

5.4.2. Experimental

Materials

For depth profile analysis, a commercially available magnetic recording disk of high-grade was used. A carbon overcoat, a magnetic layer and an underlayer were deposited on NiP-plated Al substrate. On the overcoat, a lubricant film of Fomblin Z-DOL was coated with thickness below 1 nm. The magnetic layer was Co-base alloy, including Co above 60 at% and Cr above 15 at%. The overcoat thickness was estimated at 4 nm from the cross-sectional observation by TEM, shown in Fig.5.23.

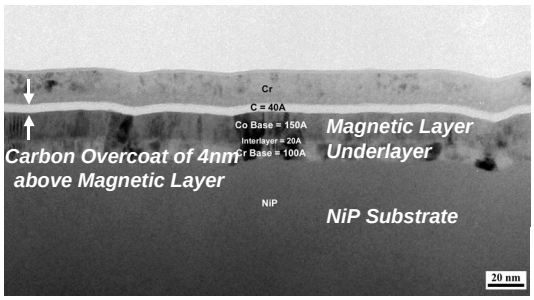

Fig. 5.23. Cross-sectional TEM image of the commercially available high-grade disk.

Measurements

ToF-SIMS measurements were performed in ION-TOF, TOF-SIMS IV apparatus. Ga liquid metal ion gun operating at energy of 25 keV, current of 2.4 pA, bunched pulse width of 0.7 ns was used as an analysis gun. Positive secondary ions were acquired with reflectron-type mass analyzer from the raster area of 100 x 100 μm^2. Ar ion gun operating at energy of 1 keV, current of 51 nA, incidence angle of 45 degree, raster area of 500 x 500 μm^2 was used as a sputter gun. In this system, ToF-SIMS depth profiling "with dual ion beam" can be performed in the following

cycles: sputtering by Ar^+ for 1 s, pause for 0.5 s and analysis by Ga^+ for 1 s. Depth profiling data were collected with / without oxygen flooding of 5 x 10^{-5} Pa.

AES measurements were performed in VG, Microlab 310-F apparatus. Field emission gun operating at energy of 10 keV, current of 8 nA was used. Auger electrons were acquired with CHA from the raster area of 10 x 10 μm^2 with detection angle of 30 degree. Ar ion gun operating at energy of 1 keV, current of 200 nA, incidence angle of 50 degree, raster area of 2 x 2 mm^2 was used as a sputter gun.

5.4.3. Results and Discussion

AES Depth Profiling

The summary of AES depth profiles is shown in Fig.5.24. In order to discuss the information depth over the magnetic layer, the abscissa in Fig.5.24 shows the sputter depth estimated from the sputtering rate of the overcoat. The variations in intensity of Auger electrons arising from C-KLL, Cr-LMM and Co-LMM transitions were observed from the overcoat to the magnetic layer. The lubricant film on the overcoat was completely disappeared after the electron irradiation and F was not detected on the AES spectra.

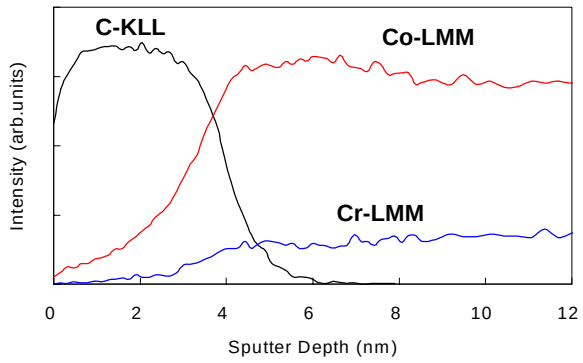

Fig. 5.24. Summary of AES depth profiles.

ToF-SIMS Depth Profiling

The summary of ToF-SIMS depth profiles in the same depth scale as that of Fig.5.24 is shown in Fig.5.25. Without oxygen flooding, the variations in intensity of positive secondary ions, CF^+ from the lubricant, C^+ from the overcoat, Co^+ and Cr^+ from the magnetic layer, were observed from the overcoat to the magnetic layer in Fig.5.25(a). The lubricant film was disappeared immediately after a few cycles of Ar sputter. At the interface between overcoat and magnetic layer, significant enhancement was observed in Co^+ and Cr^+ intensities. This enhancement could be attributed to the interfacial oxidation, because the depth profiles of cluster ions including oxygen, $Co_2H_2O^+$ and Co_3OH^+ shown in Fig.5.25(b), clearly revealed the presence of the interfacial oxidation.

Along with the interface, a characteristic increase of Co^+ intensity was observed at the outermost surface in Fig.5.25(a). In order to examine the origin of enhanced Co^+ intensity in near-surface region, depth profiling with oxygen flooding was also performed. Under oxygen flooding, CoO^+ and CrO^+ were additionally observed in the magnetic layer, shown in Fig.5.25(c). By comparison of the intensity ratio of CoO^+ / Co^+, shown in Fig.5.25(d) estimated from Fig.5.25(c), CoO^+ was not enhanced in near-surface region. This behavior could be accounted from the following reason. At first, in the region near the outermost surface the almost Co^+ peak was originated from Co oxide as some corrosion products migrated to the overcoat surface, and not affected by oxygen flooding. If Co was present as metallic, the intensity of CoO^+ should be enhanced by oxygen flooding as observed in the magnetic layer. Secondary, in the region just below the outermost surface Co was not present on the analyzing surface and the almost Co^+ peak was contributed from the magnetic layer. Thus origins of the Co^+ peak detected in the overcoat is considered as follows: some corrosion products migrated to the surface, which is the target of corrosion analysis; contribution from the magnetic layer, which should be excluded from the evaluation of corrosion resistance. In order to separate the

two origins, the information depth is estimated below.

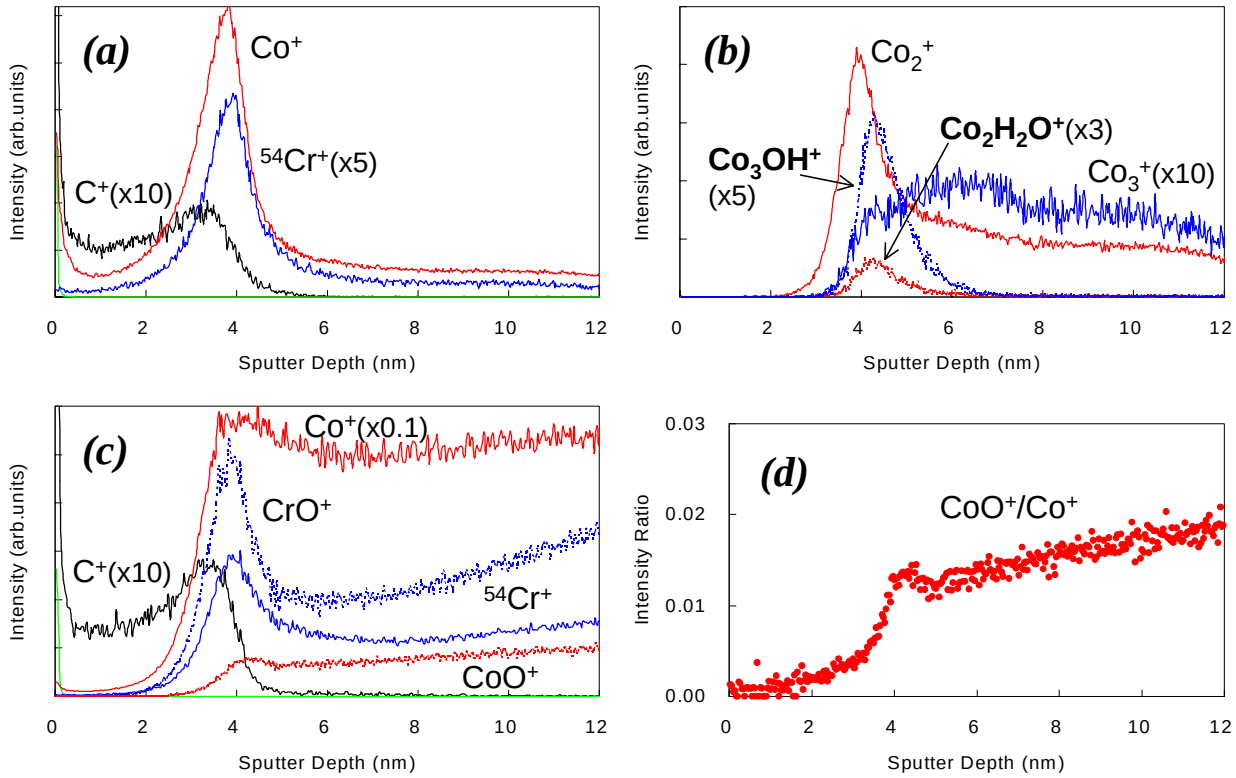

Fig. 5.25. Summary of ToF-SIMS depth profiles (a), (b) without O_2-flooding; (c), (d) with O_2-flooding.

Estimation of Information Depth

To estimate the information depth, following equation (1) was used [7].

$$I / I_0 = \exp(-d / \lambda), \qquad (1)$$

where I and I_0 are the intensities in the overcoat and in the magnetic layer, d is the residual overcoat thickness, λ is the information depth.

Typical fitting results of the depth profiles using eq. (1) are shown in Figs.5.26(a)-(c). The best fit values of λ are 1.42 nm for Co-LMM, 0.84 nm for Co^+ and 0.70 nm for Cr^+. The information depths in AES and SIMS are principally different because of their dependence on analyzing signal. In AES it can be selected with respect to different kinetic energy and detection angle of Auger electrons, while the information depth in SIMS is given by emission depth of secondary ions [7]. Thus the obtained λ for Co-LMM is including the geometrical factor of cos(30 deg) = 0.866. In normal emission, λ for Co-LMM is expected as 1.64 nm. The information depth of Co^+ by ToF-SIMS is almost half of Co-LMM by AES, but not shallow enough to avoid the contribution from underlying layer.

One may neglect the ToF-SIMS information depth on the analogy of D-SIMS, but there is an apparent difference in the information depth between ToF-SIMS and D-SIMS, depending on the primary ion beam energy. A lower energy, typically below 1 keV, ion beam is the current choice of D-SIMS in order to improve the depth resolution by reducing the range of atomic mixing and the information depth is regarded as zero. It should be emphasized that atomic ions detected by ToF-SIMS using high energy LMIG have the considerably larger information depth than D-SIMS.

Depth profiles of other cluster ions,

such as Cr_2^+, $CrCo^+$, Co_2^+, $CrCoO_2^+$, $Co_2H_2O^+$, Cr_3^+, $CrCo_2^+$, Co_3^+, Co_3OH^+, were also fitted by eq. (1). Results are summarized in Fig.5.26(d) as a function of *m/z*. Based on the results obtained the information depth of ToF-SIMS ranges from 0.2 nm to 0.8 nm, which depends on the size of cluster ions. It should be noted that in micro-corrosion analysis Co^+ has the largest value of information depth.

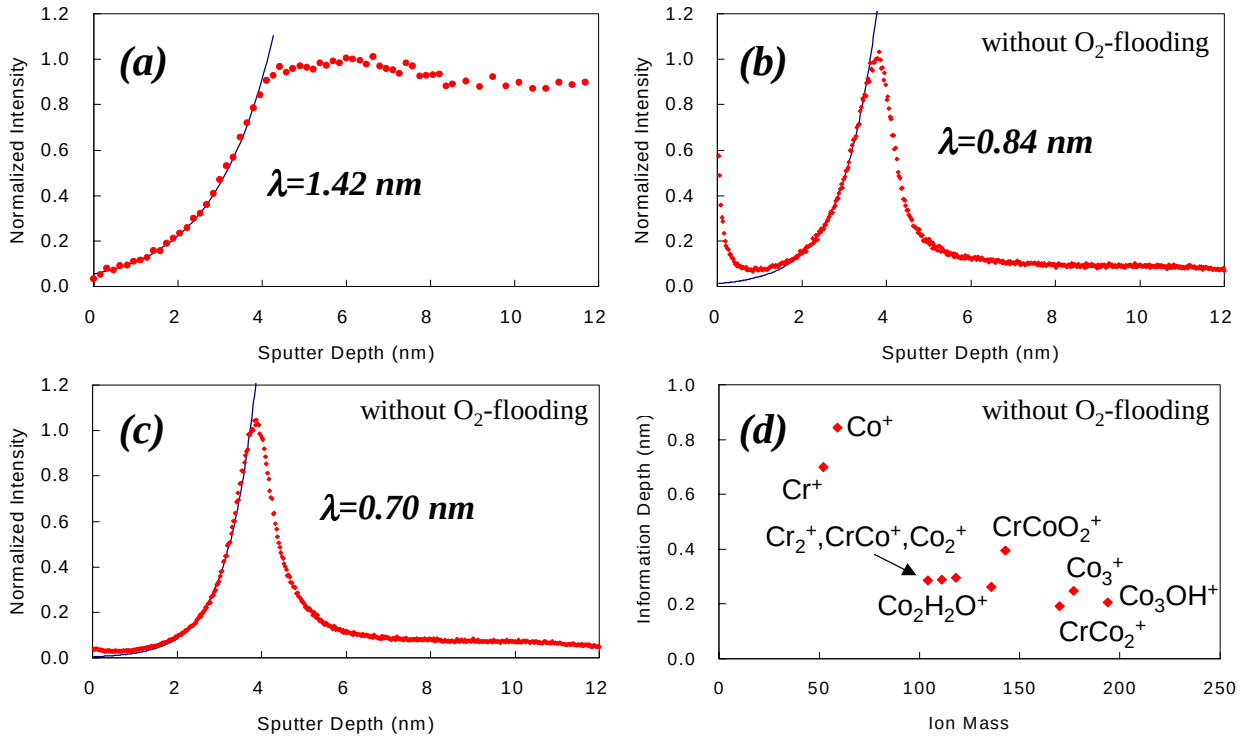

Fig. 5.26. Typical fitting results of depth profiles: (a) Co-LMM, (b) Co^+ and (c) Cr^+. Obtained information depth for secondary ions as a function of *m/z* (d).

5.4.4. Conclusions

In micro-corrosion analysis of the magnetic disk with 4nm-overcoat, Co^+ intensity contributed from the magnetic layer was estimated as $I = 0.0085*I_0$ using $\lambda = 0.84$ nm, where I was not negligible because I_0 was significantly enhanced by the presence of the interfacial oxidation. Thus not only Co migrated to the surface but also Co contributed from the magnetic layer may be detected by ToF-SIMS in the case of thinly overcoated disks.

References

[1] V. Novotny and N. Staud, J. Electrochem. Soc., 135, 2931 (1988).
[2] L.J. Huang, Y. Hung and S. Chang, IEEE Trans. Magn., 33, 3154 (1997).
[3] T.J. Schuerlein, C.A. Evans and P.M. Lindley, Proc. SIMS XI, Wiley & Sons, 615 (1998).
[4] C. Gao, Mat. Res. Innovations, 1, 238 (1998).
[5] Y. Abe, M. Shibayama, J. Sasahara and J. Kozu, J. Surf. Anal., 6, 148 (1999).
[6] T. Hoshi, M. Tozu, R. Oiwa, L. Zhanping and M. Kudo, Appl. Surf. Sci., 121/122, 146 (1997).
[7] S. Hofmann, J. Surf. Anal., 4, 9 (1998).

Chapter 6

Applications of ToF-SIMS to Nanocrystals Thin Films

In this chapter 6, the advanced use of ToF-SIMS to characterize the organic ligand capped CdSe nanocrystals is demonstrated as a result of comparable study with XPS. XPS can give quantitative information on both elemental and its chemical states. ToF-SIMS spectra are full of qualitative information on not only chemical states but also molecular structure, which can complement the XPS results. ToF-SIMS combined with XPS can provide a new perspective on the characterization of practical surfaces.

6. Investigation of Chemical Structure Changes in TOPO Capped CdSe Nanocrystals Thin Films by Comparable ToF-SIMS and XPS Study

Abstract

Comparable characterization of trioctylphosphine oxide (TOPO) capped CdSe nacocrystals by XPS and ToF-SIMS are demonstrated. Quantitative analysis of surface elemental composition and chemical state for CdSe nanocrystals surface was performed with XPS. Qualitative information about the surface complex formed on the CdSe was extracted from ToF-SIMS spectra. Based on the results obtained, the process of the photon-induced changes in TOPO capped CdSe surface was proposed as follows: In the initial state, organic ligand TOPO bound to Cd site on the CdSe surface, which was conformed by the detection of (TOPO+Cd) cluster ions. In the photo-brightening state, where photoluminescence (PL) intensity increased after some amount of illumination, a part of TOPO migrated from Cd site to Se site forming TOPO-Se complex. In the photo-darkening state, where the PL intensity gradually decreased after the photo-brightening, oxidation of surface Se and decomposition of TOPO-Se complex occurred, which was followed by the desorption of TOP and SeO_2 from the surface. It is proved that XPS and ToF-SIMS can be used for surface chemical structure analysis as complementary techniques.

6.1. Introduction

Chemically synthesized semiconductor nanocrystals (quantum dots) whose radii are smaller than the bulk exciton Bohr radius exhibit unique optical properties [1]. Quantum confinement of both the electron and hole in three dimensions leads to an increase in the effective band gap of the material with decreasing crystal size. Both the optical absorption and emission energies of quantum dots shift to the blue side (higher energy) as the size of the dots gets smaller, as shown in Fig.6.0 [3]. An example of the TEM image and a schematic diagram of CdSe nanocrystal are also shown in Fig.6.0.

The optical properties of CdSe nanocrystals are being extensively investigated [1-3]. It has been reported that the photoluminescence (PL) intensity of a thin film of CdSe is increased by some duration of UV light irradiation, and that further irradiation of UV light causes gradual decrease in PL intensity [2]. The state where the PL intensity is maximized is called a photo-brightening (PB) state, and the state where the PL intensity is decreased with further irradiation is called a photo-darkening (PD) state. These phenomena enable the invention of the luminescence-based optical memory media.

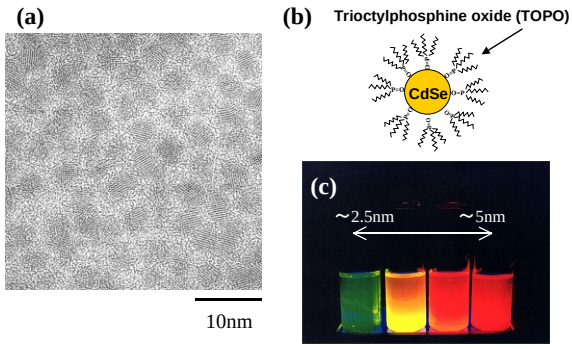

Fig. 6.0. (a) TEM image and (b) schematic diagram of CdSe nanocrystals. (c) The emission energy of the dots shifts to the blue side as the size of the dots gets smaller.

PL efficiency is deeply correlated with surface state of nanocrystals such as the degree of passivating surface nonradiative recombination sites or adsorption state of organic ligand. Recently the changes in surface states of CdSe nanocrystals before and after the irradiation of blue light have been investigated by XPS and ToF-SIMS [3]. In this section, it is demonstrated that the complementary information can be obtained on the changes in surface chemical structure of trioctylphosphine oxide (TOPO) capped CdSe nanocrystals by XPS and ToF-SIMS, and that the combination

of XPS and ToF-SIMS is a very powerful method for microscopic chemical analysis for surfaces.

6.2. Experimental

6.2.1. Materials

Synthesis of CdSe nanocrystals

TOPO capped CdSe nanocrystals used were prepared by the colloidal chemical method [1]. A mixture of dimethylcadmium and selenium, dissolved in tributhylphosphine (TBP), was rapidly injected into TOPO which was heated up to 300-350 degree C. The diameter of CdSe nanocrystals thus prepared was about 3.5 nm, which was conformed by transmission electron microscopy (TEM). The synthesized nanocrystals were dissolved in $CHCl_3$ and the solution was spun coat onto a Si wafer and dried in vacuum at room temperature.

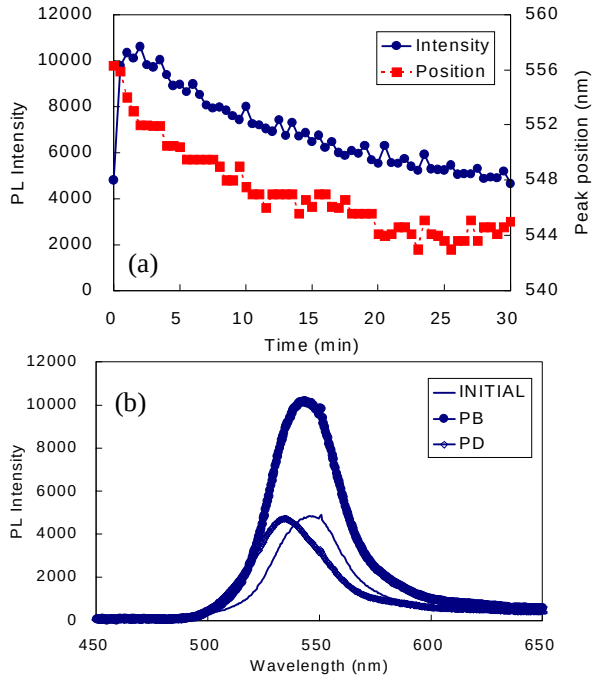

Fig. 6.1. (a) Variation in PL intensity and peak positions as a function of laser irradiation time. (b) PL spectra of CdSe nanocrystals thin film, in the initial, PB and PD states.

Optical properties

A fluorescence microscope equipped with an optical multichannel analyzer was used to measure the intensity of PL excited by He-Cd laser (442 nm), whose power density was about 1 W/cm^2. The PL inensity of CdSe nanocrystals is plotted as a function of He-Cd laser irradiation time in Fig.6.1(a). The PL intensity rapidly increased up to 1 min and decreased gradually for further irradiation. In this paper, the PB state and PD state were prepared by the irradiation of He-Cd laser light for 1 min and 30 min, respectively. In Fig.6.1(a), the peak position of PL spectra is also plotted, and a gradual blue shift of the peak with increasing irradiation time was clearly observed. Optical properties of the samples in the initial, PB and PD state are summarized in Fig.6.1(b).

6.2.2. Surface characterization

To investigate the change in surface states among initial, PB and PD states, AES, XPS and ToF-SIMS measurements were performed.

AES measurements

AES measurements were performed in the same system as that used in section 5.4. The energy resolution of ΔE/E was 0.5% for wide-scan spectra, 0.2% for narrow-scan spectra of Cd MNN and 0.1% for narrow-scan spectra of Se LMM. In this system, AES spectra with high-energy resolution can be obtained and directly compared with XPS spectra. In XPS spectra, both the peaks of photoelectrons and Auger electrons are observed, while electron-excited AES spectra provide the information on only Auger electrons. Thus, comparison of XPS and AES spectra allows us to extract only photoemission peaks from XPS data.

XPS measurements

A PHI Quantum 2000 system was used to perform XPS analysis. Photoelectrons and Auger electrons were excited by monochromated Al-Kα and detected with CHA. The X-ray tube was operated at 30 W. The pass energy of CHA was 187.35 eV for wide-scan spectra and 29.35 eV for narrow-scan spectra. The analyzing area on the specimen surface was

500 µm x 500 µm and the take-off angle was 45 degree. The binding energies of the spectra are calibrated by setting the C 1s peak maximum at 284.6 eV.

ToF-SIMS measurements

An ION-TOF TOF-SIMS IV system was used for ToF-SIMS measurements. Pulsed Ga ion gun operating at energy of 25 keV, current of 0.5 pA and pulse frequency of 5 kHz was rastered in 300 µm x 300 µm on the specimen surface. Positive or negative secondary ions were detected with reflectron-type mass spectrometer. The acquisition time to obtain a spectrum was typically 240 sec. Under these conditions, total primary ion dose was 8.3 x 10^{11} ions/cm^2, which is well below the static limit.

6.3. Results and discussion

6.3.1. Qualification of surface elements by AES and XPS

XPS and AES wide-scan spectra of the CdSe nanocrystals thin film in the initial state are shown in Fig.6.2.1. On both spectra, Auger transition lines of C KLL, O KLL, P KLL, Se LMM and Cd MNN are clearly observed and other lines of unexpected elements are not detected. In the XPS wide-scan spectra, there are many peaks arising from Se LMM Auger transitions in the kinetic energy range of 1000-1400 eV and peak interference between Se $L_2M_{45}M_{45}$ and P 2p occurs. Thus, P 2s spectra will be used to analyze the chemical state of P in the following section.

In order to demonstrate the high-energy resolution of the AES facility used in this work, narrow-scan spectra of Cd MNN and Se LMM are shown in Figs.6.2.2 and 6.2.3 together with XPS spectra. Here the pass energy was set at 29.35 eV for XPS and the energy resolution was 0.1-0.2% for AES, which reduces the pass energy of CHA to around 38 eV for Cd $M_4N_{45}N_{45}$ and 65 eV for Se $L_3M_{45}M_{45}$, respectively. The electron-excited AES spectra with high-energy resolution have similar line shapes as X-ray-excited spectra. Thus, AES can be used as a tool for chemical state analysis as well as XPS. However, since the electron excitation may cause the severe damage to organic molecules, XPS is used for detailed analysis in the following section.

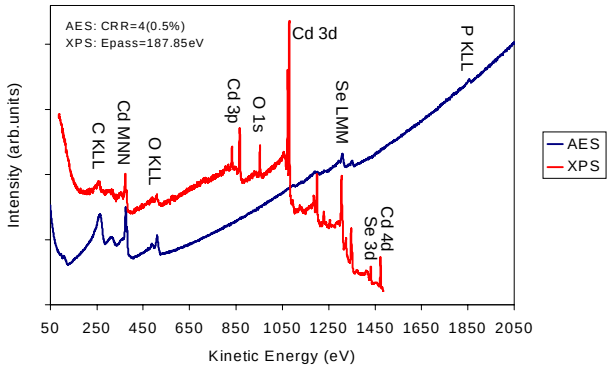

Fig. 6.2.1. AES and XPS wide-scan spectra from CdSe nanocrystals thin film, in initial state.

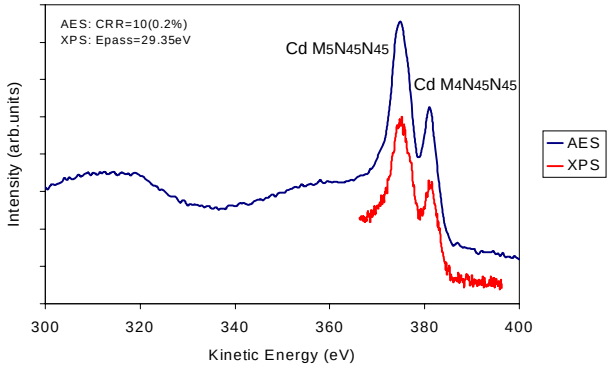

Fig. 6.2.2. AES and XPS narrow-scan spectra of Cd MNN from CdSe nanocrystals thin film, in initial state.

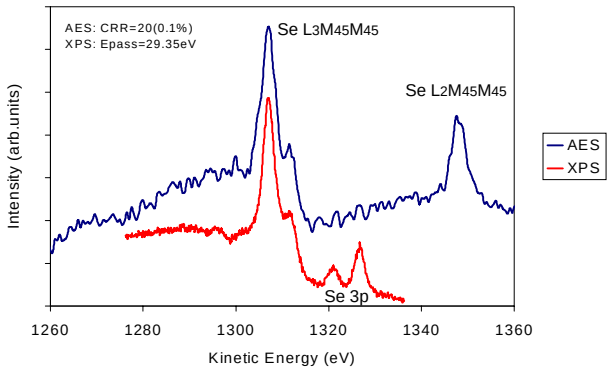

Fig. 6.2.3. AES and XPS narrow-scan spectra of Se LMM from CdSe nanocrystals thin film, in initial state.

6.3.2 Quantification of surface atomic composition and chemical state analysis by XPS

XPS narrow-scan spectra of C 1s, O 1s, P 2s, Se 3d and Cd 3d are shown in Fig.6.3. Auger lines of Cd MNN are also shown in order to examine the change in Cd Auger parameter. Surface atomic composition was evaluated by relative sensitivity factor method via the instrument quantification software, i.e. using the sensitivity factors and a transmission function corresponding to the measuring conditions, which are given by manufacturer. In Table 6.1, elemental composition of CdSe nanocrystals surface in the initial, PB and PD states are tabulated.

C, O and P

The C, O and P atoms are components of organic ligand TOPO. With increasing irradiation time, C and P decreased, whereas O increased. There was no sign of the change in chemical states of C, O and P, as shown in Fig.6.3. Decrease of C, P and increase of O are thought to be due to the fact that TOPO ligands are adsorbed on the CdSe surface with the O end, and the laser irradiation dissociates the P-O bond which leads to the desorption of TOP leaving the O atoms on the surface.

Table 6.1. Surface atomic composition (at%) of CdSe nanocrystals thin films.

Sample	C	O	P	Se	Cd
Initial	61.4	16.2	3.7	6.7	12.1
PB	58.4	19.6	2.8	6.5	12.7
PD	53.8	25.0	2.0	6.4	12.8

Cd and Se

Along with desorption of TOP, Se slightly decreased and Cd slightly increased. These changes lead to decrease of the atomic ratio of Se/Cd from 0.55 to 0.50. Whereas there was no significant change in Cd 3d and Cd MNN spectra, the line shapes in Se 3d drastically changed. With increasing irradiation time, the peak around 54 eV originating from Cd-Se decreased and Se oxide peak appeared around 59 eV. Proportion of Se oxide peak in Se 3d was estimated to be 4% in the initial state, 14% in the PB state and 42% in the PD state, respectively. In the PD state, almost half of Se was oxidized.

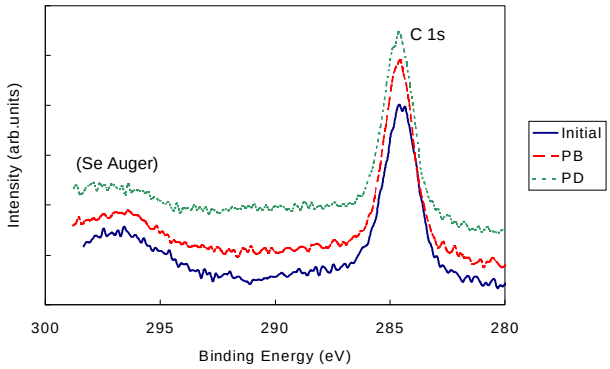

Fig. 6.3.1. XPS narrow-scan spectra of C 1s from CdSe nanocrystals thin films, in initial, PB and PD states.

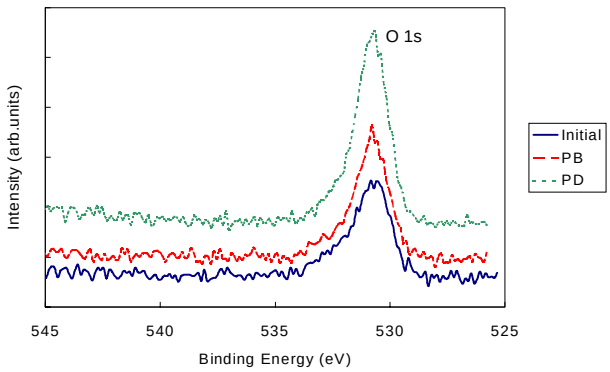

Fig. 6.3.2. XPS narrow-scan spectra of O 1s from CdSe nanocrystals thin films, in initial, PB and PD states.

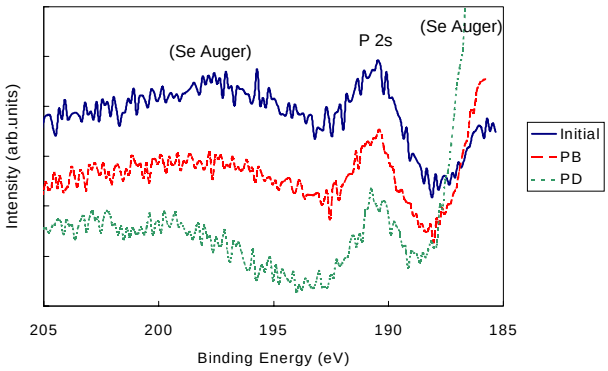

Fig. 6.3.3. XPS narrow-scan spectra of P 2s from CdSe nanocrystals thin films, in initial, PB and PD states.

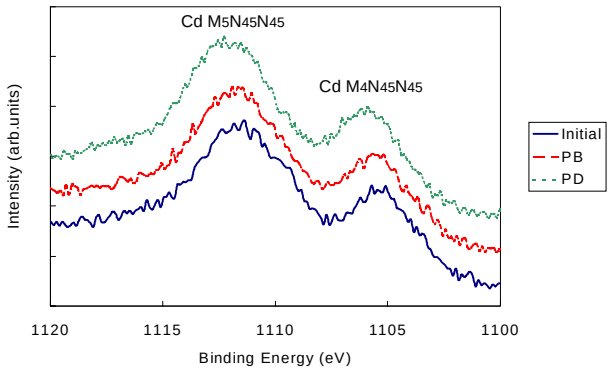

Fig. 6.3.5. XPS narrow-scan spectra of Cd MNN from CdSe nanocrystals thin films, in initial, PB and PD states.

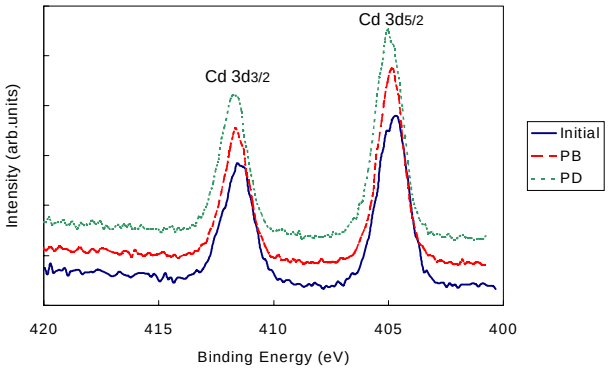

Fig. 6.3.4. XPS narrow-scan spectra of Cd 3d from CdSe nanocrystals thin films, in initial, PB and PD states.

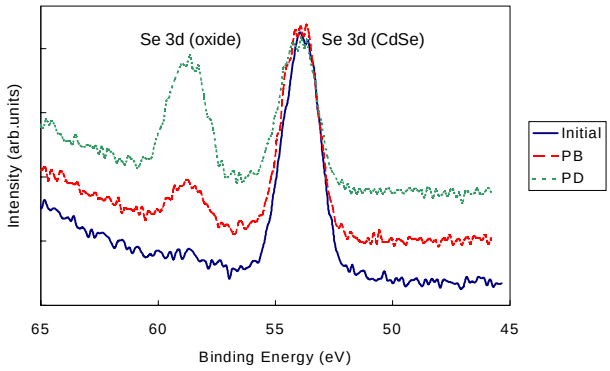

Fig. 6.3.6. XPS narrow-scan spectra of Se 3d from CdSe nanocrystals thin films, in initial, PB and PD states.

Based on the XPS results obtained, it can be concluded that decomposition of TOPO, desorption of TOP and oxidation of surface Se occurred after the laser irradiation. Here one may address the question: why PL intensity increased in PB state? In order to perform further investigation, the chemical structure of the CdSe nanocrystals surface is studied by ToF-SIMS.

6.3.3. Chemical structure analysis by ToF-SIMS

Positive ion mass spectra

Positive ion ToF-SIMS spectra are shown in Fig.6.4. Intensities of characteristic peaks in the spectra of initial, PB and PD states are summarized in Table 6.2. The intensities are normalized to those for the initial state. C_xH_y and Cd peaks were dominant peaks in low-mass region (Fig.6.4.1). Whereas the intensities of Cd peaks were decreased, those of CdO and CdOH were increasing with laser irradiation (Fig.6.4.2). These behaviors are believed to indicate the progress in surface oxidation of Cd, which is not clear in the XPS spectra (Fig.6.3.4). Comparative information on the oxidation index for Cd and Se will be discussed in the following section .

For organic ligand TOPO, its molecular ions (M-H and M+H) were observed at *m/z* 385 and 387, and the peaks were drastically increased in intensity in the PB state (Fig.6.4.3). Characteristic enhancement of the TOPO molecular ion peaks indicates that TOPO possesses slightly positive charge and the ionization probability of TOPO increases in the PB state. In addition, its dimer ion was observed only in the PB state (Fig.6.4.3). Appearance of the dimer ion can be explained to be due to the appearance of high TOPO coverage region on the CdSe nanocrystal surface.

Most interesting results are shown in Fig.6.4.4. Peaks arising from a TOPO-Cd

cluster are observed in Fig.6.4.4 irrespective of the laser irradiation time, while those from a TOPO-Se cluster are not found in the initial state. These results indicate that TOPO ligands are bound to the Cd sites in the initial state. This adsorption model is reasonable because TOPO is an electron-donating molecule and is thus expected to interact with Cd site. In the PB state, a cluster ion composed of TOPO and Se appeared. Appearance of the TOPO+Se ion indicates the formation of new chemical bonding between TOPO and Se. In summary, above results indicate that the laser irradiation induces migration of some TOPO molecules from Cd sites to Se sites.

Table 6.2. Characteristic peak intensities on positive ion ToF-SIMS spectra from CdSe nanocrystals thin films, normalized to the initial state.

Positive Ion	Mass	Initial	PB	PD
C_xH_y (x=1-5)		1.000	1.006	1.038
PO	46.97	1.000	0.996	1.077
$C_8H_{17}POH$	161.11	1.000	1.480	1.254
TBP+OH	219.19	1.000	1.251	1.100
$(C_8H_{17})_2PO$	273.24	1.000	1.172	1.099
TOPO-H	385.36	1.000	1.906	1.397
TOPO+H	387.38	1.000	**5.578**	2.193
$(TOPO)_2$+H	773.75	1.000	**64.750**	6.000
^{80}Se	79.92	1.000	1.218	1.288
^{114}Cd	113.90	1.000	0.901	0.768
$^{114}CdOH$	130.90	1.000	1.496	**2.357**
TBPO+^{114}Cd	332.08	1.000	1.304	0.854
TOPO+^{114}Cd	500.27	1.000	1.297	0.844
TOPO+^{80}Se+H	467.31	1.000	**23.778**	5.519

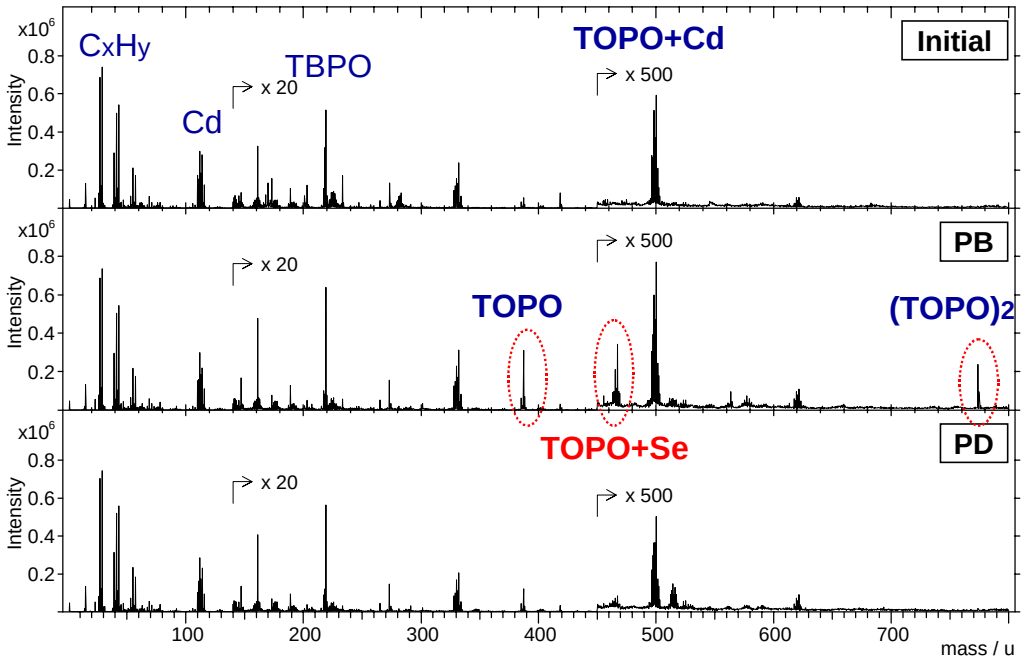

Fig. 6.4.1. Positive ion ToF-SIMS spectra from CdSe nanocrystals thin films, in initial, PB and PD states. Overview in the mass range of *m/z* 0-800.

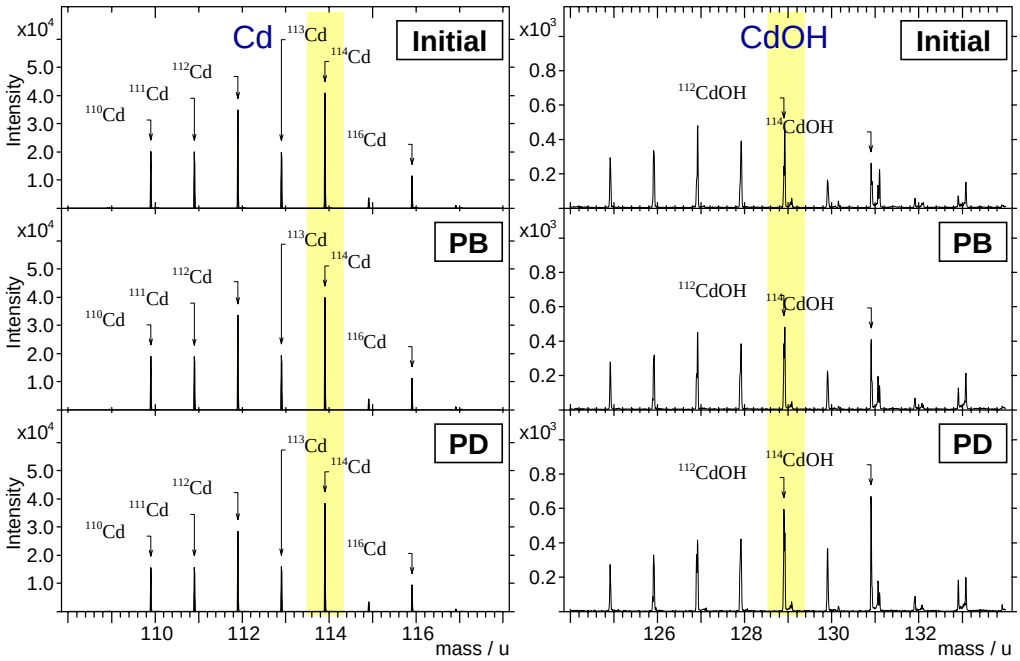

Fig. 6.4.2. Positive ion ToF-SIMS spectra from CdSe nanocrystals thin films, in initial, PB and PD states. Zoomed view of Cd^+ and $CdOH_x^+$ regions.

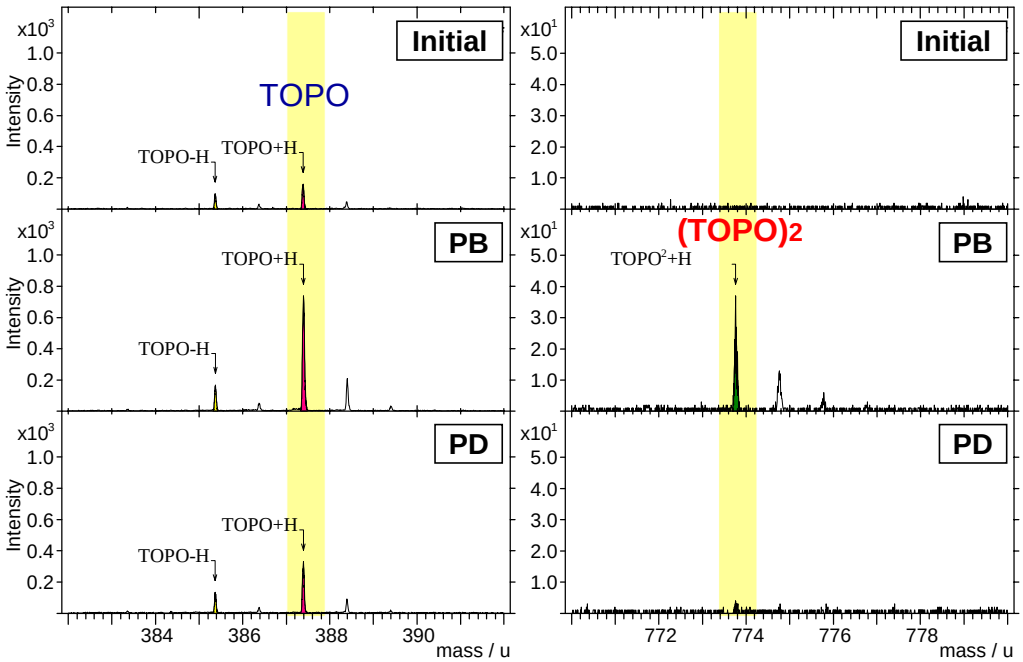

Fig. 6.4.3. Positive ion ToF-SIMS spectra from CdSe nanocrystals thin films, in initial, PB and PD states. Zoomed view of TOPO molecular and its dimer ion regions.

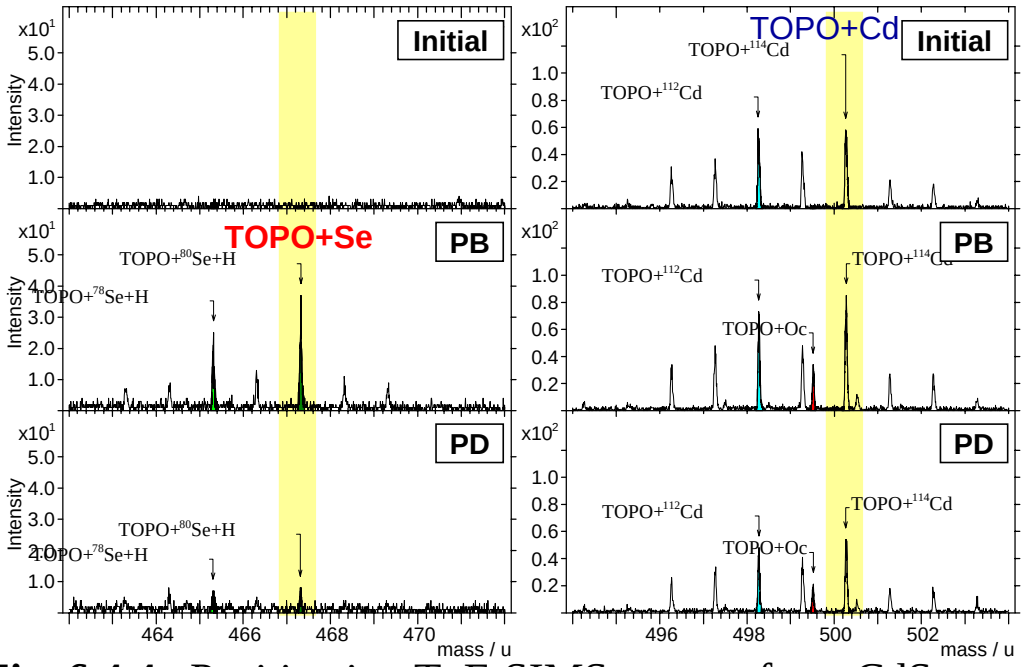

Fig. 6.4.4. Positive ion ToF-SIMS spectra from CdSe nanocrystals thin films, in initial, PB and PD states. Zoomed view of TOPO+Se and TOPO+Cd cluster ion regions.

Negative ion mass spectra

Negative ion ToF-SIMS spectra are shown in Fig.6.5. Intensities of characteristic peaks in the spectra are summarized in Table 6.3. The intensities are normalized to those for the initial state. OH_x and PO_x peaks were dominant peaks in low-mass region (Fig.6.5.1). Whereas the intensities of OH_x peaks were increasing, those of PO_x were decreasing with laser irradiation (Fig.6.5.2). Increase of oxygen and decrease of PO_x are also deduced from the XPS results.

Negative ion ToF-SIMS is useful especially for the analysis of the chemical state of Se, because Se, one of the electron-donating elements, tends to appear in the negative ion spectra. Negative ion spectra of Se and SeO_x are shown in Figs.6.5.3,4. With increasing irradiation time, Se peaks were decreasing and SeO_x peaks were increasing. These behaviors are believed to indicate the progress in oxidation of surface Se, which is consistent with the XPS results (Fig.6.3.6).

Table 6.3. Characteristic peak intensities on negative ion ToF-SIMS spectra from CdSe nanocrystals thin films, normalized to the initial state.

Negative Ion	Mass	Initial	PB	PD
OH_x(x=0-1)		1.000	1.128	1.285
PO_x (x=0-3)		1.000	0.939	0.795
$C_8H_{17}P_2O_5$	255.05	1.000	0.889	0.768
$(C_8H_{17})_2PO_2$	289.22	1.000	0.860	0.577
^{80}Se	79.91	1.000	0.619	0.417
^{80}SeO	95.91	1.000	1.486	1.445
$^{80}SeO_2$	111.90	1.000	**4.022**	**5.181**
$^{80}SePO$	126.88	1.000	0.777	0.635
$^{80}SePO_2$	142.88	1.000	0.779	0.538
^{114}CdO	129.90	1.000	1.231	1.043
$(C_8H_{17})_2P_2O_5$ $+^{114}Cd$	482.07	1.000	0.695	0.432

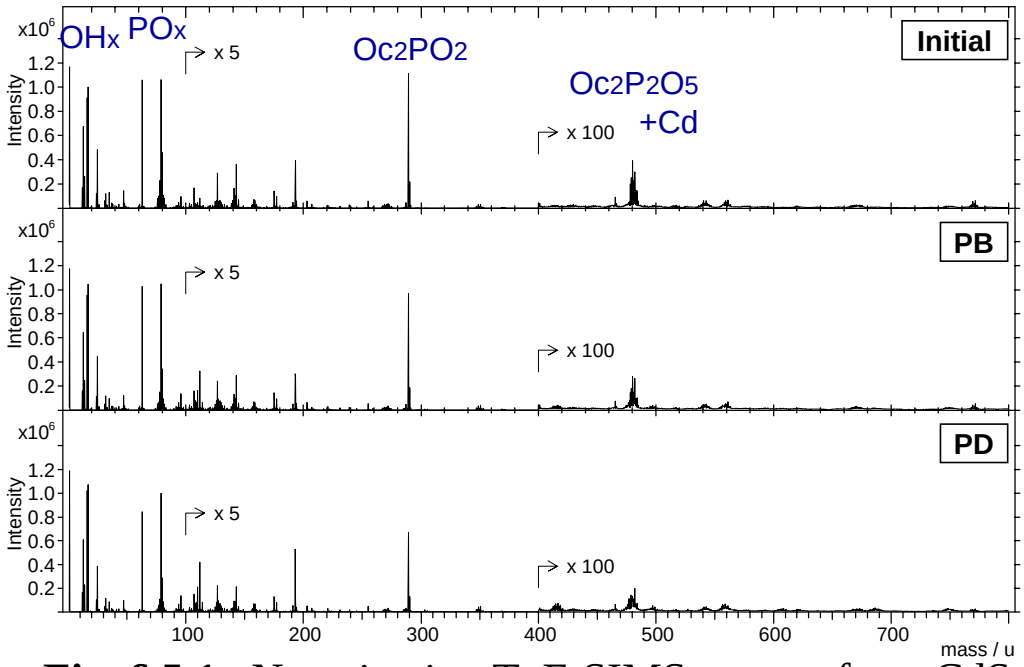

Fig. 6.5.1. Negative ion ToF-SIMS spectra from CdSe nanocrystals thin films, in initial, PB and PD states. Overview in the mass range of *m/z* 0-800.

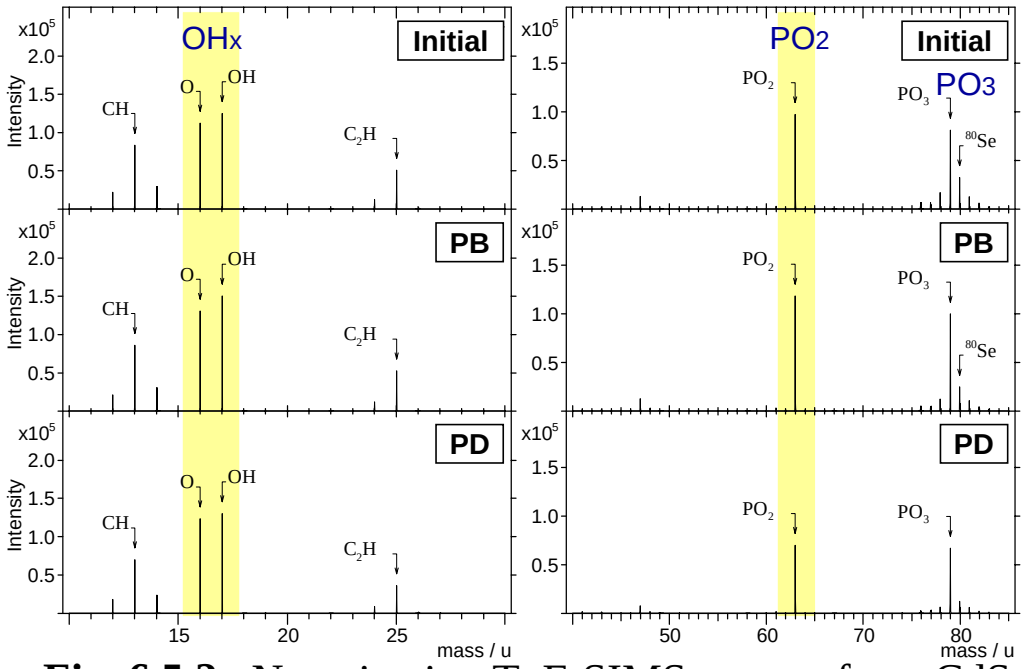

Fig. 6.5.2. Negative ion ToF-SIMS spectra from CdSe nanocrystals thin films, in initial, PB and PD states. Zoomed view of OH_x^- and PO_x^- regions.

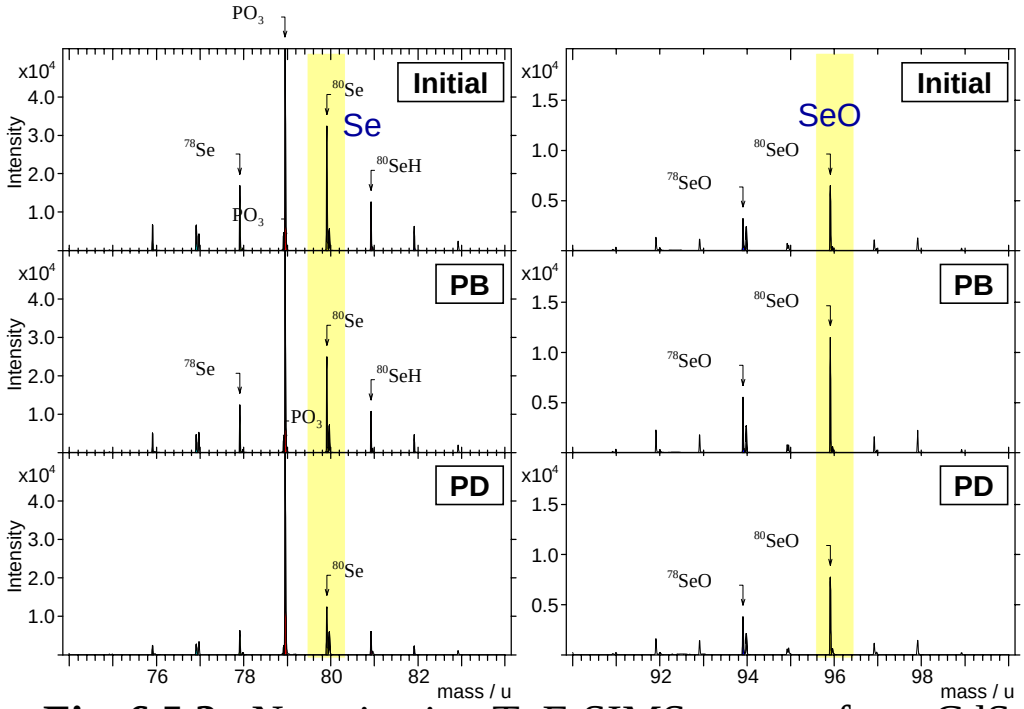

Fig. 6.5.3. Negative ion ToF-SIMS spectra from CdSe nanocrystals thin films, in initial, PB and PD states. Zoomed view of Se^- and SeO^- regions.

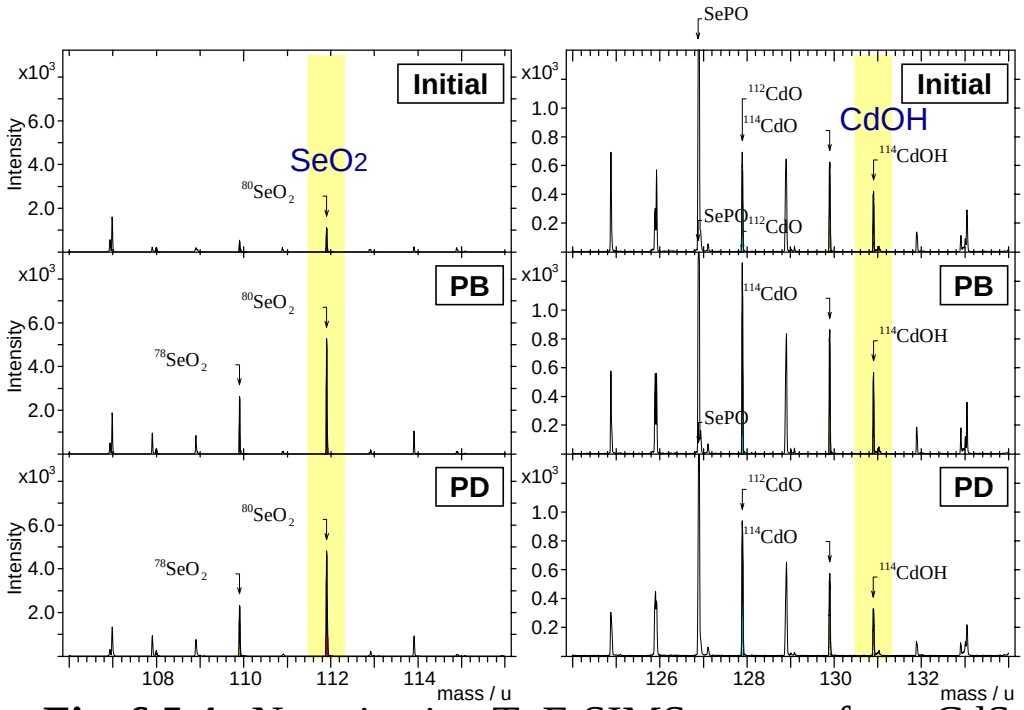

Fig. 6.5.4. Negative ion ToF-SIMS spectra from CdSe nanocrystals thin films, in initial, PB and PD states. Zoomed view of SeO_2^- and $CdOH_x^-$ regions.

6.4. Correlation between surface chemical structure changes and optical properties

6.4.1. Chemical structure changes

Based on XPS and ToF-SIMS results, the changes in the surface chemical structure of TOPO capped CdSe nanocrystals are proposed as follows: In the initial state, TOPO binds to Cd site, which is confirmed by the presence of TOPO+Cd cluster ions. After the short laser irradiation, a part of TOPO molecules are excited, described TOPO*, and slightly positive charged. Then TOPO* migrates on the surface from Cd site to Se site. This process is deduced from the observation of the characteristic enhancement of TOPO molecular ion peaks, and the appearance of the peaks of its dimer ions and TOPO+Se cluster ions in the PB state. The prolonged laser irradiation induces the further progress in the oxidation of surface Se and the decomposition of TOPO*, which is followed by TOP and SeO_2 desorption.

6.4.2. Optical properties

In the PB state, increase in PL intensity and blue shift of the peak position are observed. Enhanced PL intensity is explained to be due to the increase of the degree of surface nonradiative recombination site passivating by the rearrangement of the organic ligand TOPO*. Gradual blue shift of the peak position is attributed to the shrinkage of CdSe nanocrystals by desorption of SeO_2 as a result of the Se oxidation.

6.5. Comparison of oxidation index for Cd and Se extracted by XPS and ToF-SIMS

In order to prove the usefulness of ToF-SIMS as a tool for chemical state analysis of elements, oxidation index for Cd and Se extracted from XPS and the results of ToF-SIMS are comparatively discussed below.

6.5.1. Oxidation index for Cd

It is known that core-level spectra of Cd do not show detectable chemical shifts among the various chemical states. This is compatible with the present results; there was no significant change in Cd 3d and Cd MNN spectra, except for the slight energy shift toward the lower kinetic energy. Even when the chemical shifts in XPS spectra are small, further information on the chemical state may be obtained from Auger parameter (AP) [4], whose concept was introduced by Wagner. The AP for Cd is estimated from the Cd $3d_{5/2}$ and Cd $M_4N_{45}N_{45}$ peaks in XPS spectra, using the following equation.

$$AP = BE\ (Cd\ 3d_{5/2}) + KE\ (Cd\ M_4N_{45}N_{45})$$

The estimated AP values are shown in Table 6.4 and Fig.6.6(a). With increasing laser irradiation time, the AP slightly decreases, however, the observed change in AP is too small to identify the progress of oxidation. In short, the chemical state change of Cd cannot be detected in XPS even if the AP values are calculated.

As mentioned above, the organic ligand TOPO is likely to adsorb on the Cd sites with the O end, which leads to the chemical interaction between Cd and O. After laser irradiation, some TOPO migrate on the surface from Cd sites to Se sites in the PB and PD state, which may allow water to attack the bare Cd sites. However, it is difficult to prove the interaction between water and Cd from XPS as discussed above.

Table 6.4. Cd Auger parameter obtained from CdSe nanocrystals thin films, and reference values [5].

Sample	Cd $3d_{5/2}$ (BE, eV)	Cd $M_4N_{45}N_{45}$ (KE, eV)	AP (eV)	ΔAP (eV)
Initial	404.8	381.2	786.0	0.0
PB	405.0	381.0	785.9	-0.1
PD	404.9	380.7	785.6	-0.4
Cd	405.0	383.8	788.8	0.0
CdO	405.2	382.2	787.4	-1.4
CdSe	405.3	381.4	786.7	-2.1
CdS	405.3	381.1	786.4	-2.4
CdF_2	405.9	378.8	784.7	-4.1

In contrast with XPS, there is an unambiguous sign of Cd-water interaction in

positive ion ToF-SIMS spectra. With increasing laser irradiation time, the intensity ratio of CdOH / Cd clearly increases, as shown in Fig.6.6(a). This result indicates that the surface species covered on the Cd sites changed from TOPO to water after laser irradiation.

One possible reason for the difference between XPS and ToF-SIMS results about the sensitivity for changes in Cd chemical environment is the difference in the information depths. It should be taken into account that the information depth of ToF-SIMS is smaller than that of XPS [6]. It is considered that the chemical environment changes occur only at the outermost surface, and in this case ToF-SIMS should have the advantage of sensitivity.

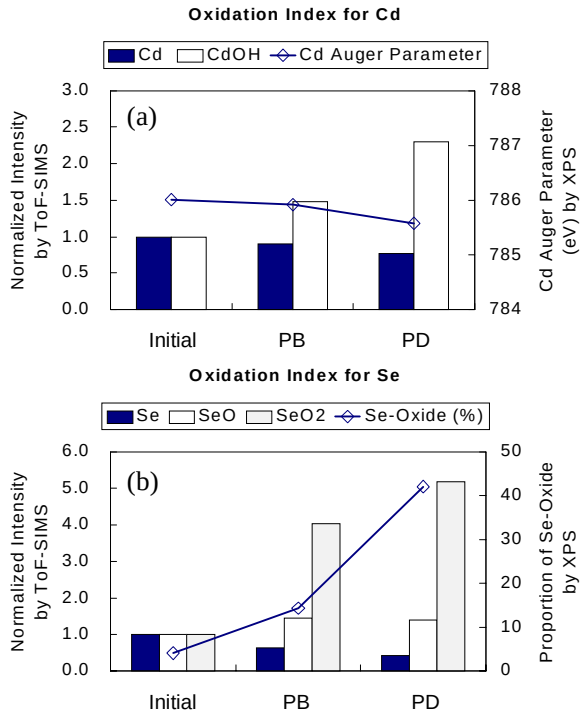

Fig. 6.6. Comparison of oxidation index for (a) Cd and (b) Se, obtained by XPS and ToF-SIMS.

6.5.2. Oxidation Index for Se

Compared with Cd, drastical change was induced by laser irradiation in the Se 3d XPS spectra, which gives much direct information on the chemical state change. With increasing laser irradiation time, a new peak arising from Se oxide appeared at 59 eV, which is well separated from the Cd-Se peak remaining at 54 eV. In this case, we can easily estimate the proportion of the number of Se atoms in each chemical state from XPS spectra. The variation in the proportion of Se oxide is shown in Fig.6.6(b), which gives quantitatively information on the proportion of each.

Unambiguous sign of Se oxidation is also obtained from negative ion ToF-SIMS spectra. With increasing laser irradiation time, the intensity ratio of SeO_2 / SeO and SeO / Se increases step by step, as shown in Fig.6.6(b). These changes clearly indicate the progress in surface oxidation of Se. Nevertheless, it is not easy to extract the quantitative information on the chemical state of elements from ToF-SIMS spectra.

6.6. Conclusions

It is demonstrated that the complementary information can be obtained on the changes in surface chemical structure of TOPO capped CdSe nanocrystals by comparative use of XPS and ToF-SIMS. Based on the results obtained, the changes in the surface chemical structure are proposed as follows:

1) In the initial state, TOPO molecules are likely to bind to the Cd sites, which is confirmed by the detection of TOPO+Cd cluster ions.

2) In the PB state, where PL intensity increases after the short laser irradiation, a part of TOPO molecules are excited, described TOPO*, and slightly positively charged. Then some TOPO* migrate on the surface from Cd sites to Se sites, forming TOPO*+Se complex.

3) In the PD state, where PL intensity gradually decreases after the long duration of laser irradiation, TOPO*-Se complexes are decomposed, which leads to the desorption of TOP and SeO_2.

XPS can provide the quantitative information on the elemental composition and

the chemical state of elements in the surface region. But there are some limitations to distinguish one chemical state from others or to characterize the chemical structure of organic molecules. ToF-SIMS can complete not only the qualitative information on the chemical state of elements but also the chemical structure of surface organic molecules. For example, ability for detection of the cluster ions between organic ligand and substrate element can provide the direct evidence of the chemical interaction. It can be concluded that the combination of XPS and ToF-SIMS is a very powerful method for microscopic chemical analysis for various surfaces.

References

[1] B. O. Dabbousi, J. Rodriguez-Viejo, F. V. Mikulec, J. R. Heine, H. Mattoussi, R. Ober, K.F. Jensen and M. G. Bawendi, *J. Phys. Chem. B*, **101**, 9463 (1997).

[2] S. Maenosono, E. Ozaki and Y. Yamaguchi, *Jpn. J. Appl. Phys.*, **40**, L638 (2001).

[3] H. Asami, Y. Abe, T. Ohtsu, I. Kamiya and M. Hara, *J. Phys. Chem. B*, **107**, 12566 (2003).

[4] C. D. Wagner, eds. by D. Briggs and M. P. Seah, Appendix 5, in Practical Surface Analysis, Vol.1: AES and XPS, 2nd ed., Wiley, Chichester, 1994.

[5] J. F. Moulder, W. F. Stickle, P. E. Sobol and K. D. Bomben, ed. by J. Chastain, p. 208, in Handbook of X-ray Photoelectron Spectroscopy, Perkin-Elmer, Minnesota, 1992.

[6] Y. Abe, M. Komatsu and H. Okuhira, *Appl. Surf. Sci.*, **203-204**, 859 (2003).

Chapter 7

Summary

Perspective on Practical Surface and Interface Analysis by advanced Use of HR-AES and ToF-SIMS

Auger electron spectroscopy has a great advantage in micro area analysis because the electron beam is adequate for reducing the probe size. Its usefulness will get more extensive if not only the elemental information but also the chemical information can be obtained. For this reason, the aim of studying the advanced use of AES is focused on how to extract the chemical information from the complicated Auger line shapes. I demonstrate two attempts in chapter 4 to understand the initial oxidation caused by the oxygen exposure. One is the simplest method, using Auger peak-to-peak height (APPH) obtained by the conventional AES. In the conventional AES system, AES spectra are measured in the derivative mode (differentiation with the lock-in amplifier). APPH's ratio between two peaks arising from the same Auger transition can be related with the degree of surface oxidation. Another is the more direct method analyzing the Auger line shapes without derivation. In the modern AES system, AES spectra can be directly measured with high-energy resolution. Along with the significant change in the line shapes, small energy shift of the peaks can be discussed as similarly as XPS.

But there are some disadvantages of AES. Firstly, an electron excitation of the small area on the surface will cause severe charging effects and damages to the sample. It is quite difficult to apply AES to organic materials. Secondly, hydrogen is not detectable in principle. Hydrogen and its compounds are the key species in order to characterize the initial oxidation on the metal surfaces.

In early 1990's time-of-flight secondary ion mass spectrometry has widely come into use and been getting more and more extensive. ToF-SIMS has many advantages that complement the disadvantages of the conventional techniques. Thus, the aim of studying the advanced use of ToF-SIMS is devoted to obtaining complementary information on the hydrogen-including species and organic molecules on the surface. Quick data collection and ability for hydrogen detection enable us to monitor the surface reaction. I demonstrate the in-situ monitoring of the initial oxidation on the Gd surface in chapter 4. Combined with AES results, the whole process progressing on the oxygen-exposed Gd surface is clearly drawn. High-mass resolution and high-mass accuracy enable us to characterize organic thin films. High sensitivity for trace elements on the surface and high-spatial resolution enable us to analyze the trace elements on the surface. I demonstrate the typical use in industry applying to the magnetic recording media in chapter 5. In particular, I found that the ionization probability from the functional end groups concerned with the chemical bonding strongly depends on the chemical interaction between the organic molecules and substrate atoms.

However, even ToF-SIMS has some limitations that should be overcome in the near future. First of all it is difficult to obtain the quantitative information because the intensities of secondary ions are quite affected by many factors of the chemical environment. This major disadvantage can be overcome by the combined use with the conventional techniques such as AES and XPS, which provide the quantitative information on both elemental and

chemical state. I demonstrate the comparable study of CdSe nanocrystals thin films by ToF-SIMS and XPS in chapter 6. The photon-induced changes in surface chemical structure are thoroughly discussed from the various aspects of atomic composition, chemical bonding state and adsorption site of organic ligand. In particular, I found that the cluster ions between organic ligand and substrate element can provide the direct evidence of the chemical interaction.

In general each technique has advantages and disadvantages. It should be noticed that the combination of several techniques, which are adequate and complementary for the present objective, is getting more and more necessary to characterize the practical surfaces in the real world.

It is believed that the applications described here can provide the appropriate perspective on the practical surface and interface analysis.

Acknowledgements

Many people contributed to this work.

I wish to express my deep appreciation to Prof. K. Edamoto, who provided valuable suggestions and fruitful discussions to complete this work.

I am also grateful to Prof. E. Miyazaki, who instructed me in surface science with profound knowledge.

I would like to thank T. Koyama, Dr. T. Nakamura, Dr. T. Akai, T. Kawano, K. Uchino, J. Kozu, K. Seki, K. Sawada, Y. Sasaoka, T. Matsuo, Dr. H. Asami, J. Sasahara, M. Shibayama, H. Yamauchi, A. Kawai and coworkers in Yokohama Research Center (YRC) of Mitsubishi Chemical Corporation (MCC). Most of all experiments in this work were performed in YRC of MCC.

Especial thanks are devoted to Yuki Abe of my wife, who encouraged me to finish my work in both my laboratory and home.

In addition, I am grateful to Dr. S. Tanuma and Dr. S. Hashimoto of Surface Analysis Society of Japan for stimulating my work to apply to the field of practical surface analysis.

Finally, I want to express gratitude to H. Okuhira, Dr. M. Komatsu of Hitachi Science Systems, Ltd. and M. Tozu of ULVAC-PHI, Inc. for expertly operating ToF-SIMS systems. In particular, H. Okuhira kindly instructed me in the ToF-SIMS field and collaborated on many experiments in this work with me.

M. Takagi of Nissei Electronics, Ltd. kindly organized this collaboration.

Dedicated to my mother Toshiko and my departed father Seiichiro.

List of Publications

Original Papers

(1) “Angle-resolved Photoemission Study of the Surface State on NbC(111)”,
K. Edamoto, Y. Abe, T. Ikeda, N. Ito, E. Miyazaki, H. Kato and S. Otani,
Surface Science, Vol.237, 241-247 (1990).

(2) “Oxidation Study of 3d Transition Metals (Cr, Fe, Co and Ni) and Rare Earth (Tb): AES Application to Auger Depth Profiling of Magneto-optical Disk”,
Y. Abe, A. Kato and T. Nakamura,
Surface and Interface Analysis, Vol.22, 14-17 (1994).

(3) “AES and REELS Study of Fe/Ni Alloys”,
Y. Abe and Metal Materials Group of SASJ,
Journal of Surface Analysis, Vol.5, No.2, 266-269 (1999).

(4) “Characterization of Micro-Corrosion on Magnetic Recording Disks by ToF-SIMS and AAS”,
Y. Abe, M. Shibayama, J. Sasahara and J. Kozu,
Journal of Surface Analysis, Vol.6, No.2, 148-154 (1999).

(5) “Characterization of Lubricant Films on Magnetic Recording Disks by ToF-SIMS”,
Y. Abe, M. Shibayama and T. Matsuo,
Surface and Interface Analysis, Vol.30, 632-634 (2000).

(6) “Gd 表面での初期酸化状態の研究を基にした UHV 装置内の残留ガスの評価”,
Y. Abe,
Journal of Surface Analysis, Vol.7, No.2, 203-210 (2000).

(7) “ToF-SIMS による Gd 表面の初期酸化過程の研究”,
Y. Abe and H. Okuhira,
表面科学, Vol.22, No.9, 579-585 (2001).

(8) “ToF-SIMS Characterization of Molecular Ions from Fomblin Z-DOL on Ag Substrate”,
Y. Abe and H. Okuhira,
Applied Surface Science, Vol.203-204, 175-179 (2003).

(9) “Estimation of ToF-SIMS Information Depth in Micro-corrosion Analysis”,
Y. Abe, M. Komatsu and H. Okuhira,
Applied Surface Science, Vol.203-204, 859-862 (2003).

(10) “Surface State Analysis of Photobrightening in CdSe Nanocrystal Thin Films”,
H. Asami, Y. Abe, T. Ohtsu, I. Kamiya and M. Hara,
Journal of Physical Chemistry B, Vol.107, No.46, 12566-12568 (2003).

(11) “Chemical Structure Changes in TOPO Capped CdSe Nanocrystals Thin Films by Comparable ToF-SIMS and XPS Study”,
Y. Abe, H. Asami, H. Yamauchi, T. Ohtsu, I. Kamiya, H. Okuhira and K. Edamoto,
Journal of Surface Analysis, Vol.11, No.2, to be published (2004).

Other Articles

(1) “AlGaAs/GaAs 多層膜断面での ToF-SIMS イメージング”,
Y. Abe and H. Okuhira,
Journal of Surface Analysis, Vol.7, No.2, 262 (2000).

(2) “AES による化学状態分析の一例”,
Y. Abe,
Journal of Surface Analysis, Vol.8, No.2, 139-146 (2001).

(3) “EPMA 波形変化の一例”,
Y. Abe, Yuki Abe and T. Nakamura,
Journal of Surface Analysis, Vol.8, No.2, 160-163 (2001).

(4) “AES における高エネルギー分解能測定時のエネルギー軸較正”,
Y. Abe,
Journal of Surface Analysis, Vol.9, No.2, 185-191 (2002).